SENSING AND DYNAMICS OF LEAN BLOWOUT IN A SWIRL DUMP COMBUSTOR

A dissertation
presented to
the academic faculty

by

Muruganandam Thiruchengode

In partial fulfillment
of the requirements for the degree
Doctor of Philosophy

School of Aerospace Engineering
Georgia Institute of Technology
May 2006

SENSING AND DYNAMICS OF LEAN BLOWOUT IN A SWIRL DUMP COMBUSTOR

Approved by:

Dr. Jerry Seitzman, Advisor
School of Aerospace Engineering
Georgia Institute of Technology.

Prof. Ben T. Zinn
School of Aerospace Engineering
Georgia Institute of Technology.

Prof. Jeff Jagoda
School of Aerospace Engineering
Georgia Institute of Technology.

Dr. Tim Lieuwen
School of Aerospace Engineering
Georgia Institute of Technology.

Dr. Richard Gaeta
Advanced Transportation and Advanced
Systems (ATAS) Laboratory
Georgia Institute of Technology.

Date Approved: 13 March 2006

To my parents

For their love, understanding and support

ACKNOWLEDGEMENTS

First of all I would like to thank my advisor, Jerry Seitzman for his guidance and mentoring throughout my stay at Georgia tech. I had a wonderful time during all the discussions from the very first meeting onwards. I would like to thank him for providing a great learning, research and teaching opportunity. I appreciate his patience and cheerful attitude towards my exaggerated claims and generalizations during discussions.

I also would like to acknowledge the helpful comments and guidance from Dr. Tim Lieuwen, Dr. Jagoda, Dr. Zinn throughout the research period of this research. I would like to thank the thesis reading committee for their helpful comments and for taking an active part in the committee.

I would like to thank Suraj, Rajesh, Ben, David, Yedidia, Bobba, Randy, Rob, Shashvat, JP, Thao, Santosh Sr. and Santosh Jr. for the valuable discussions during the course of this research work. Without their critical comments about my theories, this theory of blowout would be having several shortcomings.

I would like to thank Randy Olsen for the discussions and his non-stoppable urge to learn, which made me understand my research problem better. I would like to thank Matt, Joshua, Ryan, Mayank, Jessica, Bryan, Byoung-Hui, Charles, Logan, David Butts, Colby and Sasha for helping me with parts of my work at several instances in this work. I would like to thank Harry Rudd, Wayne Springfield, Scott Mosley and Chuck Albert for their help in building the components of the experiments.

I thank all the lab people for the great research environment. I thank all the combustion lab research engineers and John Holthaus for ensuring safety and smooth

running of research work. I would like to thank all the graduate students in the lab that helped me expand my knowledge through a variety of questions about anything in life. I would like to thank the lab gang and the indian gang who made my life at GT a lot of fun even with all my injuries. Special thanks to my room mates for making sure that food and other utilities existed whenever I went home.

I would like to thank the GThapkido club and black knight martial arts team, who made me unwind from research oriented thinking and removed the frustrations of work. In particular, I thank Master Nils Onsager and Mr. Brian Ritchie for bringing my morale up during tough times.

Finally, I would like to thank my family for their love and support which encouraged me in every step of my life.

Table of contents

List of Tables

List of Figures

Summary

This thesis describes an investigation on the blowout phenomenon in gas turbine combustors. The combustor primarily used for this study was a swirl- and dump-stabilized, atmospheric pressure device, which did not exhibit dynamic combustion instabilities. The first part of the thesis work concentrated on finding a sensing methodology to be able to predict the onset of approach of blowout of the combustor using optical methods. Temporary extinction-reignition events that occurred prior to blowout were found to be precursor events to blowout. A threshold based method was developed to identify these events in the time-resolved sensor output. The number and the average length of each event were found to increase as the LBO (fuel-air ratio) limit is approached. This behavior is used to predict the proximity to lean blowout.

In the second part of this study, the blowout sensor was incorporated into a control system that monitored the approach of blowout and then actuated an alternate mechanism to stabilize the combustor near blowout. Enhanced stabilization was achieved by redirecting a part of the main fuel to a central preinjection pilot injection. The sensing methodology, without modification, was effective for the combustor with pilot stabilization. An event based control algorithm for controlling the combustor from blowing out was also developed in this study. The control system was proven to stabilize the combustor even when the combustor loading was rapidly changed.

The final part of this study focused on understanding the physical mechanisms behind the precursor events. High speed movies of flame chemiluminescence and laser sheet scattering from oil droplets seeded into the reactants were analyzed to explain the

physical processes that cause the extinction and the reignition of the combustor during a precursor event. A mechanism for coupling of the fluid dynamics of vortex breakdown and combustion during precursor and blowout events is proposed. This mechanism is consistent with the behavior of the combustor near blowout as observed in sensing and control experiments.

This understanding of blowout phenomenon, along with the sensing and control strategies developed in this study could enable the gas turbine combustor designers to design combustors with wider operability regimes. This could have significant payoffs in terms of reduction in NOx emissions from the combustor.

Chapter 1

Introduction

1.1 Lean blowout problem

Emission of pollutants is a major concern in the design of modern combustion systems. Diffusion flames have been used traditionally in gas-turbine engines because of their reliable performance and reasonable flame holding characteristics, but they tend to produce high NOx emissions. The increasingly strict regulation on pollutant emissions has recently led engine manufacturers to develop low-emissions gas turbine engines.[2] For gas turbine engines, the predominant options for ultra low NOx emissions include Lean Premixed (LP) combustion and Rich-Quench-Lean (RQL) combustion.[2-5] Of these methods, RQL techniques are hampered by soot formation and incomplete mixing between fuel-rich combustion products and air.

Gas turbines with LP combustion have demonstrated the ability to greatly reduce NOx emissions in ground power generation, and similar improvements are available for premixed, prevaporized liquid-fueled combustors.[6] Even for current aeroengine combustors, which operate in a partially premixed mode with rapid mixing after fuel injection, increased fuel-lean operation may reduce NOx emissions.[7] The lower temperatures in the combustion zone for leaner mixtures, decreases the thermal NOx formation,[3] a predominant mechanism for NOx production in hydrocarbon/air flames. The current engineering challenge is to reduce pollutant emissions while simultaneously improving (or at least maintaining) power output and reliability of the engines.

Stabilization of slowly propagating flames against the high speed flow in a gas turbine combustor is a challenge by itself. Common flame holding methods in gas turbine combustors are: 1) bluff body flame holders, 2) swirl or sudden area expansions and 3) secondary flames (pilots). The underlying strategy is that 1) the lower velocity regions, 2) the heat and radical feed back created in the recirculation zones or 3) the pilot flame can help increase the reaction rates and stabilize the flame. When the mixture is made leaner, the reaction rates and the flame speed decrease. If the stabilization method used is not sufficient to sustain the flame inside the combustor, the flame is convected out of the combustor, and this is called blow out of the flame or combustor. The equivalence ratio at which blowout occurs is referred to as the lean blowout (LBO) limit.

In land based engines used for power generation, a blowout necessitates an expensive shut down and relight procedure, in addition to the loss of power during this period. Similarly, lean blowout in an aircraft engine causes loss of thrust and thus poses a significant safety hazard. This is especially important when power (and fuel flow) is reduced during approach and landing. Although analysis of the combustor flow field can give a crude estimate of the LBO limit for some well-specified operating condition, the stochastic nature of turbulent flows and perturbations of the operating environment can move the system beyond the stability of the given combustor.[5,8] Since most practical combustion systems have inherent disturbances that can trigger blowout, blowout limit is not a well defined curve on an operating map of the combustor (Figure 1). Currently, stable performance is ensured by operating the combustor with a wide margin above the uncertain LBO limit, as there is no technology to estimate the proximity to LBO.

Typically, an engine operating line will not be along the edge of its combustor's operating regime. Thus designers have to design to ensure operability during the worst possible conditions. This requirement puts a constraint on the best operating point during normal operating conditions. As shown in Figure 1, during the normal operating conditions, the best operating point in terms of NOx will be the leanest condition for that velocity in the combustor. But due to the design constraints, the combustor is forced to operate at a relatively higher fuel-to-air ratio, which produces higher NOx emission.

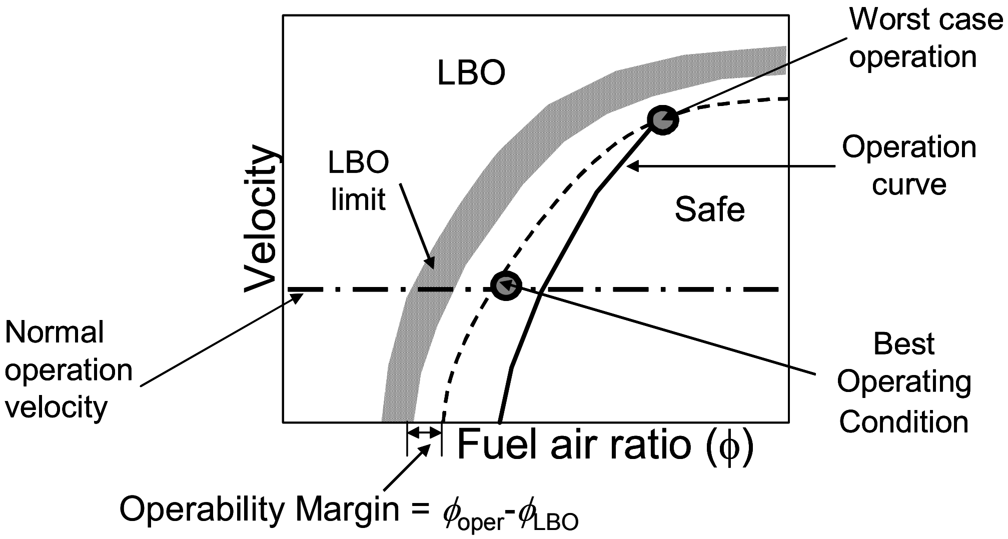

Figure 1. Operating map of a combustor showing blowout limit, operability margin (dotted curve) and operating line. Also shown is the best operating condition for a given velocity.

Furthermore, there is a new constraint due to the possibility of dynamic change in the operating conditions. A rough sketch of a basic gas turbine is given in Figure 2(a). The compressor compresses air from the atmosphere; fuel is mixed with the air and burnt in the combustor; and the hot products expand through a turbine, which powers the compressor through shaft work. The hot gases exiting the turbine have high thermal and kinetic energy. For thrust producing engines, this energy can be converted to useful energy by another turbine stage (turboshafts, turbofans, turboprops) or a nozzle (turbojet).

For electricity or other power generating systems, the additional energy can be extracted in a power turbine.

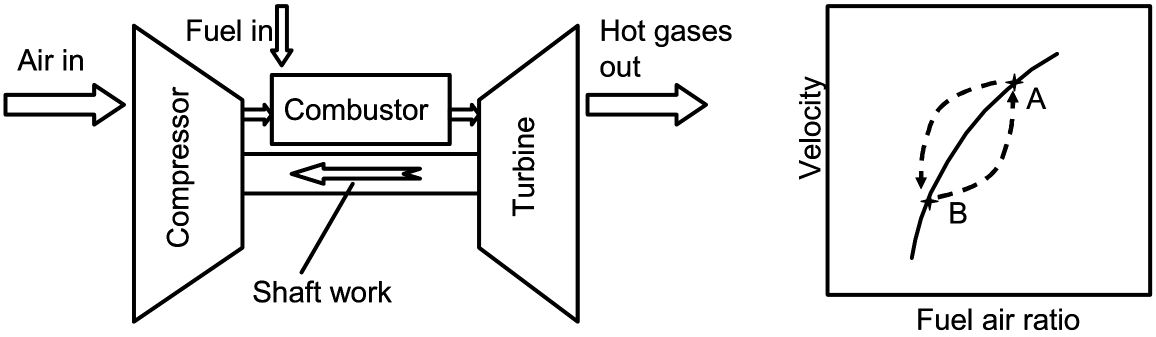

(a) (b)

Figure 2. (a)Schematic of a basic gas turbine engine. (b)Transient processes between two points on the operating regime plot in a gas turbine. The solid line represents the design operating line while the broken line arrows represent the transients.

This basic structure of the gas turbine engine has drawbacks when there is a need for rapid changes in operating conditions. When the power required is decreased, the primary way to decrease the output of the gas turbine is by decreasing the fuel flow rate. This decreases the thermal energy in the hot gases and thus the turbine derives lesser power, which in turn decreases the air flow rate through the compressor. Due to inertia of these rotational devices, during a transient the combustor experiences a condition where the fuel-to-air ratio decreases first, followed by decrease in the mass flow rate (see Figure 2(b)) and thus a decrease in power output.

The constraint of avoiding blowout even during these transient conditions forces combustor/engine designers to operate in further non-optimal conditions. The operating curve has to be such that even transient processes do not cross the operability (safety) line (see Figure 3). This forces the normal operating point further away from the best (lowest NOx emission) operating condition. The other solution is to limit the variability of the power output, to decrease the excursions from the operating curve, and so allow a slightly leaner operation. But this decreases the flexibility of the engine's operation.

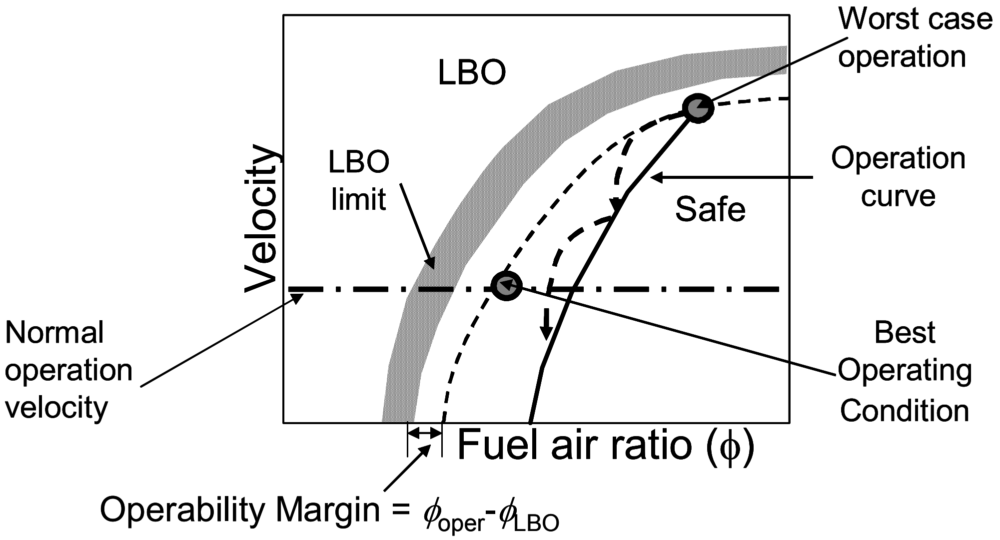

Figure 3. Operation regime plot showing modified operation curve for accommodating transient processes.

Thus, the issue of avoiding blowout of the combustor tends to increases the NOx production from gas turbine engines. One of the primary reasons for this situation is the standard approach to avoiding the uncertain combustor blowout is to operate with a considerable blowout margin. Enhanced performance can therefore be obtained with a reduction of this margin. Therefore, the ability to sense approach of LBO limit can provide significant payoffs. For instance, a sensing methodology with appropriate sensitivity, reliability and time response could be used to detect the onset of LBO. This would decrease the blowout margin required (since it decreases the uncertainty on the proximity to blowout) and allow for leaner operation, which in turn will reduce NOx emissions.

The overall objective of this work is to develop a sensing methodology that can detect and assess the proximity to LBO limit and thus provide early warning before the actual blowout of the combustor. The sensing methodology, when used in conjunction with an active control system that would allow combustors to run at leaner equivalence ratios compared to the present combustors, would reduce NOx emissions without loss of flame. The presence of such a control system would also allow design of combustors based on nominal operation instead of the worst case, as the rare occurrence of the worst case can be handled by the control system. This will result in better pay offs in terms of NOx reduction as the engine will be operating near the optimum for longer duration.

1.2 Current understanding of blowout phenomenon

There is a large body of extensive studies on stability of combustors. Stability of a combustor can be broadly classified into static and dynamic stabilities. Self-excited oscillations due to coupling of chemical reaction rates with the pressure and flow oscillations in the combustor is termed dynamic instability.[9] A combustor is considered to be statically unstable when the flame cannot be held inside the combustor. Therefore at flashback or blowoff, the flame becomes statically unstable. Static stability boundaries are usually dependent on operating parameters like flow rate, temperature and equivalence ratio. Dynamic instability can cause fluctuations in some of these parameters and can thus drive the combustor operating conditions towards its static stability limits. Likewise, static instability can cause changes in flame shape and thus affect the heat release distribution inside the combustor and thus drive dynamic instabilities.

Although there is much research in the field of controlling dynamic instability, there is less work in understanding complex combustors near their static stability limits (flashback or blowout limits). This work focuses only on static stability of the combustor and does not consider cases with dynamic instability. The terminology "static" is misleading since in reality the static instability is a time varying process; for example, flame shape and flame location can change in the combustor. Therefore, this work also emphasizes the temporal behavior of the combustor near its static stability limits; in particular, the lean blowout limit.

Stabilization of the flame (holding the flame stable in a desired volume) in high speed flows such as in gas turbine combustors has been dealt with for several decades. The main research focus was to improve flame stabilization in high speed streams. Others focused on predicting the blowout limit for the given configuration of the burner. The several types of stabilization methods developed thus far will be briefly described in the following chapter. But these studies did not focus on understanding the behavior of the flame near the blowout limit for a particular stabilization mechanism or the specific process by which stabilization is lost.

Wohl *et al*. observed that a jet flame's lift off was not a symmetric process, and the flame did not lift off always from a fixed point on the jet exit. Additionally, there was a range of velocities where the flame could lift off or "drop back" (reattach) to the lip of the jet. They reported an approximate regime where the flow was unpredictable. They reported that small disturbances could push the flame to either lift off or reattach when in this regime. Nicholson and Field[11] observed large scale pulsations in the flame as it was blowing off. They also reported that the main flame detached and reattached to the flame holder before extinguishing completely. Chen and Goss[12] attempted to characterize the intermittent behavior near liftoff for various flames studied, in terms of a crossing frequency. They reported that the frequency appeared to be irregular but remained in the range of 100-150 Hz.

There have been several studies in simple flames that indicate there is local loss of flame that grows to complete loss of flame.[13-16] Kurosoy and Whitelaw[17] studied opposed flames, with and without acoustic forcing, by means of laser Doppler velocimetry. They related the local extinctions to high strain rates. They reported temporary extinction and reignition when the equivalence ratio was very close to extinction limit. Sardi *et al.*[18] studied extinction of forced turbulent counterflow flames. They reported that when the strain rate was quickly cycled beyond the critical strain rate, the flame did not extinguish. However, when the cycling period exceeded a critical time scale, the flame was weakened over several cycles, which suggested that temperature played a role in extinction.

One of the first studies of flame structure within a combustor with geometry close to gas turbine combustors was by Roquemore *et al.*[19] The combustor used in this study was a non-premixed combustor stabilized by a sudden expansion. They reported longitudinal oscillation of the flame just prior to blowout. They hypothesized that the flame must liftoff prior to blowout, and they tried to find the conditions for the liftoff of the flame in this complex flow field. They reported that the stochastic nature of the flame made it difficult to quantify the precise equivalence ratio of the transition. They used laser-induced fluorescence of OH and showed that the instantaneous reaction zones had holes in them. They therefore concluded new combustor modeling approaches were needed that included the interaction between vortex structures and reaction zones.

Chao *et al.*[20] used acoustic excitation to stabilize a jet flame beyond its stability limit and then suddenly turned off the excitation to understand the blowout process. They found the flame went through a pulsating phase before the onset of liftoff and eventually blowout. They also found that the process depended on the rate at which the conditions are changed towards blowout. They suggested that the high strain rates, much higher than the extinction strain rate, encountered by the flame base should be a prominent factor in the blowout process.

De Zilwa *et al.*[21] investigated flame dynamics close to blowout in dump stabilized combustors with and without low swirl. They noticed very low frequency oscillations as the rich and lean extinction limits were approached. They monitored the CH emission intensity to identify the combustion zone. They report that one of the two branches of their dump-plane stabilized flame extinguished after oscillating for around 5-10 sec. The oscillatory behavior was found to be around 3-12 Hz and was independent of the combustor configurations studied.

A handful of numerical studies simulate the nonlinear dynamics before the extinction limit in simple flames.[15,16] They show that apparently chaotic combustion can occur near extinction limit if full interaction of the fluid dynamics and the transport process are taken into account. However, due to higher complexity of the problems, little work is done in modeling practical combustor configuration. Black and Smith[22] assessed the LES modeling of blowout of a low emission gas turbine fuel injector. They concluded that the models used for spray and chemistry require improvements to predict near blowout behavior correctly.

There is very little literature on preventing blowout of a combustor by use of a control system. There are two U.S. patents[23,24] on avoiding LBO of the combustor in which they just detect the approach of LBO from pressure signal disturbances. A select band of frequencies were known to give disturbances near blowout and were monitored.

When the amplitude in this band increased, the controller was given an alarm signal. The controller then increased fuel to avoid blowout, which increases the NOx penalty. The control researchers are not yet able to model the combustor blowout and thus are unable to come up with an effective blowout control system. The common approach is to map out the combustor's operability and monitor the conditions to ensure operation of the combustor.

1.3 Overview of present work

Thus the main understanding of blowout dynamics is that there is some unsteady behavior as the blowout limit is approached, and the dynamics depend on the actual rate at which blowout is approached. It is evident that this understanding is in its primitive stages and is mostly from simple combustors and not from studies of practical engine combustors. Thus the need to develop a sensing and control system for blowout of a combustor needs systematic analysis of the unsteady phenomenon observed near blowout. This understanding can then be used to develop sensing methodologies to assess the proximity to blowout limit.

This dissertation therefore also includes an investigation of the dynamics of blowout in a simplified model of a gas turbine engine combustor, with the objective of improving an advance warning system for sensing blowout of the combustor. The first part of this work is towards developing a sensing strategy to estimate the proximity to blowout limit. The sensing approach in this work is based on optical detection, as opposed to the parallel effort by Nair,[25] which describes acoustic detection of lean blowout. The second part of this work is an implementation of the sensing method into an active control system that can avoid blowout of the combustor. The final phase of this work is research intended to improve the understanding of the physical mechanisms behind the unsteady behavior of swirl-stabilized flames near blowout.

Chapter 2 of this dissertation gives the background and previous studies related to the current work. Chapter 3 describes the experimental setup and procedures used in this study. Chapter 4 describes the blowout sensing methodology developed in this work. Chapter 5 gives an example application of this sensing method in an active control system that avoid blowout in a swirl-stabilized combustor. Chapter 6 discusses the physical mechanisms behind the observations and results described in Chapters 4 and 5. Chapter 7 concludes the thesis with a summary of the findings and suggestions for future work in this area.

Chapter 2

Background

This chapter provides a foundational background for understanding the work presented in the following chapters. The first two sections of this chapter discuss stabilization of flames in high velocity flow streams. The following section introduces flow dynamics in swirling flows without combustion. The next section presents modifications to the swirl flow brought about by combustion. The last section briefly presents the near blowout behavior of flames

2.1 Stabilization

Premixed laminar flames propagate normal to themselves at a fixed speed known as the laminar flame speed. This speed depends on the net heat release, the thermal and species diffusivities, and the relevant chemical reaction rates, which are functions of local temperature, pressure and fuel/oxidizer mixture.[3] Flame speeds can also be affected by flow related heat and species transfers away from the reaction zone in a non-normal direction. Thus the flow field can either enhance or inhibit flame speed; this is often called the stretch/curvature effect.[26,27] While premixed flames have a propagation speed, nonpremixed, diffusion flames do not. For reasonably fast chemistry, they burn in regions of near stoichiometric mixture fraction.[3,28] It has been shown that jet diffusion flames are stabilized by a small premixed flame near the lip of the jet burner.[29,30] Thus the diffusion flame can also propagate due to propagation of the anchoring premixed flame.

When the propagation speed matches the flow speed, the flame can be easily contained in a desired volume in the combustor. However the case of flow speed of the order of flame speed does not fit the requirements of current high heat release rate combustors. This is due to the high flow speeds (~50 m/s) needed for the power requirement while the flame speeds are orders of magnitude lower (~30-100 cm/s). When flow speeds are much larger than the flame speed, the flame will be blown out of the combustor and when the flame speed is higher, the flame flashes back, trying to move upstream of the combustor. In both cases, the flame does not remain in the desired region of the combustor, and is said to have lost its stabilization.

The combustion research community has been facing the challenge of understanding stabilization mechanisms of flames for over sixty years. Specifically flame holding in high velocity flows is a complex problem with close coupling between chemical reactions, heat transfer and turbulent fluid dynamics. There is a large body of work focused on understanding the mechanisms of flame stabilizations in high velocity streams. The stabilization mechanisms used to hold the flame in high velocity flows depend upon several parameters such as flow rate, flow geometries, swirl, heat release rates, fuel/air composition, temperature, and the presence of ionized species.[11,31-38]

2.2 Stabilization mechanisms

Perhaps the simplest method for extending the combustor operating range to higher flow speeds is preheating the air before it enters the combustor. Changing the fuel composition, for example to produce a higher heating value, can also extend a combustor's operability. For instance, adding acetylene or hydrogen to most hydrocarbon fuels can increase flame speed and thus help stabilize the flame in higher velocity streams. Similarly, near stoichiometric fuel-oxidizer mixtures often have the highest flame speeds for a given fuel-oxidizer combination. Although operating at close to stoichiometric conditions and preheating help increase flame speeds, they also entail severe penalties in NOx emissions due to the higher product gas temperatures.

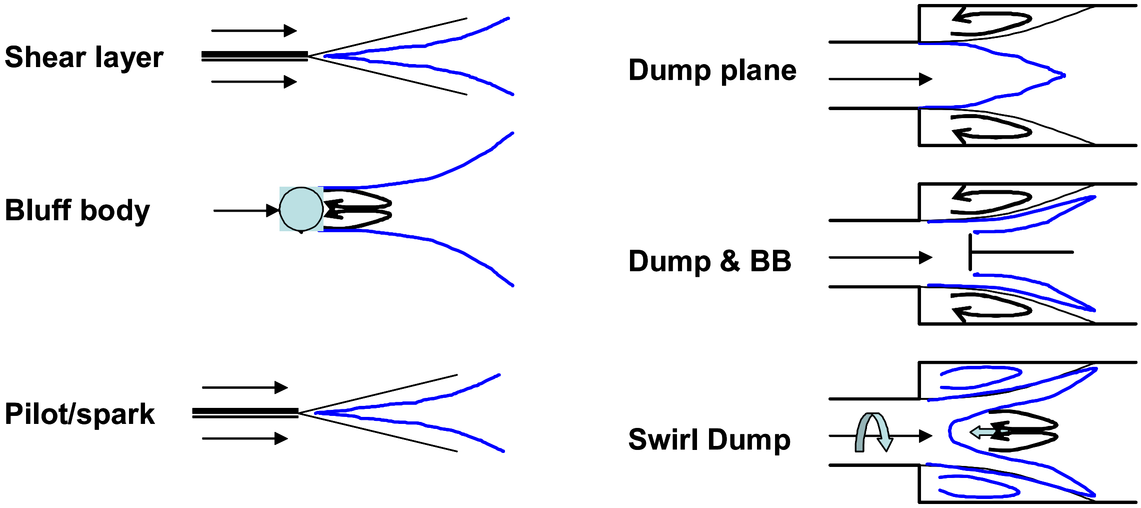

Figure 4. Various forms of flame stabilization and their main mechanisms.

In the case of shear-layer-stabilized flames (e.g., jet flames), the flame is stabilized due to the low velocity region created by viscous diffusion (see Figure 4). At high flow rates, the low velocity region may occur too close to a wall, where the radical and heat losses may be high; thus the flame speed drops and the flame cannot be stabilized.[39] Jet flames stabilization can be improved if the depletion of radicals and heat can be replenished by a secondary flame ("pilot flame") very close to the lip of the jet (see Figure 4). This can also be achieved with other mechanisms like electric discharges, which create localized plasma that can supply additional thermal energy and high energy radicals to sustain a reaction.[40-42]

A popular passive method for stabilizing a flame in high speed flow is to design recirculation zones into the flow. The recirculation zone can be created by several methods including bluff body wake, sudden area changes (a ‘dump’), swirl, a trapped vortex and a combination of these methods (see Figure 4). The main physical reason for stabilization is the feedback of radicals and heat from the burned products.[3] This depends on recirculation zone residence times, radical lifetimes, heat/radical losses to any nearby walls, and the mixing between the fluids in the recirculation zone and the outer regions.

Well-stirred reactors have been used to model the effect of recirculation zones, and the approach has been quite successful in predicting trends in stabilization limits and their relationship with residence times.[3] Further improvements to this model were achieved by the partially stirred reactor, which simulates the imperfect mixing in practical combustors.[43] A circuit of well-stirred reactors and plug flow reactors have also been used to model complex combustors to simplify their characterization.[3]

The space constraint for many practical combustors restricts the length available for the combustion chamber. Adding swirl to the flow increases the residence time since the fluid now takes a helical path instead of straight path through the combustor and thus helps ensure higher combustion efficiency within a shorter length combustor. Addition of a sudden expansion in the flow area (called a dump region) decreases the flow velocity and also adds a corner recirculation zone which provides the feed back of hot products and radicals. The configuration of swirl and dump stabilized combustors is the most common stabilization method used in modern gas turbine combustors. Swirling flows are characterized by the strength of the swirl, given by swirl number, S, defined as the ratio of tangential momentum to the axial momentum of the flow at the inlet of the combustor. Flows with high swirl numbers have the added advantage of vortex breakdown and have an inner recirculation zone, which again helps in stabilizing the flame.[44] This swirl flow feature will be discussed in detail in the following section.

Several modes of flame shapes have been observed in premixed swirl dump combustors. Average flame shapes are illustrated in Figure 5. The flame shape in case (a) occurs at fuel-to-air ratios close to stoichiometric. Case (b) occurs in leaner mixtures; the outer recirculation region due to the dump plane loses the flame and only the inner flame is present. The flame also is longer due to the lower flame speed. Case (c) occurs when the mixture is very lean, and by eye, it resembles a tornado funnel. There are a handful of studies that cover these flame structures, and experimental data is also available on the average velocity, temperature and heat release distributions.[45]

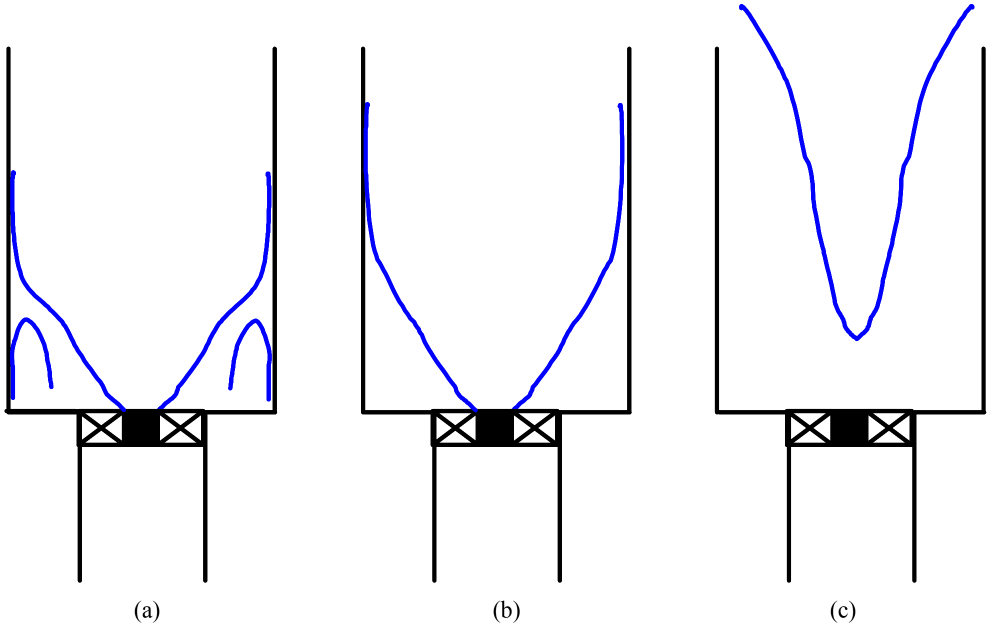

Figure 5. Various flame shapes observed in a simple swirl-dump combustor. (a) Flame stabilized in both outer and inner recirculation zones, occurs near stoichiometric mixtures (b) flame stabilized only in the inner recirculation zone, and (c) “tornado” like flame, which appears at very lean mixtures.

More advanced combustion systems have several variations to this swirling flow with area expansion. There are multiple swirling streams providing co- and counter-swirl to the flow. The shear in between the counter swirling streams is typically used to break apart liquid fuel droplets and it also help to mix the fuel rapidly after injection. The geometry can also have a quarl that shapes the flow and helps form recirculation zones. In this dissertation, understanding the swirling flow dynamics is important to understand the dynamics of swirl flow with combustion.

2.3 Swirling flow dynamics

Flow physicists have been studying swirling flows over several decades. The studies of interest to this work are related to vortex breakdown phenomenon in swirling flows. Historically vortex breakdown has been observed first on flow over a delta wing, which has two concentrated lines of vorticity leaving the edges of the wing. These vortex lines, flow along the streamlines at low angle of attacks. When the angle of attack of the delta wing is increased, the vortex lines experience a sudden change in shape, redistributing the vorticity in the core into three dimensions. This is referred to as vortex breakdown. For aerodynamicists, the motivation is to avoid vortex breakdown, as it results in decreased efficiency from lifting surfaces in aircraft, while the combustion engineers is interested in the use of vortex breakdown for stabilization. Flows with high swirl numbers and Reynolds numbers (*Re*) have been found to be more susceptible to vortex breakdown.[44] This happens when the local tangential velocity in the flow becomes greater than the axial flow velocity. Vortex breakdown is triggered by a disturbance that causes the axial momentum to be distributed into radial direction, e.g., sudden expansion.

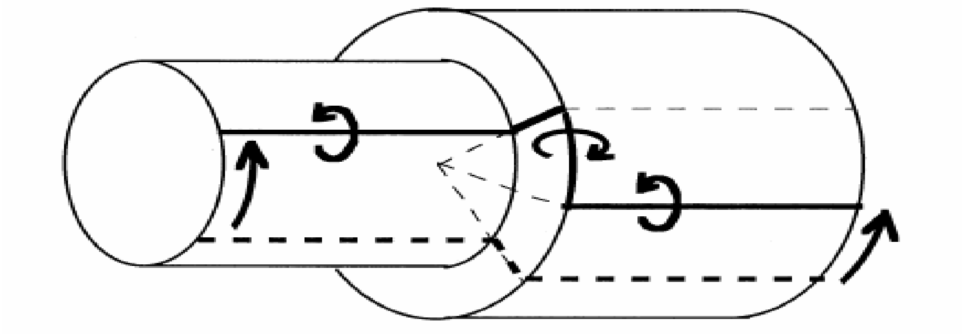

Figure 6. Azimuthal vorticity production by radial vortex tube expansion. The schematic shows the sense of the azimuthal vorticity produced through spiraling of vortex lines. The axial flow is from left to right. Figure adapted from Umemura and Tomita.[46]

A sudden decrease in the axial velocity causes redistribution of momentum in the radial direction. Figure 6 illustrates the production of azimuthal vorticity through sudden area change in the flow. The vortex lines that constitute the vortex tube are stretched and tilted due to the increase in the cross section area of the vortex tube.[46] This causes redistribution of axial vorticity into azimuthal direction resulting in an induced reverse flow near the axis of the flow. This induced reverse flow if sufficiently strong can result in a central recirculation zone in the mean flow field in a toroidal shape. This central recirculation zone is helpful in stabilizing the flame by providing feedback to the incoming gases. In a typical gas turbine combustor, both inner recirculation zone and sudden expansion are used to stabilize the flame at the high combustor loadings required (see Figure 5).

Vortex breakdown in swirling flows has been studied for over fifty years and is still a research topic among the fluid mechanics researchers.[44,47-49] However, their work has focused on non-reacting, low *Re* flows, often in water for ease of visualization.[50] Vortex breakdown is observed when there is an adverse pressure gradient in the axis of the flow and the point of breakdown is determined by the strength of swirl, the Reynolds number and the pressure gradient. There are several vortex breakdown (VBD) modes that have been observed including bubble and helical types, depending on swirl strength and Reynolds number.[47,51]

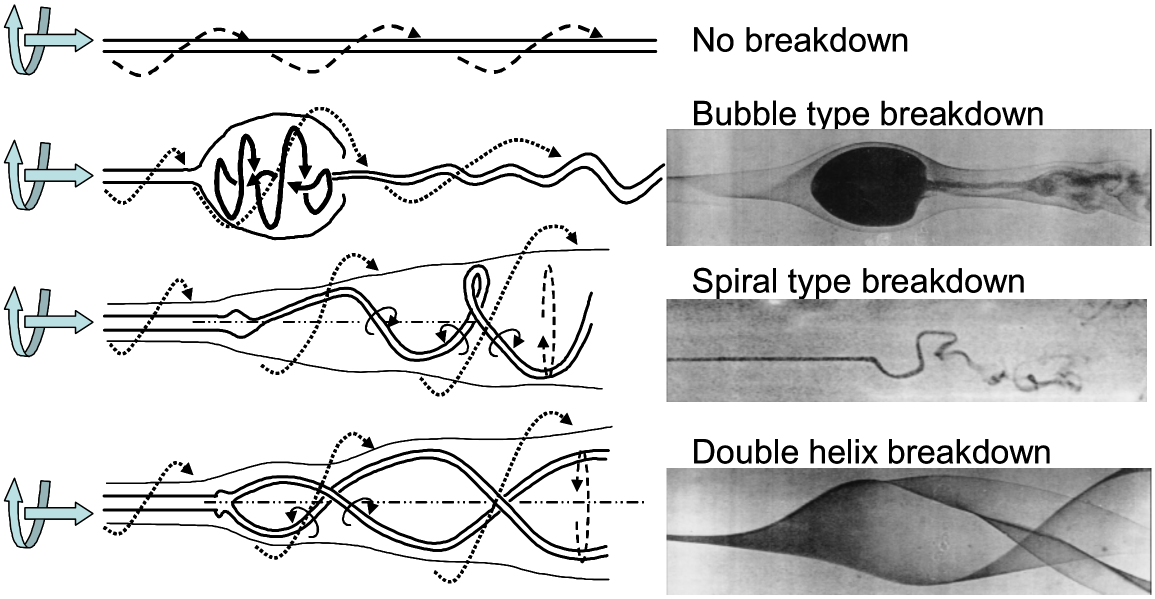

Figure 7. Illustration and dye flow visualization of most common vortex breakdown modes.

2.3.1 Bubble type VBD

The first type of breakdown relevant to this work is the bubble type (see Figure 7) in which there is a toroidal vortex near the axis of the flow just past the breakdown point; the majority of the oncoming flow goes around this bubble. This bubble type vortex breakdown is used in combustion chambers to increase flame stability[44] and is referred to as the inner recirculation zone. This bubble structure is nearly axisymmetric and there is an exchange of fluid with the surroundings near the downstream end of the bubble (see Figure 8). Sarpkaya[47] explains this as simultaneous filling and emptying through the toroidal vortex ring located near the downstream end of the bubble.

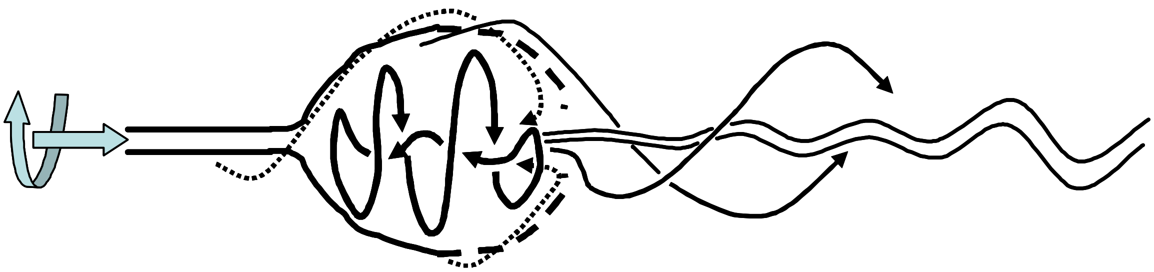

Figure 8. Illustration of pathlines for bubble type vortex breakdown showing exchange of fluid across the bubble surface.

Shown in Figure 9 (reproduced from Sotiropoulos *et al.*[52]) is the flow structure, the pathlines in and around the bubble, and the evolution of fluid particles in the bubble. The first depiction, Figure 9(a) shows the general structure of the vorticity field. Figure 9(b) shows fluid particles that just go around the bubble, as well as particles very close to the bubble that enter the bubble and take a long time before finally leaving the bubble. Figure 9(c) shows the time evolution of particles that are lined up on the surface of the bubble. As seen in this figure, particles go around the bubble and enter from the downstream side of the bubble. It also shows the toroidal vortex structure entraining the particles into the bubble. The particles that leave the bubble leave mainly through the center of the downstream end of the bubble.

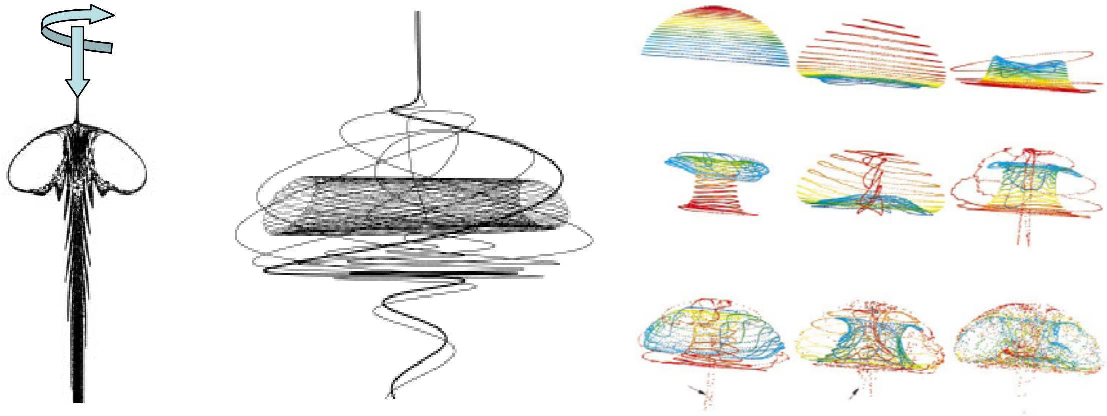

Figure 9. Illustration of pathlines and flow patterns in a bubble type vortex breakdown. These images are adopted from Sotiropoulos *et al.*[52] (a) general structure of the vorticity in bubble type VBD, (b) The path lines inside and outside of the bubble, (c) time evolution of particle distribution inside the bubble. The top left image in (c) is the initial distribution of the particles. The time sequence of these images is from left to right and top to bottom. The particles are convected into the bubble from the downstream end of the bubble. The particles that leave the bubble are not shown in these images.

2.3.2 Spiral/helical breakdown

The second VBD mode of interest is the helical mode, where the axial vorticity is redistributed into single/multiple helixes (see Figure 7) after the point of breakdown.[53] The exact number of helical structures depends on the *S* and *Re*, with more helical structures for higher swirl.[51] As *S* is increased for a given *Re*, helical disturbances[i] in the flow cause the vortex core to go off axis and spin along the flow direction. The sense of rotation of the spiral has been observed to be both along and against flow swirl.[53] But if the disturbances are strong enough, the sense of winding of the helix assumed is that against the swirl direction. As discussed earlier (see Figure 6), this causes an induced reverse flow along the center line of the flow field.

Figure 10 from Ruith *et al.*[51] shows particle paths for increasing S for a given Re and vice versa. In both the cases, the starting case is bubble breakdown, which can sustain

---

[i] Any three dimensional disturbance with an axial velocity component can be decomposed into an axisymmetric and a set of helical components. Flow physicists often use the term helical disturbances for non-axisymmetric disturbances

low levels of helical disturbances. As Re (or S) is increased, the flow becomes more susceptible to helical disturbances, and the breakdown mode switches to the spiral mode. As Reynolds number is increased further, the spiral mode becomes the double helical VBD mode.

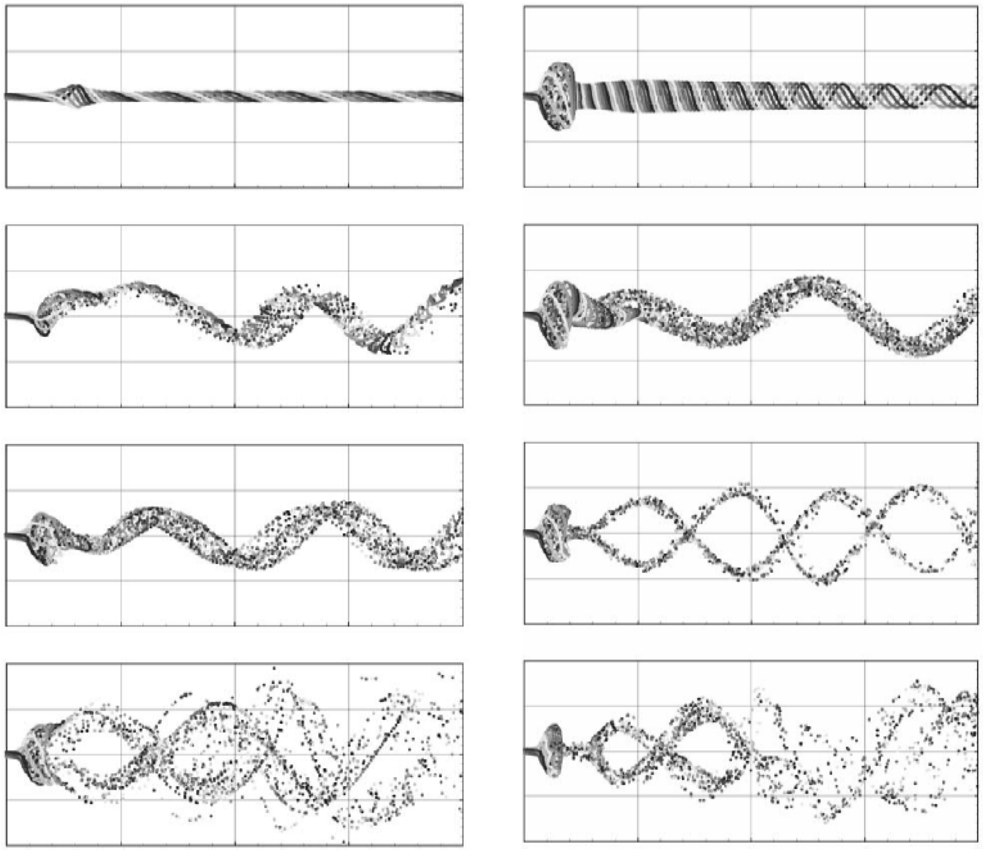

Figure 10. Effect of swirl and Reynolds number on VBD mode. The left column corresponds to constant Re of 200 with S increasing top to bottom (S=0.9, 1.0, 1.1, 1.3). The right column corresponds to constant S of 1.3 with Re increasing from top to bottom (Re=100,120,150, 300). Figure adopted from Ruith *et al*.[51]

Figure 11 shows the time evolution of fluid particles in the double helical VBD mode. The helical structures carry the particles and also rotate about the axis of the flow. This essentially appears as two helical structures wrapping and rotating around each other. The point of breakdown seems to have a small cone like structure, which appears to be stationary. Each of the spirals carries fluid particles downstream, while the whole structure is rotating about the axis. The instantaneous shape of the spirals (as seen from the location of the fluid particles) appears to be distorted at several points in time.

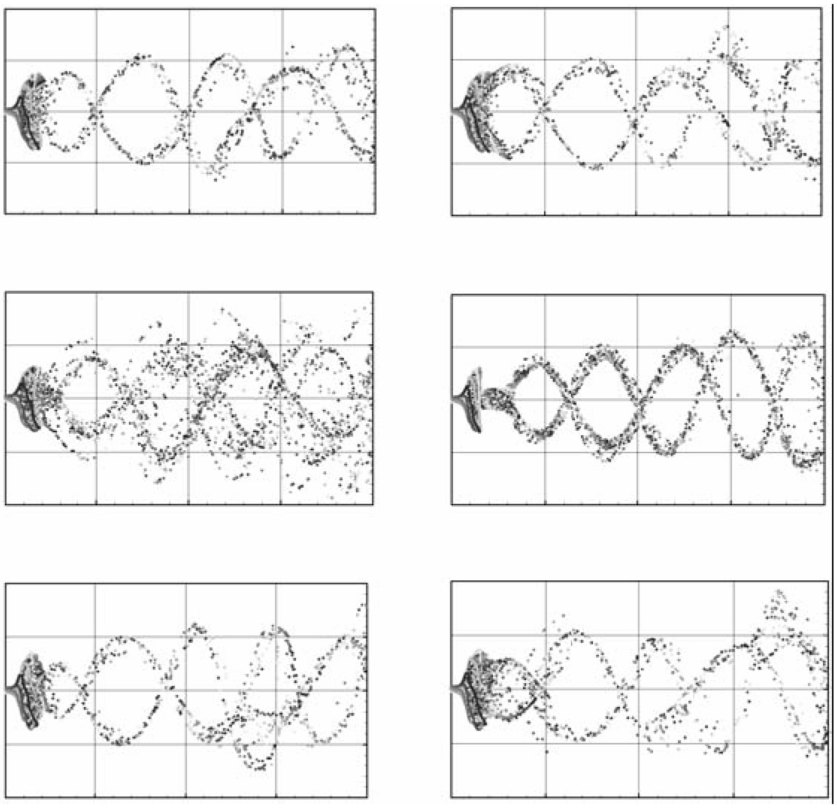

Figure 11. Figure to show that the double helix structure rotates in time. Figure from Ruith *et al.*[51]

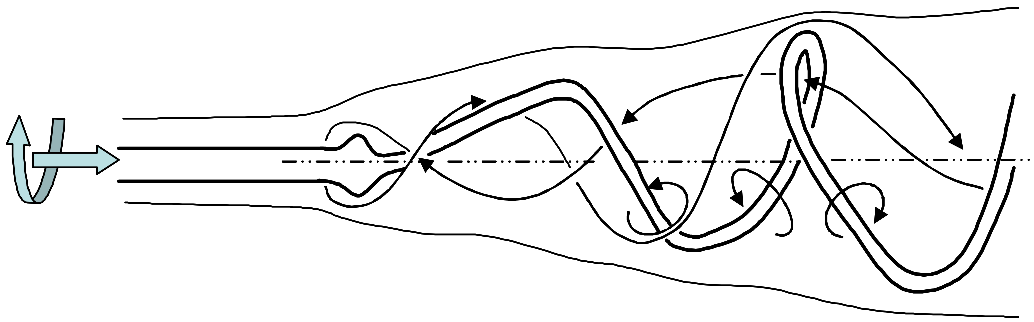

Figure 12. Illustration of instantaneous streamlines around a spiral vortex core. This illustration does not take into account the effect of rotation of the helix about the central axis (dotted line). In an average sense, there is a negative velocity on the inside of the cone formed by the rotating vortex core, and positive on the outside of the cone, with spiraling streamlines due to the swirl component of velocity.

Figure 12 shows an illustration of the helical vortex breakdown with one spiral. The sense of overall flow swirl is shown on the left. The sense of winding of the spiral is opposite that of the sense of the flow, while the vorticity along the helical coils is still the same sense as that of the original flow. This induces negative (reverse) velocities in the fluid inside of the cone enveloped by the spiral. The figure also shows a pathline based on the current location of the helix (not considering the helix rotating about the axis, in time). The streamline spirals upstream on the inside of the cone and spirals downstream on the outside of the cone. This behavior on a time average sense might look like an elongated recirculation zone in the axial velocity contours, with a cone shape. Although not shown here, not all streamlines need to reach the tip of the cone; they can turn around at any axial location if it gets close to the vortex core (shown as a thick double line in the figure). Thus there will be several points in the flow with zero axial velocity and there will be a region with negative axial velocity.

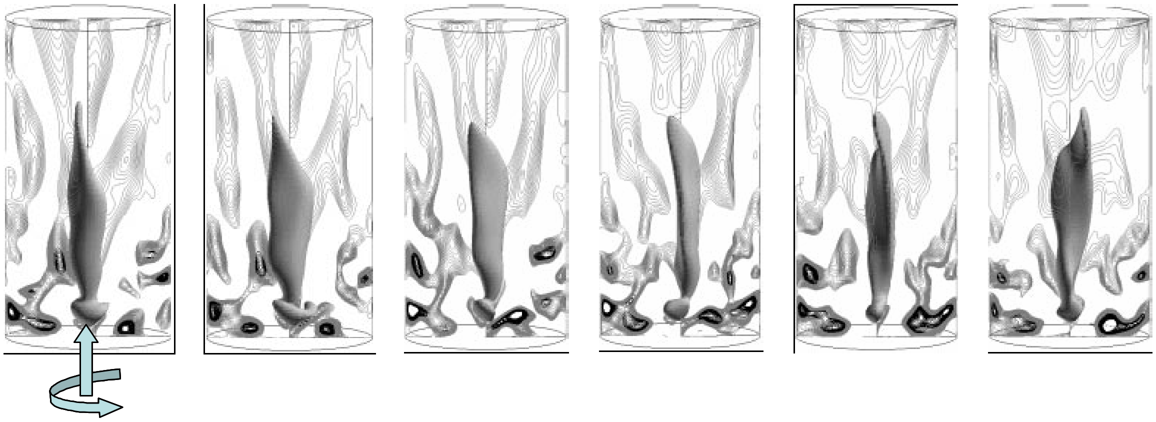

Figure 13. Time evolution of the isosurface of zero axial velocity in a spiral VBD. The thick-leaf-like isosurface rotates about the axis of the tube. The velocities inside of this surface are negative. The bottom most point in the surface (axial stagnation point) is off axis and is rotating about the axis.[56]

Figure 13 (reproduced from Serre and Bontoux[56]) shows the isosurface of zero axial velocity in a spiral type vortex breakdown. It can be noted from the figure that the shape of this contour roughly appears like a thick leaf-like structure with a bulb at the bottom. The breakdown point still has a small bubble like structure. The whole structure appears to rotate around the axis. The reader can imagine this contour as an envelope with all the fluid with negative axial velocities inside of it. It can be noted that the flow at a point near the downstream end may have negative or positive velocity depending on whether this point is inside or outside of the surface, at that instance. Also to be noted is that the axial stagnation point near the axis (the bottom of the bulb) is off axis and is rotating about the axis.

2.3.3 Double helical VBD mode

As discussed earlier, there can be more than one helical structure in the breakdown depending on the flow conditions. The flow field becomes more complex in these conditions. Mathematical tools like proper orthogonal decomposition of the vorticity field have been used to show the structure of the main helical vortex core.[51] Shown in Figure 14 is the isosurface of the absolute value of vorticity in the flowfield in the primary mode alone, for a double helical vortex breakdown mode. This shows that the double helical mode has alternating positive and negative vorticity structures rotating around each other. The velocity field induced by this structure will also appear to be similar in shape. It will appear to be a set of alternating positive and negative axial velocity spirals rotating about one another.[54-56] The instantaneous flow field in the double helical mode is complex and will not be explained here. But the inference from this section is that the double helical structure has several negative velocity helical paths.

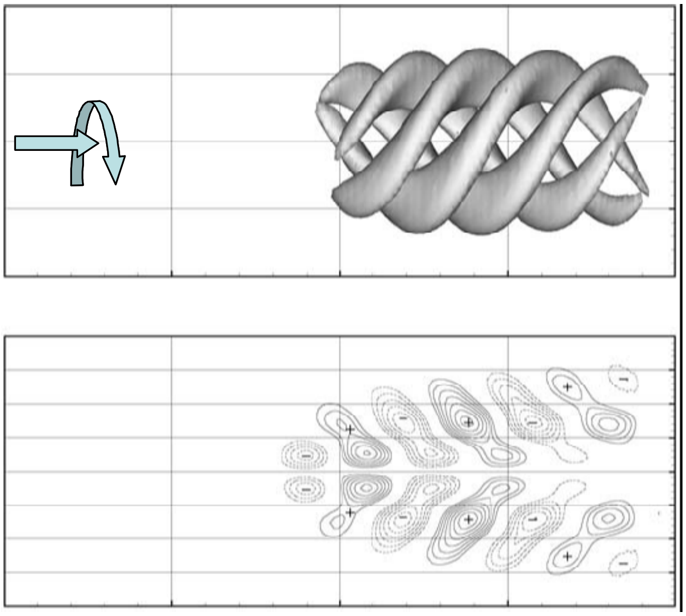

Figure 14. Isosurface of vorticity modes in the double helix mode. Also shown is the vorticity contours in the central cross section plane of the flow field. Figure adopted from Ruith *et al.*[51]

2.3.4 Transition from bubble to spiral VBD

In this dissertation it will be shown that there are both bubble and spiral type VBD observed close to blowout of the combustor. Thus it is necessary to understand the transition between these two modes of VBD. The various modes of vortex breakdown have been observed to evolve from one another depending on the flow geometry, Reynolds number and swirl number. The bubble breakdown may evolve directly from an axisymmetric swelling of the vortex core, or from spiral or double helix vortex breakdowns.

The presence of an adverse pressure gradient can accelerate the formation of the bubble type vortex breakdown from a helical breakdown. The adverse pressure gradient decreases the axial component of the velocity and increases the radial component of the velocity. As discussed earlier, this results in redistribution of the axial vorticity into circumferential vorticity. The induced velocity due to this circumferential vorticity at the axis is a further negative velocity. Thus this feedback loop results in a mode shift from spiral to bubble type vortex breakdown mode.

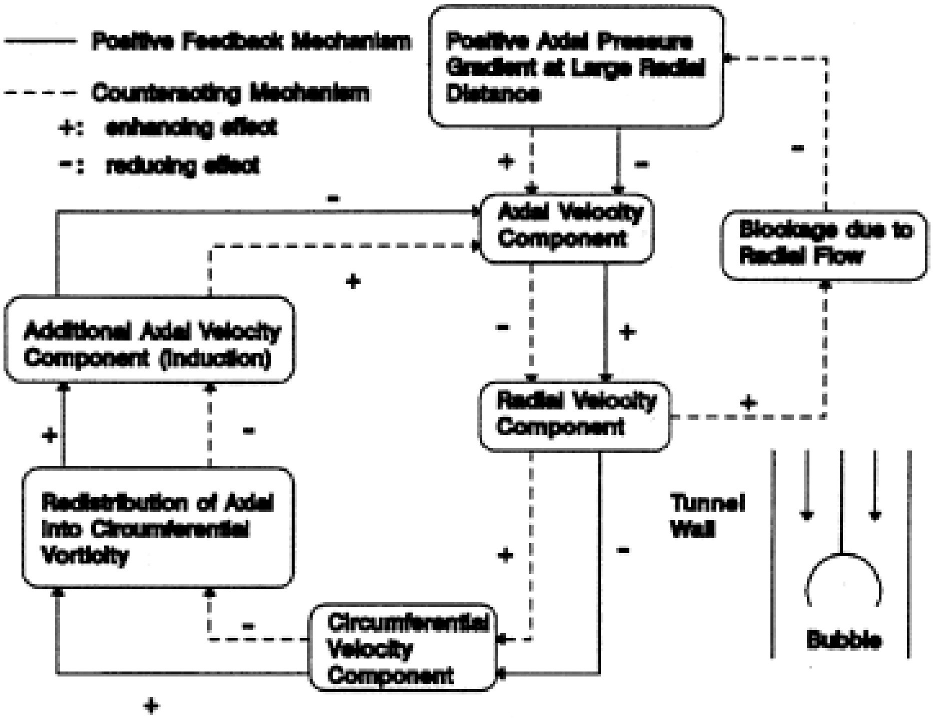

Figure 15. Figure showing the diagram for feedback loop for formation and disintegration of bubble type vortex breakdown mode.[44]

When the pressure gradient is decreased, the reverse of the feedback loop can occur and a bubble type can transition into a helical type VBD. The axial velocity increases decreasing the radial velocity and thus decreases the redistribution of axial vorticity into circumferential vorticity. This decreases the axial induced negative velocity, and thus further decreases the strength of the toroidal vortex. This results in the flow now being susceptible to helical disturbances in the flow and the vortex core now transitions into a spiral/helical type VBD. Figure 16 shows the transition process from spiral to bubble and from bubble to spiral type VBD. It can be noted that the bubble is formed from the axisymmetric swelling followed by an umbrella like structure that folds over several times to form the bubble. In case of transition from bubble to spiral mode, the bubble appears to become more and more asymmetric and evolves into a spiral.

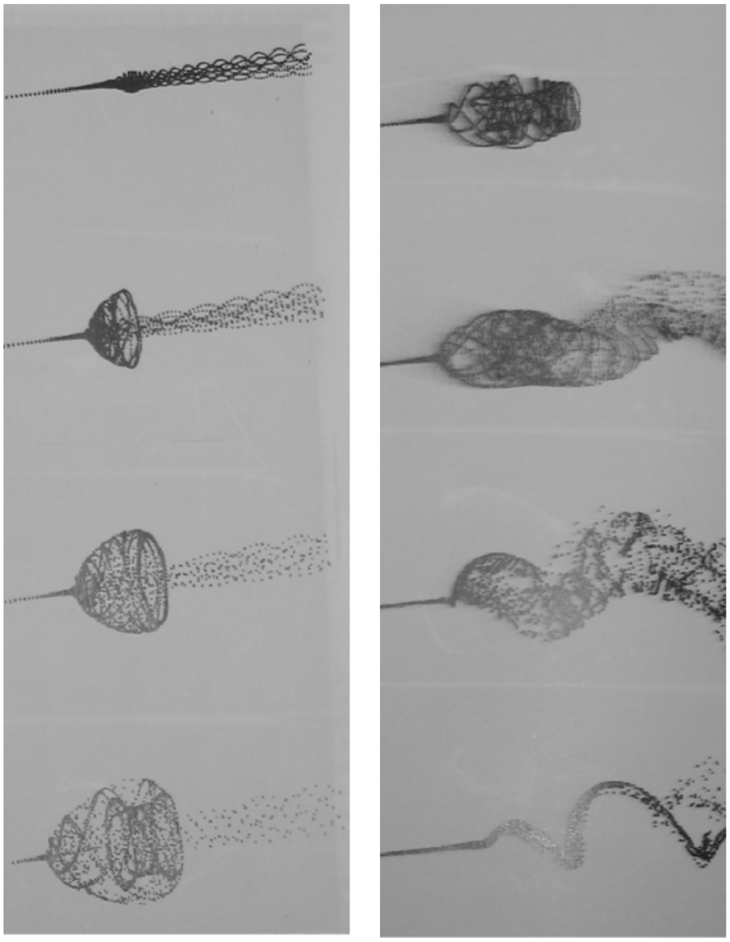

Figure 16. Visualization of transition of vortex modes from numerical simulation results.[57] The figure on the left shows the transition from spiral to bubble mode, while the figure on the right shows transition from bubble to spiral mode. Images adopted from Althaus and Weimer.[57]

The bubble type breakdown occurs in non combusting flows for low swirl and Reynolds numbers. It transitions to spiral and then to double helical breakdown as either *S* or *Re* is increased.[51,57] The spiral mode is very unstable but can be stabilized in careful experiments with specific boundary conditions. The helical modes are the most stable and the only type observed at high Reynolds numbers as the other modes are unstable to small perturbations that are abundant in turbulent flows.[58,59] Bifurcation characteristics are observed at the transition between these modes of vortex breakdown.[56,60] Increasing the vortex core axial velocity more than the coflow velocity around the vortex core can cause the helical mode to transition to a bubble mode. Conversely, decreasing the core velocity below the coflow velocity can cause the bubble type breakdown to transition into helical breakdown.

2.4 Swirl flows with combustion

In reacting swirl flows, the spiral breakdown mode has been observed in combustors with low heat release and has been referred to as the precessing vortex core.[61] It has been observed that the precessing vortex core is prevalent only in weak heat release cases and is suppressed by higher heat release.[62] Swirling flow with sudden expansion, as used in gas turbine combustors, can produce several flame shapes based on the heat release, swirl and velocity in the combustor.[45] The observed average flow fields in cold and hot flows are different due to the dilatation from heat addition. The presence of the swirl-induced vortex core is suppressed by combustion and the dilatation, which makes the inner recirculation zone (IRZ) smaller for the case with combustion.[63,64] It is also observed that the turbulent kinetic energy and the velocity fluctuations are increased substantially due to combustion.[65] Syred *et al.*[66] found that at very high S (>2.2) there is little change in flow field due to chemical reactions.

Recent work has concentrated on understanding the dynamics of this complex flow field using both numerical and experimental methods. Although the mean flow shows a central toroidal vortex, the instantaneous flow field is observed to have smaller vortical structures, which help in mixing.[67] Adding heat release to a near critical swirling flow has been analytically shown to cause a decrease in the critical swirl for breakdown.[68] Also the bifurcation behavior has been shown to be altered by the presence of weak heat release. The solution branch was found to be double valued for near critical swirl values and thus two solutions are simultaneously possible for a given swirl and heat release.

2.5 Flame behavior near blowout

The behavior of flame in swirl combustors near blowout is the topic of interest in this dissertation. One of the first detailed works on loss of stabilization of flames was by Lewis and Von Elbe.[39] They found that the velocity gradient at the wall/lip of the burner was important in determining the stability of the flame. Several researchers following their lead studied the loss of static stability of flames. Jet flames and bluff body flames were observed to lose its stability in an intermittent, sporadic and non-symmetric fashion.[10,11,13] The flames generally pulsate at a low frequency (~10-200 Hz) for several seconds prior to blowout.[12]

It is generally accepted that high magnitudes of strain are a cause for local extinction of flames.[17,27,69,70] It is observed that extinction of flame depends on instantaneous value and the history of the strain experienced by the flame.[18,20,71,72] When a flame is periodically forced to exceed extinction strain rates, the flame weakens gradually eventually extinguishing after several cycles. Many turbulent flames develop small holes at random locations that grow in size until the whole flame is extinguished.[14,73] In turbulent flow fields these local holes of the flame may be caused by strain rates caused by turbulent perturbations. In a turbulent flow these holes caused would appear and disappear at random locations depending on the strain field at any instant. In more complex flames, e.g., gas turbine combustors, the flame extinctions and reignitions appear to oscillate between two flame shapes prior to blowout.[19,21,74]

Chapter 3

Experimental Methods

This chapter describes the various experimental setups, diagnostic methods and data analysis procedures used in this study. The first section describes the combustors that were used in this study. The second section describes the instrumentation used for data acquisition and movie recording. The third section describes the control experiment setup. The final sections describe the procedures, including the image processing procedures, used for analysis and presentation in this dissertation.

3.1 Combustor

The experiments were performed in an atmospheric pressure, premixed, swirl-stabilized dump combustor, which is the basic configuration of most gas turbine combustors. A schematic of the combustor is shown in Figure 17. The overall combustor configuration was chosen as a simplified model of a lean, premixed, gas turbine combustor that includes a swirling inlet section. Premixed gas, consisting of gaseous fuel (methane or natural gas) and air flows through swirl vanes housed in a 23 mm i.d. tube. The combustor wall is formed by a 127 mm long quartz tube, which permits uncooled operation of the combustor and facilitates detection of ultraviolet (UV) radiation. The quartz tube has an inner diameter of 70 mm and an outer diameter of 75 mm. The quartz tube rests in a circular groove (thickness 4 mm and depth of 6 mm) in a base plate made of ¾” thick aluminum.

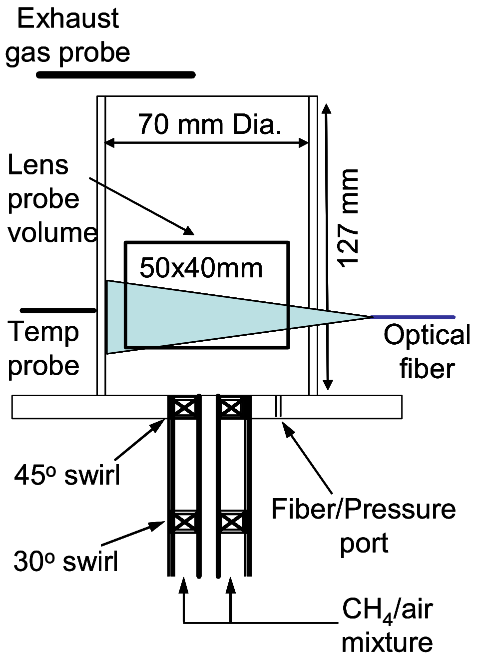

Figure 17. Schematic of combustor with probe volumes for the lens system and optical fiber used.

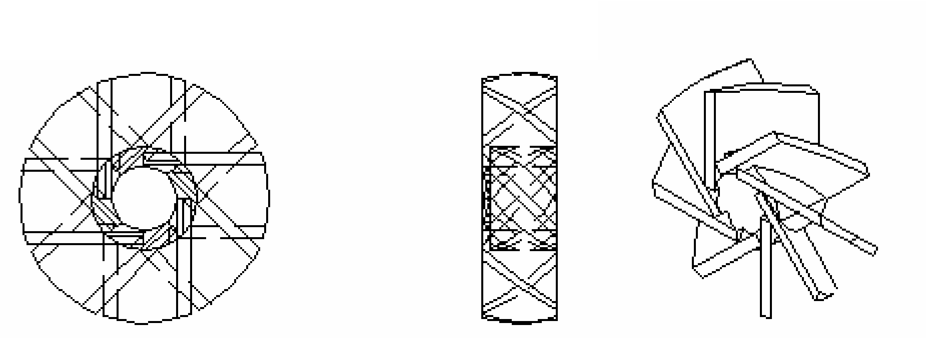

Figure 18. Drawing of the swirlers used in this study.

The swirler consists of two sets of vanes, 30° followed by 45° (see Figure 17) causing the exit flow to have a (theoretical) swirl number of 0.66.[75] The two-stage swirl design was used to ensure that the swirl number was close to the theoretical values reported in the study. The flow separation that may occur across the swirl vanes is decreased by this staged swirl generation. The swirlers are spaced by about 100 mm, and drawings of them are shown in Figure 18. The swirlers are made of brass for ease of machining and because of its temperature capability. The outer diameter of the swirlers is 23 mm so as to have a tight fit into the flow tube. The inner hole diameter (6.3 mm) allows a ¼" OD tube to fit through it. The premixed gases flow through the annular region between the inner tube and the flow tube. The swirlers are 6.3 mm thick, with an inner hub that is 1 mm across. The swirl vanes are flat blades, with each blade roughly 1 mm thick, and they are not twisted. The angles of the vanes referred to in this study are the angle of the flow vector with respect to the axial direction. The area through the swirler at the exit plane is calculated to be 15.5 cm^2.

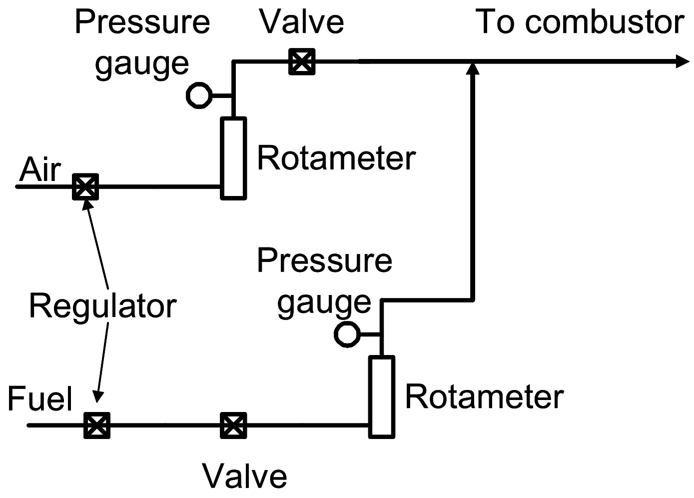

Figure 19. Schematic diagram of the flow control and monitoring system.

Figure 19 shows the schematic of the flow control/monitoring system. The air and fuel flows were double choked to ensure flow rates remained constant during the experiments even in the presence of combustor fluctuations. An upstream regulator, which sets the pressure, provides the first control, while the downstream control is a valve to set the flow rate. Flow rates are measured by a rotameter and pressure gauge in each of the flow paths. The fuel is supplied from a pressurized methane bottle, except in the case of natural gas experiments, where the fuel comes from the building supply (at

25 psig). Experiments with natural gas supplied at low pressure could not ensure constant flow rates during data acquisition, since the flow was not double choked. Most of the results presented in this study use high pressure (bottled) methane for this reason. The flow control and monitoring system has a resolution that is equivalent to a change in equivalence ratio (ϕ) of approximately 0.003. A thermocouple (see Figure 17) was used to monitor the change in the temperature of the combustor wall, as this by itself can cause LBO limit to change. For most cases, the external wall temperature was in the range 400-500 K. The data presented in this study correspond to a bulk average axial velocity in the combustor of around 4.5 m/s in the combustor under cold conditions. Assuming complete combustion, the average axial velocity of the product gases would be ~30 m/s. However, other axial velocity cases (2-6.5 m/s) were also used for certain experiments.

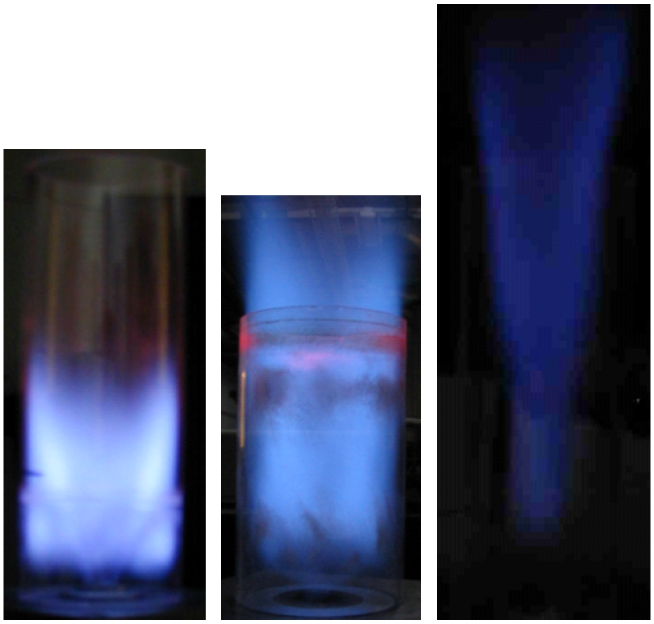

Compact flame V-shaped flame Tornado flame

Figure 20. Digital photographs of various flame modes observed in the combustor. The equivalence ratio decreases from left to right. The tornado flame exists only in high aspect ratio tubes.

The combustor was mainly used in the configuration described above. However, quartz tubes of multiple diameters (70 and 115 mm) and lengths (200, 120, 80 and 75 mm) were used in the study. Figure 20 shows photographs of various modes of the flame observed in the combustor. The compact flame exists for near stoichiometric equivalence ratios. The V-shaped flame is similar to the compact flame except the outer recirculation zone does not show any flame, and the overall flame is longer. The tornado flame is a very thin and weak flame that exists only at very low equivalence ratios, and only in long (high aspect ratio) tubes. This flame extends well beyond the exit of the tube. The shape appears like a funnel of a tornado, thereby suggesting the name. These flame shapes were also observed by Bradley *et al.*[45] in a similar combustor.

Table 1. Various flame modes for a 70 mm diameter tube with varying lengths and equivalence ratios for 6 m/s average cold flow velocity.

Tube configuration	Equivalence ratio	Flame mode
200 mm long	0.89	Compact flame
200 mm long	0.86	V-flame
200 mm long	0.79	Tornado flame
200 mm long	0.68	Blowout
120 mm long	0.89	Compact flame
120 mm long	0.86	V-flame
120 mm long	0.78	Blowout
80 mm long	0.89	Compact flame
80 mm long	0.85	V-flame
80 mm long	0.82	Blowout
75 mm long	0.89	Compact flame
75 mm long	0.87	Blowout

Table 1 gives the type of flame shape observed for a combustor with 70 mm diameter tube for different lengths and equivalence ratios. In this set of data, the air flow rate was fixed to have a value of 6 m/s average cold flow axial velocity and the equivalence ratio was decreased from stoichiometric condition to blowout. The compact mode was observed near stoichiometric value. The equivalence ratios shown for the non-compact flame modes are the highest equivalence ratios where that mode was observed. As the mixture is made leaner, the flame mode shifts from compact to V-shaped mode to tornado mode to blowout. In case of shorter tubes, the flame blowout occurs at higher equivalence ratios.

A liquid fueled, preheated air, partially premixed swirl dump stabilized annular sector combustor was also used in this study. This CFM56 single cup combustor uses a burner head with co-annular, counter rotating swirlers. The standard fuel nozzle was replaced with a pressure-swirl atomizer. The combustor air comes from an air plenum chamber fed by electrically heated air (~400 K). The test-section is optically accessible through quartz side walls. The combustion gases exit through a small converging nozzle to provide a more realistic boundary condition. The fuel used for these experiments was Jet-A aviation grade petroleum.

3.2 Instrumentation

Several types of instrumentations and diagnostic methods were employed in this study. The chemiluminescence emission from the flame was collected by a fiber optic based sensor developed in this study. The dynamics of the flame were observed by high speed visualization of chemiluminescence and droplet scatter imaging. In most high speed imaging experiments, simultaneous chemiluminescence data was recorded from the fiber sensor. Some of the experiments involved simultaneous NOx emissions measurements.

The signal output from the sensors was low pass filtered by a Krohn-Hite Model 3362 digital Butterworth filters and then fed into a 12 bit National Instruments A/D board. The sampling frequency varied with experiment and will be provided in the respective sections. The low pass filter frequency (for anti-aliasing) was set at half the sampling frequency. Typical sample sizes were of the order of 2^{16} data points to facilitate ensemble averaging and minimize bias error. LABVIEW, a graphical programming language by National Instruments, was used for data acquisition. A program written in LABVIEW processed the data collected on the A/D data acquisition board, and displayed and stored all the relevant information. All the electronics were grounded to minimize electrical noise. Sheathed BNC cables were also used to minimize cable noise.

The collection volume for the chemiluminescence optics is indicated in Figure 17. The lens based collection employed a simple spherical lens and a rectangular aperture to pick the required collection volume. The collection volume was roughly a rectangular cross section of 40x50 mm with line of light integration of light. This volume was placed such that light is collected from the brightest region in the combustor. The fiber optic collection setup employs a 365 μm diameter fused silica optical fiber. The fiber has an acceptance cone half-angle of about 12°. The collected radiation passes through an interference filter, centered at 308 nm and with a full-width-half-maximum (FWHM) of 10 nm, which corresponds to the primary spectral region for the OH $A^2\Sigma$-$X^2\Pi$ electronic transition. The collected OH emission is detected by a miniature, metal package PMT (Hamamatsu H5784-04). This PMT has a built-in amplifier (bandwidth of 20 kHz) to convert the current to voltage and operates from a 12 VDC source.

To help understand the dynamics of the near blowout dynamics of the flame, a high-speed intensified camera (Videoscope International, Ultracam3) was employed. The camera has a 512×512 CMOS sensor and can record at a rate up to 1000 frames/sec (fps) at this resolution. The image intensifier (GEN III) in the camera has a response from 200 - 700 nm with a gate duration as short as 50 ns. In conjunction with the glass camera lens employed, the camera is sensitive to all the visible light emitted by the combustion gases. Simultaneously, the chemiluminescence from the combustor was also collected by a fiber optic probe placed 40 mm from the center line and 40 mm above the inlet.

Flow visualization experiments using laser sheet scattering from oil droplets were also performed. The air stream was seeded with olive oil droplets using a laskin nozzle[76] based droplet seeder. The seeding system had two nozzle assemblies with four holes of 1 mm diameter. The seed droplets produced are less than 1.2 μm in diameter[76] and thus can follow the flow with a frequency response of 10kHz.[77] A part of the airflow was sent through the seeder and was mixed with the rest of the air before premixing with the fuel. The droplets were illuminated by a 510 nm wavelength laser sheet formed from a copper vapor laser (Metalaser Technologies, Inc, MLT-20). The laser was operated at 5.7 kHz with a 5 W average power (< 1 mJ/pulse), and the laser sheet was 89 mm (3.5 in.) in height. In the droplet scattering experiments, a 510 nm bandpass interference filter (10 nm bandwidth) was placed in front of the camera to remove the flame emission, and the camera was triggered once every three laser pulses (at 1.9 kHz) with a gate duration of 60 nsec. Since the oil droplets are an additional source of fuel, the LBO equivalence ratio based on just the methane-air composition is not the same in both cases. The LBO limit occurred at an equivalence ratio of 0.73, while the droplet seeded flow LBO limit was 0.68.

Exhaust gas analysis was carried out using a LANCOM series II portable flue gas analyzer (Land Instruments International Ltd.). The manufacturer reports this system has an accuracy of ±1ppm for NO and CO measurement when properly calibrated.

3.3 Control setup

This section describes the various components of the setup used in experiments involving control of combustor blowout. A schematic of the flow system is shown in Figure 21. Both fuel and air lines are double choked before the spilt between main and pilot lines, and thus the total flow rates can be maintained at constant values throughout the experiment. The split between the pilot air and the primary air was fixed at a constant value throughout this study.

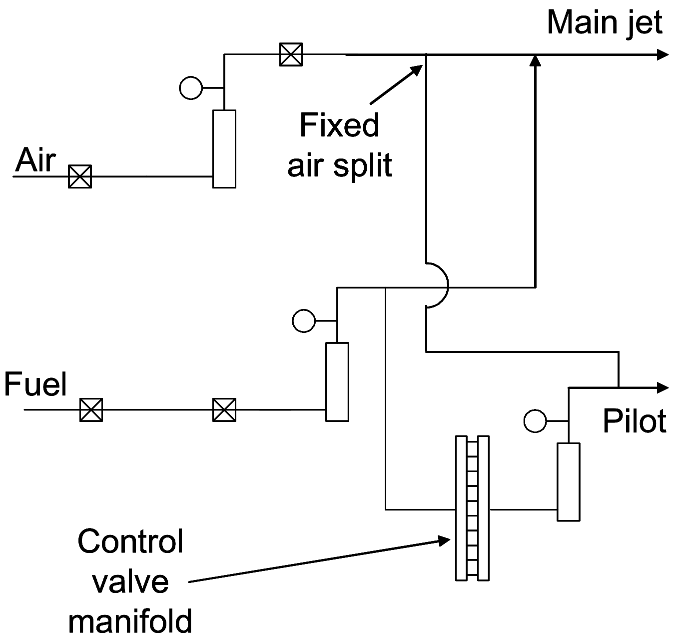

Figure 21. Schematic of the flow system with controllable fuel split.

For steady operation, the split of the fuel between the primary and the pilot flows could be adjusted with manual valves. However, the active control system required controllable valves with good time response, repeatability, and flexibility. Therefore, the fuel split was varied with a set of ten miniature solenoid valves (AM1124, Asco Scientific). These 2-way valves operate at 24 V, normally closed, for pressures up to 110 psi (76 kPa), and have an orifice size of 0.64 mm. The control signal was a 5 V signal from the control computer, which activated a set of relays to switch these valves at 24 V. The relay circuit for one vale unit is shown in Figure 22(a). The relay switch chip used was a Panasonic AQV214E, MOSFET relay chip. It can have low voltage inputs and can control switching of up to 400 V. The typical turn on time is 0.5 msec, and the typical turn off time is 0.05 msec. Ten such parallel circuits were used for each of the ten solenoid valves. So we can have ten TTL pulses, each controlling one solenoid valve. The valves were connected in parallel in a central manifold (see Figure 22(b)). Therefore, an increase in fuel flow through the pilot was attained by increasing the number of open valves, or the amount of time that the valves were open. The flow rates in the main and pilots were both affected by the operation of the valves due to pressure feedback. In order to decrease this effect, extra volume was added to the upstream manifold and in the fuel flow system such that the volume acts as capacitance for the pressure pulse.

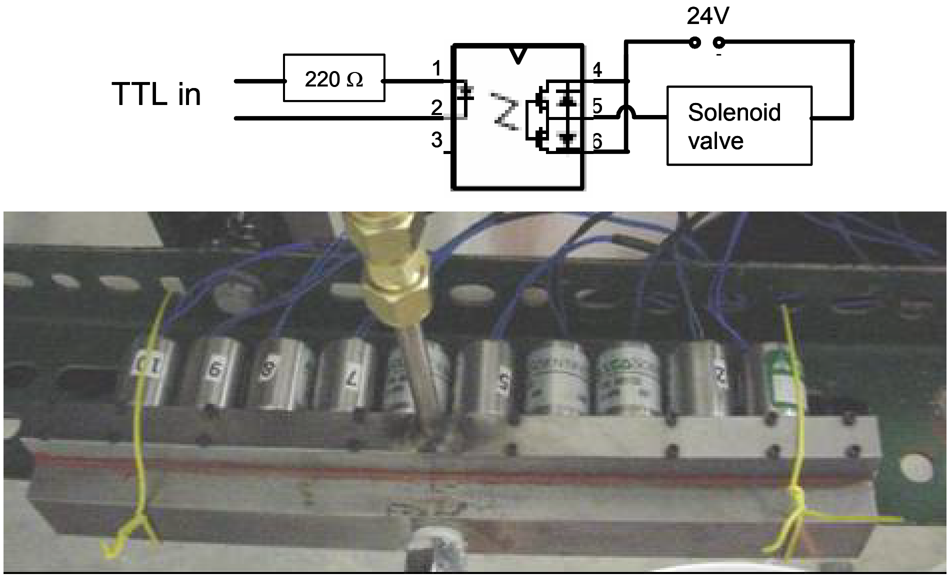

Figure 22. (a) Circuit diagram for the relay switching circuits for each vale control. (b) photograph of the valve array and manifold used for fast fuel control.

The control program used in this study was developed for the QNX real-time operating system running on a Pentium IV 1.5 GHz computer. It was used to process the optical signals and output the command signals to the valves. The real-time input and output are supplied at a sampling rate of 20 kHz by different IO boards (United Electronic Industries, Inc., PowerDAQ PD2-MF-64 for data input and PD2-AO-32 for command output).

3.4 Data recording procedure

The time series data obtained for various equivalence ratios for a given velocity was obtained by keeping the air flow rate constant and changing the fuel flow rates. For cases where the flame is very close to blowout and it blows off within a few seconds, data could not be obtained. This will cause the time series data length to be very short. To avoid this, a procedure for getting data for near blowout cases was devised. The length of a time series data set was chosen first to be 32 seconds; all data sets were 32 seconds long. The equivalence ratio for blowout was determined prior to recording the data. The criterion for blowout was that the flame is lost from the combustor within 32 seconds from the time the flow conditions were changed.

Once the lowest fuel flow rate (blowout limit) was determined, a maximum fuel flow was chosen so as to give enough points far from blowout. The data sets were now recorded in a continuous fashion. The air flow rate is fixed, and then the fuel flow rate is fixed for the highest equivalence ratio. After recording each time series data, the fuel flow rate is decreased to the next step while the flame is burning and the next data set is obtained, and so on. This process is continued until the combustor blows out. If the combustor does not blow out during the data recording, the last flow condition is repeated until that happens. The repeated process involves relighting the combustor at a lower velocity, then increasing both fuel and air flow rates such that the combustor operates at the required velocity and higher equivalence ratio. Then after a few seconds, the fuel flow rate is decreased to the blowout value. This process usually ensured that the time series data captured the blowout of the combustor. This process also allows the temperature of the walls to play a role in the blowout of the combustor. It was also observed that if the tube wall is first heated until it glows red, then the combustor does not blowout within the 32 seconds recording time, but blows out later.

Several of the large data sets taken for blowout studies were checked for repeatability. The data sets were recorded in forward and backward orders, and obtained during different days and different times of the day. The data was found to be quite repeatable, barring small variations in the blowout equivalence ratio, which may be attributable to changes in room temperature. This behavior was not analyzed in detail in this study because the focus of this work was to be able to detect the approach of blowout irrespective of the operating conditions.

During chemiluminescence imaging with simultaneous fiber data time series data recording, the recording time for the fiber data was set to 10 seconds. The recording time for the camera movies were of the order of 4-5 seconds, based on the resolution chosen and the memory size of the camera. The flow rate was set to desired values, then the fiber data recording was started, and then the camera recording was started within a few seconds so that the full movie is within the 10 second data record. When the combustor was near blowout, this process became more difficult. The combustor tube walls had to be heated for about 6 seconds, and then the procedure described above was started. Typically there were several recordings where the flame did not blowout during the recording time windows of the movie and the fiber data. This data was not stored and the whole process was attempted again until blowoff was captured. Thus, the wall temperature may not be the same across all the data sets.

For the case of droplet scatter imaging, another system must be included in the complex procedure. This scattering system includes two main components, the seeding system and the high-speed laser. The seeding system takes a few seconds to stabilize. The droplets, if they hit the quartz tube walls, are smeared along it and burn, leaving a dark black streak that blocks optical access. This does not happen when the flame is running at an equivalence ratio reasonably far from blowout. The seeding system also needed a part of the air to be routed through it. Thus the air flow was split into two parts. This meant that the flow rates had to be calculated to make sure that the net air flow rate was the desired value. Thus each run was preceded by a practice run, where the air flow rates were adjusted and the readings input into a spread sheet during the run, and the flow rates matched with good seeding density.

After that, the fuel flow rate required for blowout of the combustor was determined. Then the desired equivalence ratio step from the LBO limit was chosen, providing a required fuel flow rate. During this practice run, the flame was not present and thus the droplets hit the walls. This caused a liquid layer on the walls. Thus before each run the quartz tube was taken out and cleaned with acetone.[ii] Then the tube was reinstalled, and the remaining olive oil and black streaks formed on the tube usually burned away during the start up procedure. If this did not happen, then the black streaks were burned by increasing the equivalence ratio of the flame without any seeding.

The start up procedure began with a clean quartz tube. The air flow that did not go through the seeding system was set first. The fuel flow was set arbitrarily to have a flame in the combustor. The mixture was made richer and then the seeding air flow was increased carefully to make sure the flame did not blowout. If conditions were close to blowout, the fuel flow rate was increased further and then the seeding air was increased again to the desired value. Thus each movie recording started with the flame running at a stable equivalence ratio, the seeding system running with the required airflow rate for the desired seeding level, and the remaining airflow rate going directly to the combustor. When this was achieved, the aperture for the laser was opened to let the light sheet into the setup. The desired equivalence ratio was achieved by setting the fuel flow rate. The data acquisition computer was triggered, followed by the camera system, in a manner similar to the chemiluminescence data recording procedure. This procedure could be

---

[ii] Acetone was not very effective in removing olive oil, but was sufficient to decrease the liquid layer

continued for several equivalence ratios, in a continuous manner, if the flame did not blowout.

In the case of flame blowout, the procedure was started again, from the point of cleaning of the tube, until the settings and triggering were just right to get a good recording. For lower equivalence ratios cases, without blowout, the olive oil slowly starts flowing along the horizontal wall from the swirl vanes and reaches the quartz tube after a few data recordings. This again required cleaning the tube and restarting the procedure. Due to the removal of the quartz tube before each run, the tube location in the movies may not be consistent and the locations of the reflections are not deterministic across all the movies. This causes difficulty in the image processing procedures in terms of removing undesired light reflections.

3.5 Image processing: Chemiluminescence imaging

The chemiluminescence imaging was performed with the room lights off, and thus the background light level on the camera is almost zero. Thus there was no need for background subtraction corrections. The image of the combustor was recorded with the room lights on and a card placed in the center of view of the camera. This was done at the start and the end of the data recording session each day. This ensured the focus and the field of view did not change during the acquisition of a data set. The location of the combustor walls was determined in the post-processed images from the combustor images. The gain value of the camera remained fixed for different equivalence ratios to permit direct comparisons. Thus the images show the highest intensity value for the highest equivalence ratio (higher heat release rates). The intensity values in the images were scaled linearly to increase the contrast, and presented as inverted gray scale images for printing in the thesis. Thus dark regions in the images correspond to bright zones and the white regions correspond to zones with no chemiluminescence.

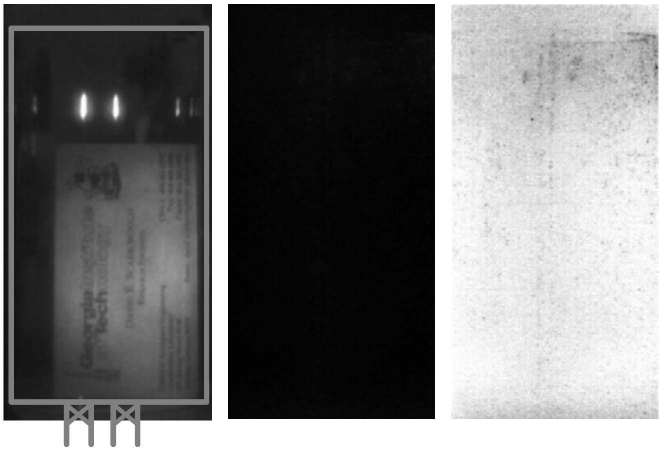

Figure 23. Image of the combustor with focusing card, raw background image of the combustor, and the processed background image.

Figure 23 shows an example focus image, which is used to find the edges of the combustor. The edges are drawn on top of the image. The second image shows the background image just after the flame blew off; as was the case for most runs, there is no significant background light. The third image is the processed image of the background image shown. This image can also be used to cross check the edges of the combustor as identified from the focus image.

Figure 24 shows two raw images from a chemiluminescence movie. The top row shows the various stages in processing of image of a stable flame. The second row shows stages in processing of image of a flame closer to blowout. The leftmost image is the raw image frame from the movie. The next image is the scaled image, which is scaled to show details of the low intensity flame near the blowout. The third column shows the inverted gray scale image with the outline of the combustor superimposed. All the chemiluminescence images were processed the same way before analysis.

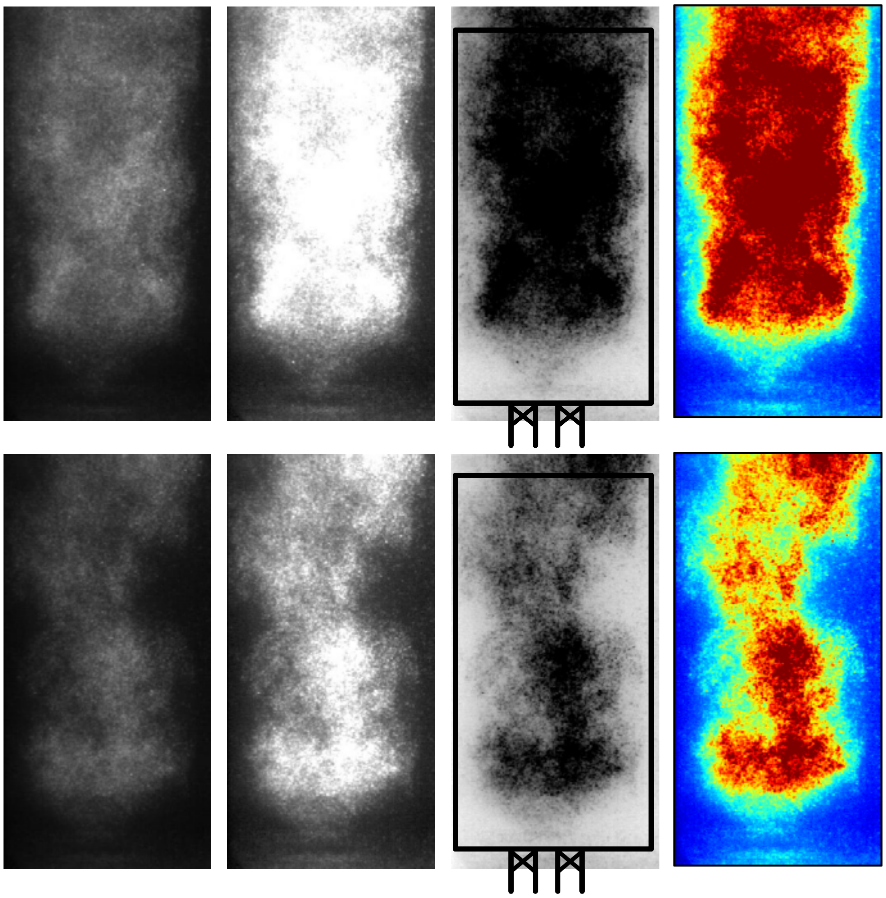

Figure 24. Stages of image processing for chemiluminescence movie images. First and second rows show regular flame and partial flame respectively. First column: raw movie frame, second column, scaled image, third column: inverted gray scale image and fourth the false color image.

The scaling of the images is achieved by using a linear function to convert the raw image intensities into scaled image intensity values. The scaling used for chemiluminescence images is given by:

$$B = \begin{cases} 0 \quad if A \leq 2 \\ (A+2)\dfrac{255}{90} \quad if\, 4 < 2A < 185 \\ 255 \quad if\, 2A \geq 185 \end{cases}$$

The formula shown above is used for each pixel in the image to convert the raw image array (A) into the scaled image (B). Figure 25 shows the distribution of intensities in the images before and after scaling. It can be noted that the intensities are stretched towards value 255. In case of the stable flame, a many intensity values are forced to become 255. But when close to blowout, the flame intensity distribution is just stretched such that only the highest intensities are set to become 255, giving better presentation of the images for analysis.

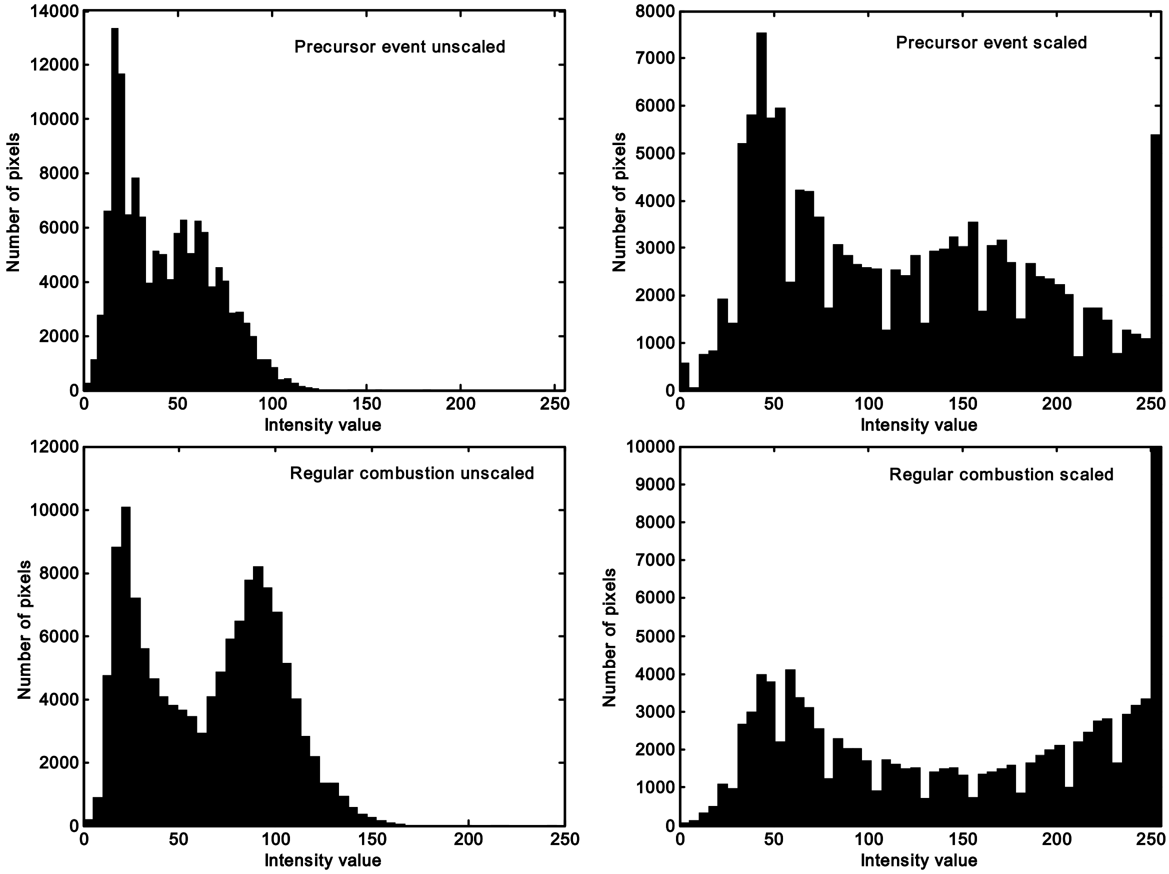

Figure 25. Change in distribution of chemiluminescence intensities in an image due to scaling used. The left column gives statistics for the unscaled image while the right gives for scaled image. The first row gives a case which is of interest in this thesis, while the second row gives a case where the flame is stable. Note the saturation in the scale in the stable flame case.

3.6 Image processing: Droplet scatter imaging

Processing of the droplet scatter images were more complex even though the experiments were performed with the room lights off, as the quartz tube surface scatters and reflects the high intensity laser light. Moreover, the intensity of the laser varied shot-to-shot and thus consecutive images will not have the same intensity. In addition, the quartz tube was moved between each run and thus the laser sheet may not pass through the tube on the exact same spot and thus the reflections may move by a few pixels each run. Also when there is olive oil liquid layer flowing along the tube, the light is refracted and scattered by the liquid layer and thus the laser sheet did not have uniform intensity along the height. The camera gains were selected such that the reflections do not saturate the pixels in the camera and were fixed for all the equivalence ratios. As a consequence, the droplet scatter intensities, which are weaker than the laser reflections, had about half the full scale value of the camera (128 counts).

The image processing procedure started with subtraction of laser reflections. The combustor was recorded without any flow with the laser light on. This gives the basic pattern of the reflections in the combustor. This reflections-movie was recorded only once each day of experiments. This is considered only the nominal location of the reflections as the tube moved every time when it needed cleaning. Since the laser intensity varied during each run, an average background value cannot be used to subtract from all the images. Thus the reflections-movie was used to produce several average images with specific laser intensity ranges. The shot-to-shot laser intensity was not recorded and was determined by the variation of intensity of reflections in the image. A region far from the expected droplet zones is picked for this purpose (see Figure 26). This small rectangular region was used to give an average intensity value for each frame. The variation of this value in time gives the variation of the laser intensity from frame to frame (see Figure 27).

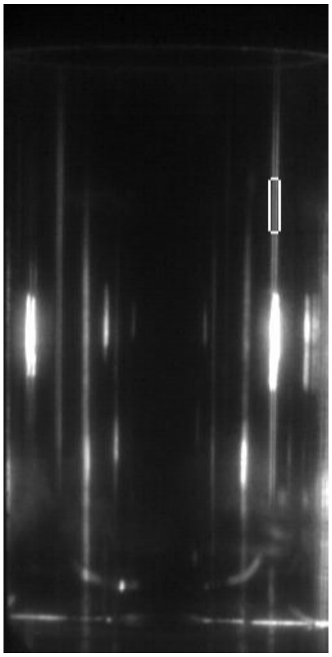

Figure 26. Image of the combustor with the laser sheet illumination, with no droplet seeding. The various lines seen in the image are due to reflection of the laser sheet inside the circular tube. The white rectangle above the bright spot on the right side is the reference window for laser intensity calculations.

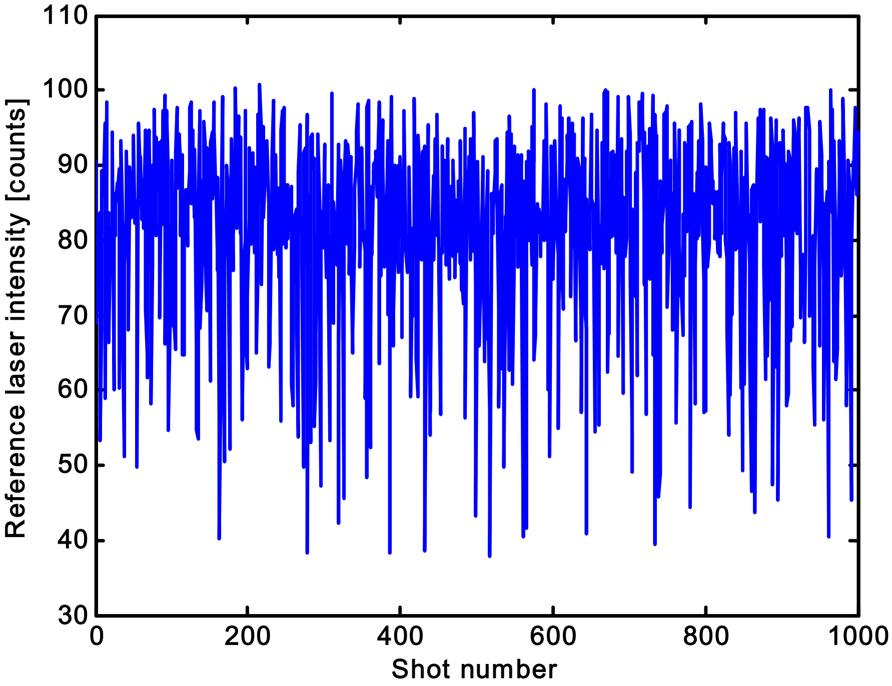

Figure 27. Shot-to-shot variation of the laser intensity value caluculated from the rectangular reference window.

The range of laser intensities determined by the rectangular region, was divided into 15 bins. Figure 28 shows the bins and the number of reflections-movie frames that fall under each bin. Each of the reflections-movie frames was segregated into these bins and used to give one average reflections-image for each bin. Figure 29 shows two example reflections images for two laser intensity bin values of 50 and 100. Each of the droplet movie frames from each run was used to find the rough laser intensity from the same rectangular window. The laser intensity as calculated from the droplet movie images also varied from 40 to 105 counts and this range divided into 15 bins resulted in 5 intensity values in each bin. This laser intensity value was used to pick the appropriate reflections-image to subtract from the droplet image.

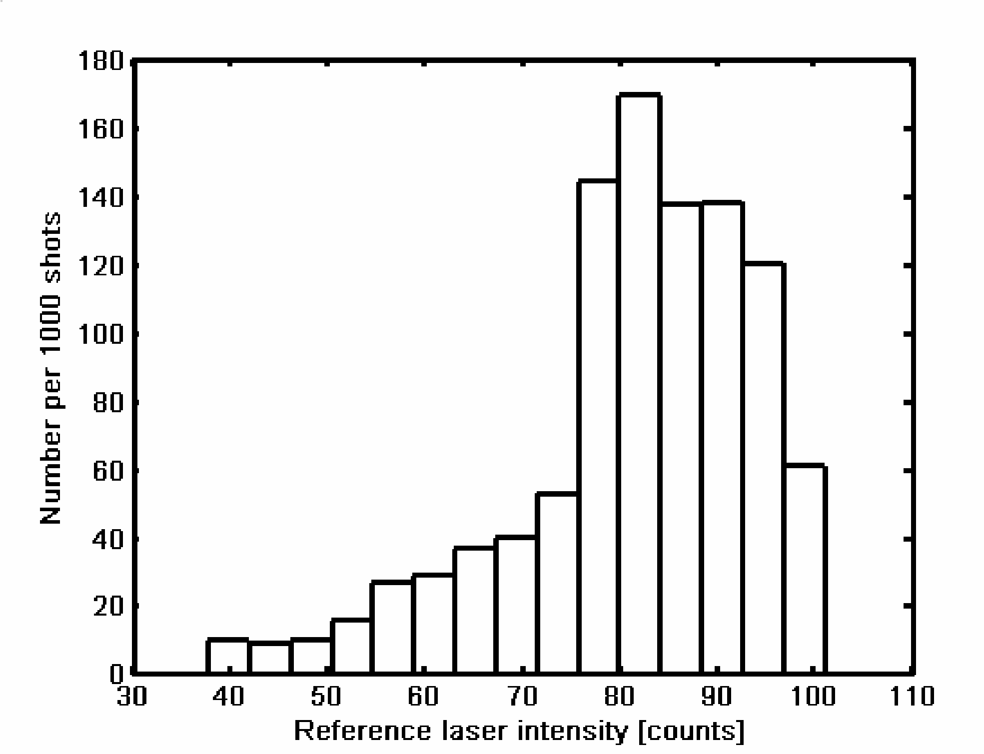

Figure 28. Shot-to-shot variation of the laser intensity. This plot represents the bins used and the number of shots of the laser with the given average intensity in the reference window.

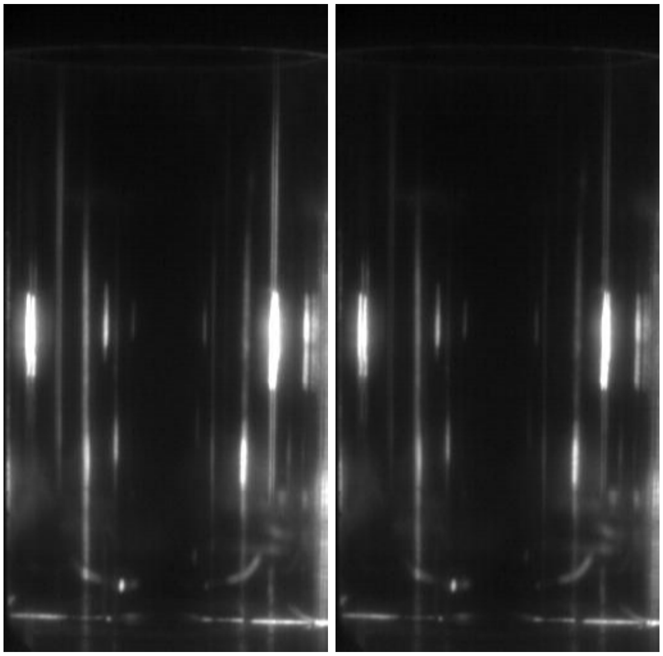

Figure 29. Sample images of reflections images used to correct the laser reflections. The images shown are from averaging the images in the bins corresponding to intensity values of 100 and 50 counts respectively.

This procedure removed most strong reflections but left out the reflections that moved due to movement of the tube during cleaning of the tube. The accuracy of this method in removing all the reflections will be higher for higher number of bins. However, having all the values for the laser intensity increases the number of reflections images to be stored and increases the general noise level due to fewer the number of such images in each bin.

The reflection-subtracted images were then corrected for the laser intensity variation. The scattered light intensity, which is proportional to the intensity of the incident light, also fluctuated image-to-image. This was corrected by dividing the whole image by a single number such that the intensity value (from the reference rectangular region as before) is kept constant at 100 counts. After this correction, the images primarily had only the droplet scatter intensities. The intensity corrected images were scaled to fit the full colormap to increase the sensitivity. However, the whole movie was scaled in a similar fashion as the chemiluminescence images. For easy visualization in print the frames are presented in inverted gray scale colormap. Figure 30 shows the stages of processing of the raw image from the droplet scatter movies for an image far away from blowout and for an image closer to blowout.

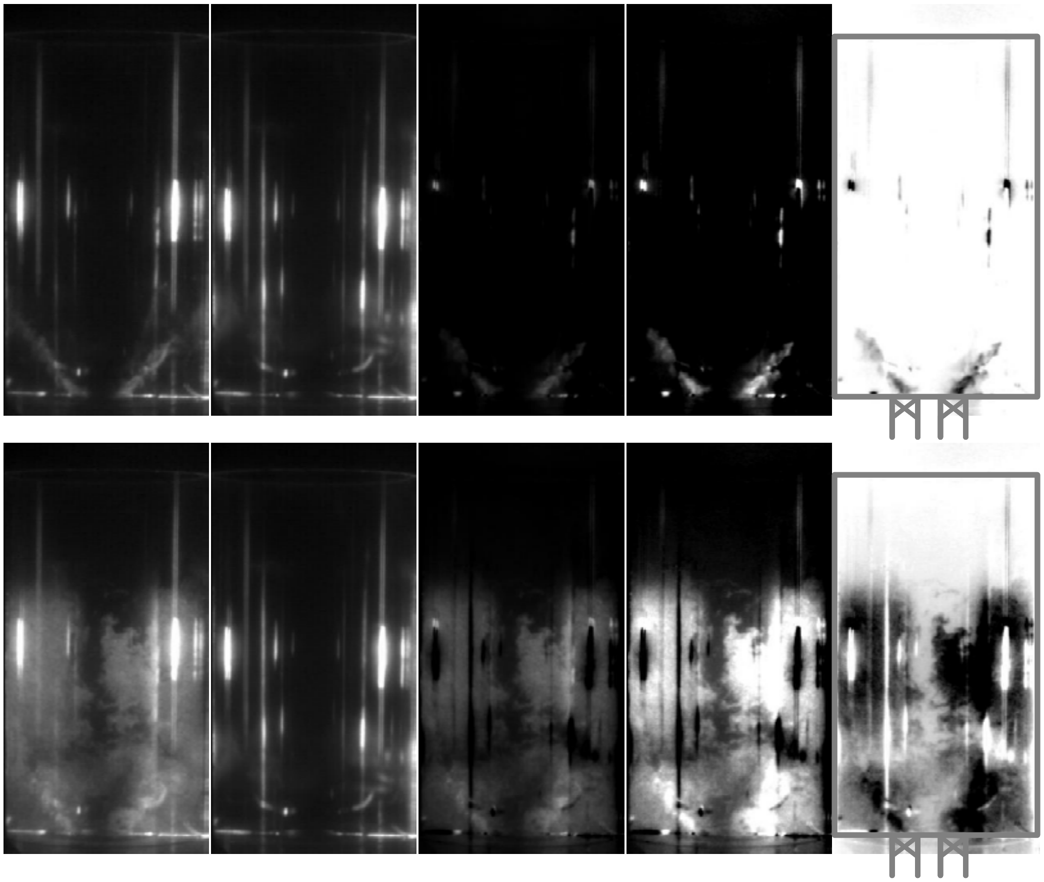

Figure 30. Stages of image processing for droplet scatter movie images. First row: stable flame, second row: flame very close to blowout. The columns from left to right represent, the raw movie frame, the reflections image chosen to be subtracted from that frame, the reflection and intensity corrected image, the image after scaling, and finally the image after gray scale inversion.

Figure 30 shows the raw image in the first column. The reflections image chosen for subtraction based on the calculated laser intensity is shown in the second column. The third column shows the image after the laser reflections and intensity variations are corrected. The next image shows the intensity scaled image. The final image in the row shows the inverted gray scale image which is the final processed image for that frame of the movie. The outline of the combustor is also super imposed over the final image for ease of visualization of the images.

The intensity scaling for the droplet scatter movies is given by:

$$B = \begin{cases} 0 \quad if A \leq 1 \\ (A-1)\dfrac{255}{98} \quad if 1 < A < 100 \\ 255 \quad if A \geq 100 \end{cases}$$

This scaling function was arrived at manually after several iterations for best representation of the images for the given analysis. In this scaling, the intensities are not as strongly shifted past the 255 value since the movies have high intensity values mainly only near blowout. This scaling function was fixed for all the images presented in the dissertation.

Chapter 4

Sensing of LBO

This chapter describes the development of a sensing strategy for estimating the proximity to lean blowout (LBO) during the operation of a combustor. The approach to LBO proximity sensing is based on unsteadiness that has been observed prior to the blowout of a combustor. Since an ideal sensor for LBO proximity detection should be sensitive, reliable and survive the harsh environment in a gas turbine combustor, a nonintrusive approach is preferable. Here optical emissions, i.e., chemiluminescence, from the flame are used to monitor the variations in the reaction rates inside the combustor. This choice also allows the optical sensor to be located outside the high pressure, high temperature combustor. The systematic observations of the unsteady behavior near blowout are presented in Section 4.1. Section 4.2 identifies the extinction reignition events observed. Section 4.3 describes the sensing methodologies to estimate the proximity to the LBO limit in the swirl dump combustor. Section 4.4 presents various aspects of the sensor development towards implementation in practical combustors. The final section summarizes the results from this chapter.

4.1 Near LBO Characteristics of the Combustor

As illustrated in Chapter 1, there have been a number of studies that reported increased unsteadiness just prior to blowout of a combustor. This section describes systematic observations and characterization of the unsteady behavior prior to blowout in the swirl-dump stabilized combustor. This combustor, used for most of the studies in this dissertation, is described in Chapter 3. The combustor was operated near blowout conditions for long times, and the temporal behavior of the combustor was recorded. The variation in combustor operation as LBO approached was studied by holding the overall airflow rate constant and decreasing the fuel flow rate. This ensured that the incoming velocity field was approximately constant while the equivalence ratio was reduced, since the flow rate of the fuel was small compared to that of the air. Chemiluminescence emission from the OH radical in the combustion zone was recorded over a period of time for various equivalence ratios near blowout.

4.1.1 Fourier spectral analysis

Figure 31 shows the Fourier power spectrum of the optical signals (lens based collection) for equivalence ratios of 0.81, 0.751, and 0.748. LBO occurred at an equivalence ratio of 0.745 in this set of experiments. These curves have been normalized at each equivalence ratio to have the same total power (this accounts for the overall increase in chemiluminescence associated with higher heat release at higher ϕ). The fractional energy in frequencies below 200 Hz appears to increase while that of frequencies above 400 Hz appears to decrease. However there are no peaks arising in the low frequency range as LBO limit is approached. This indicates that there are no coherent, periodic oscillations occurring near the blowout limit. Nevertheless, it is clear that close to the LBO limit, the “low frequency” spectrum has the largest (relative) increase in energy.

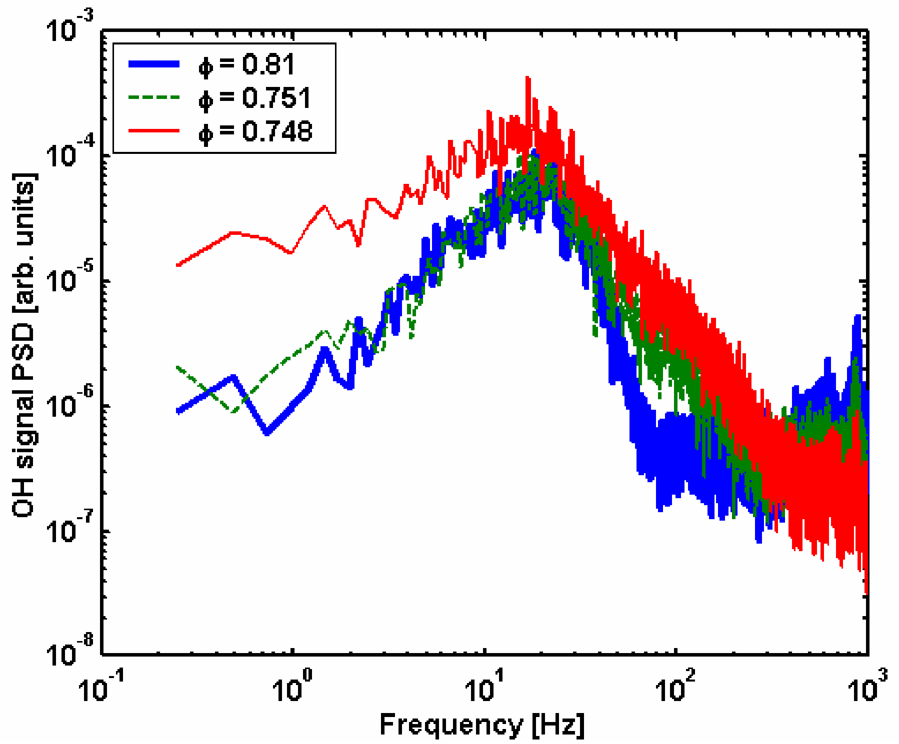

Figure 31. Fourier power spectrum of optical emission signal for ϕ = 0.81, 0.751 and 0.748. ϕ_{LBO} = 0.745, Tube diameter 70 mm. Lens based collection of light.

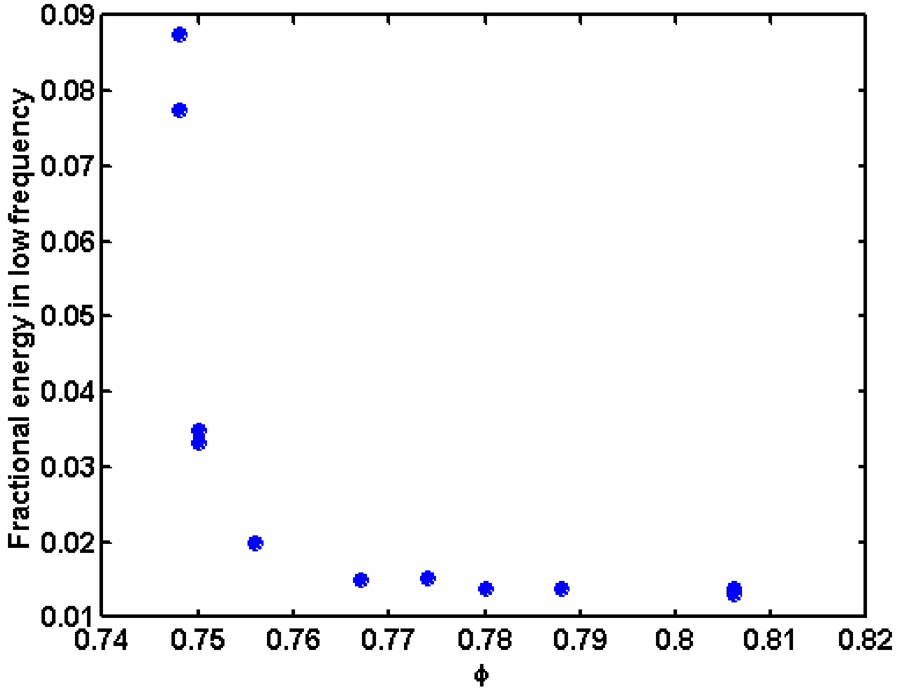

Figure 32. Variation of fractional energy in the low frequencies (10-200 Hz) for various equivalence ratios.

Figure 32 shows the fraction of the total fluctuating energy (i.e., excluding DC) that is contained in the low frequencies (in the range 10-200 Hz). It can be noted that the fraction of low frequency content increases rapidly as LBO is approached. Thus the proximity to LBO can be estimated by quantifying the relative amount of low frequency content in the signal. A practical implementation of this approach might employ two filters: a bandpass filter to measure the low frequency content and a highpass filter to remove the DC signal (leaving the total fluctuating power). Monitoring the lower frequency content will however, require longer times, which will hamper the time response of the control systems. Thus this study investigated more methods for detecting the approach of blowout.

4.1.2 Time domain analysis: statistical methods

As an alternative to frequency domain analysis, one can also directly analyze the time series data from the sensor to observe its dynamic behavior. Figure 33 shows examples of the sensor outputs at two stable equivalence ratios and one near the LBO limit. These data sets are the same as that used in frequency analysis. The LBO equivalence ratio for this combustor was just below 0.745 for the flow conditions used. It can be noted that the turbulent nature of the combustion produces variations in the chemiluminescence emissions even when the combustor is considered stable. As expected, the mean emission signal decreases at leaner mixtures due to the reduced heat release (reaction) rates as the fuel flow is reduced. The results also show the presence of relatively high amplitude short bursts, with the signal going both below and well above the mean value. The number of these bursts appears to increase near LBO.

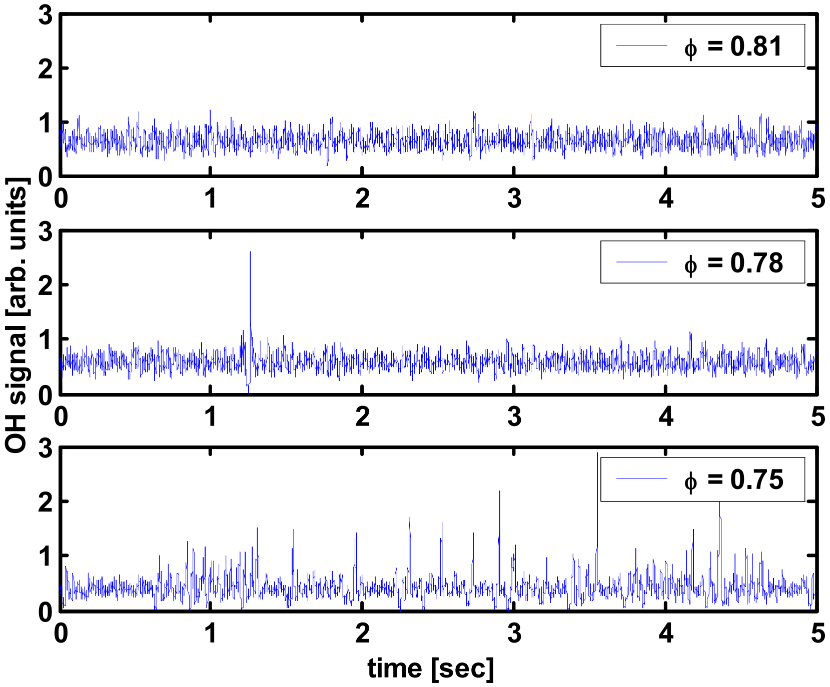

Figure 33. Time series data of OH chemiluminescence signal for ϕ = 0.81, 0.78 and 0.75. ϕ_{LBO} = 0.745, Tube diameter 70 mm, average cold axial velocity 6.1 m/s. Lens based light collection.

As the change in the signal behavior is clearly evident to the human observer as LBO is approached, a time-series analysis is clearly attractive as an indicator of onset to blowout. The challenge is to determine an analysis procedure that identifies the presence of these bursts as readily as the human observer. A simple approach would be to calculate the statistical moments, e.g., standard deviation (std) or root-mean-square deviation (rms) of the signal, higher order moments, kurtosis. The statistical definitions are given below.

$$Mean = \mu = \sum x / n \qquad Std = \sigma = \sqrt{\mu_2}$$

$$Second\_moment = \mu_2 = \frac{\sum (x-\mu)^2}{n} \qquad Kurtosis = k = {}^{\mu_4}\!/_{\mu_2^2}$$

$$Fourth\_moment = \mu_4 = \frac{\sum (x-\mu)^4}{n}$$

The second and fourth moments are summations of the higher powers of deviation from the mean. Thus they emphasize the large deviations form the mean. Statisticians often use kurtosis, which is the fourth moment normalized by the second moment, to show significance of the outliers in a distribution.

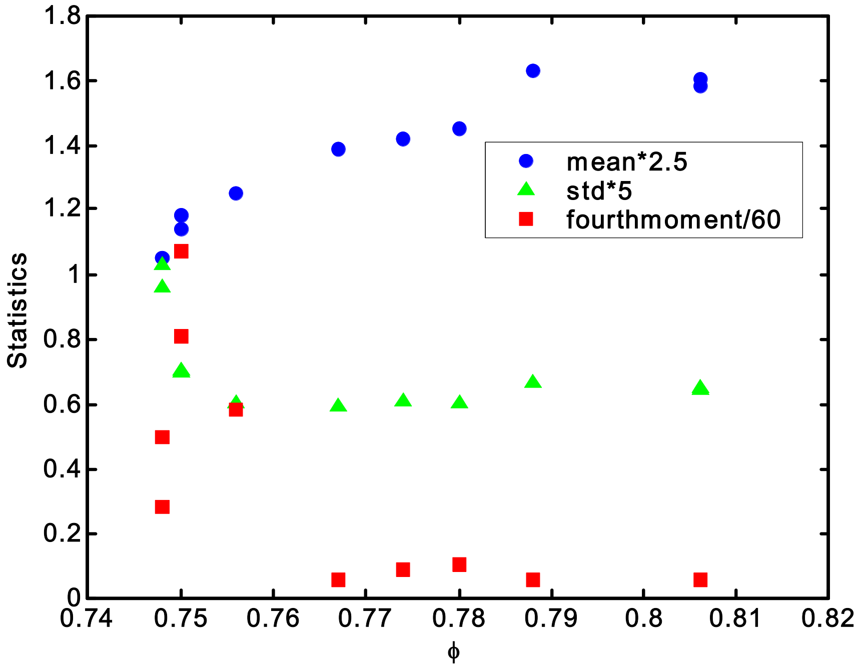

Figure 34. Variation of the mean, standard deviation and fourth moment as a function of equivalence ratio.

Figure 34 shows the variation of the signal's mean, standard deviation (second moment) and fourth moment with equivalence ratio. The mean of the signal decreases for lower equivalence ratios corresponding to the reduced fuel flow rate (reduced heat release rate) and due to inefficient combustion as LBO is approached. The higher order moments have higher values as the LBO limit (equivalence ratio of 0.745) is approached. Thus these parameters can also be used to indicate the approach of blowout of the combustor. The normalized statistical quantities such as std/mean and kurtosis can also be used for this purpose. Figure 35 shows the variation of these parameters as a function of equivalence ratio. Thus these parameters can also be used as indicators of approach of the imminent blowout.

There are other statistical approaches besides discrete moments that could be used to analyze the detector output, for example calculation of a probability distribution function. Such an approach would be computationally expensive and would probably not provide added useful information compared to what is found from a few simple moments. Thus this idea is not pursued in this dissertation.

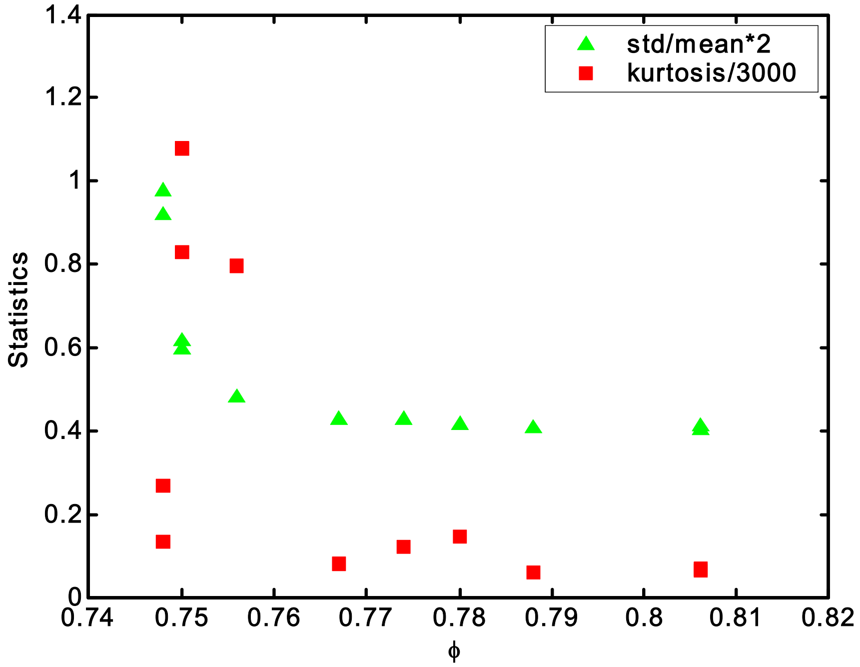

Figure 35. Variation of normalized statistical quantities with equivalence ratio.

All the data presented so far (spectral energy fraction and statistical moments) were based on data sets with records 33 seconds long, recorded at 2 kHz, at each flow condition. The analysis procedures then reduced this to a single "averaged" measure for each data record. For a controller to detect the approach of the LBO in real-time, however, it is desirable to detect the change in behavior of the signal within a fraction of a second. The statistical methods can be modified to accomplish this with the use of a short duration moving window, for example by calculating the kurtosis in a moving time window. This type of local statistical measure (calculated in a 16 msec window) of the signal variation is shown in Figure 36. The time trace shown corresponds to the time series data shown in Figure 33. It can be noted that the kurtosis signal increases in value when the signal has bursts in them. Also the value reached by kurtosis also is higher for lower equivalence ratios. This suggests that the deviations from the local mean value are higher as blowout limit is approached.

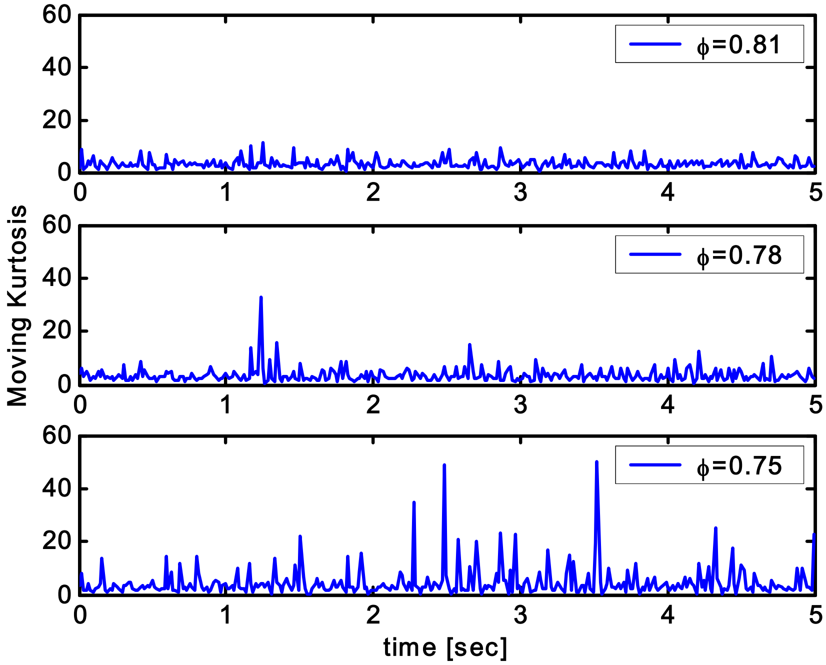

Figure 36. Variation of kurtosis over 16 msec window as a function of time for three different equivalence ratios.

It is evident that the approach of detecting blowout of the combustor by monitoring kurtosis of the time signal over a moving time window can also be used to detect blowout of the combustor. The accuracy of this statistical method depends on the number of samples and thus the time window and the sampling frequency. Longer time window can give accurate kurtosis values but will need longer data acquisition time. A threshold can be set on the kurtosis time signal to establish a criterion for the control system to take preventive action.

4.1.3 Time domain analysis: direct signal analysis

The preceding statistical method was based on the fact that there are significant deviations from the mean in the time trace of the signal. Kurtosis was used to amplify these deviations and a threshold was used to set actuation criterion. However as a statistical approach, it provides only some "averaged" measure of these deviations over the integration time. In this section, the time-localized nature of these excursions of the raw signal is examined in more detail.

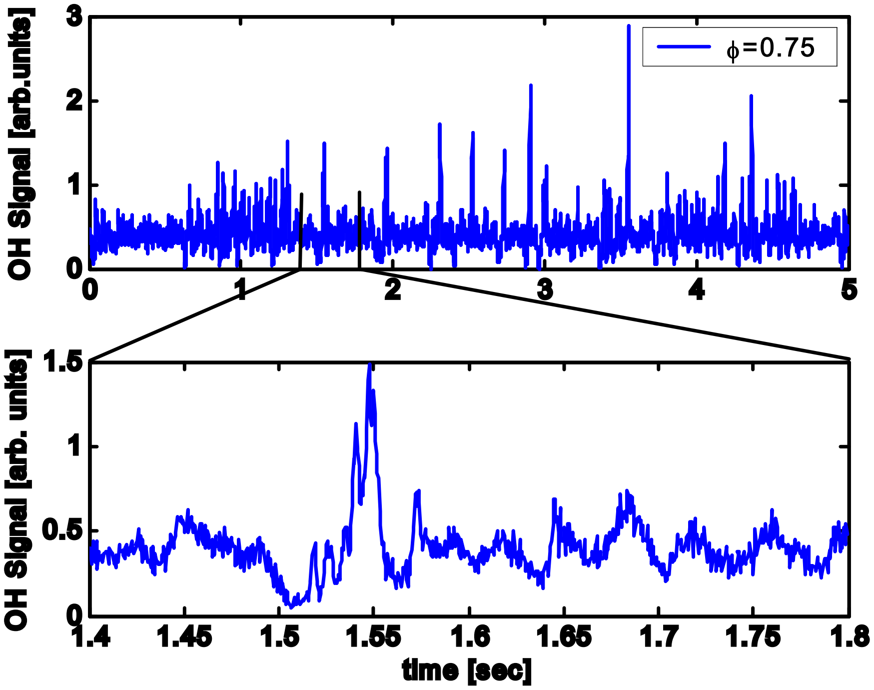

Figure 37. OH chemiluminescence time series data near blowout, shown with expanded view of an extinction-reignition event.

Figure 37 shows the OH chemiluminescence signal as a function of time, with an expanded plot of just one occurrence of deviation from mean. This data shown is the same as the data shown for equivalence ratio of 0.75 in subsection 4.1.2. It can be seen that these bursts (or unsteady ***events***) are characterized by an almost complete loss of chemiluminescence signal quickly followed by a strong signal spike. This corresponds to a local extinction of the flame followed by a strong reignition of the flame. This dissertation concerns the behavior of these unsteady events and these local extinction-reignition events from this point forward will be termed '***precursor events***' to blowout.

These distinctive extinction and reignition events span a period of several milliseconds, and they occur, without any obvious periodicity, prior to LBO. As the LBO limit is approached, more of these events occur in a given time period and thus the time between two such events decreases closer to LBO. The data presented later will show that the above mentioned near-LBO "events" occur in a number of combustor configurations, e.g., combustor diameter, length of the combustor, and flow rate. These temporary extinction-reignition events can thus be considered as ***precursors*** to the imminent total flame loss in the combustor.

Figure 38 shows the time series data of a precursor event each at two different equivalence ratios. The overall mean of the signal is lower for the leaner case due to lower reaction rates. The general behavior of the signals away from the precursor events appears similar for the two cases. There are small fluctuations around the mean in the signal due to turbulent nature of the flame. During the precursor event, the signal appears to decrease to a value very close to zero (representing complete loss of flame), followed by a sharp increase in the signal (representing presence of intense combustion), and finally by the signal drops back to the mean. The reignition phase of the leaner precursor appears to have perturbations while the richer case does not have significant perturbations.

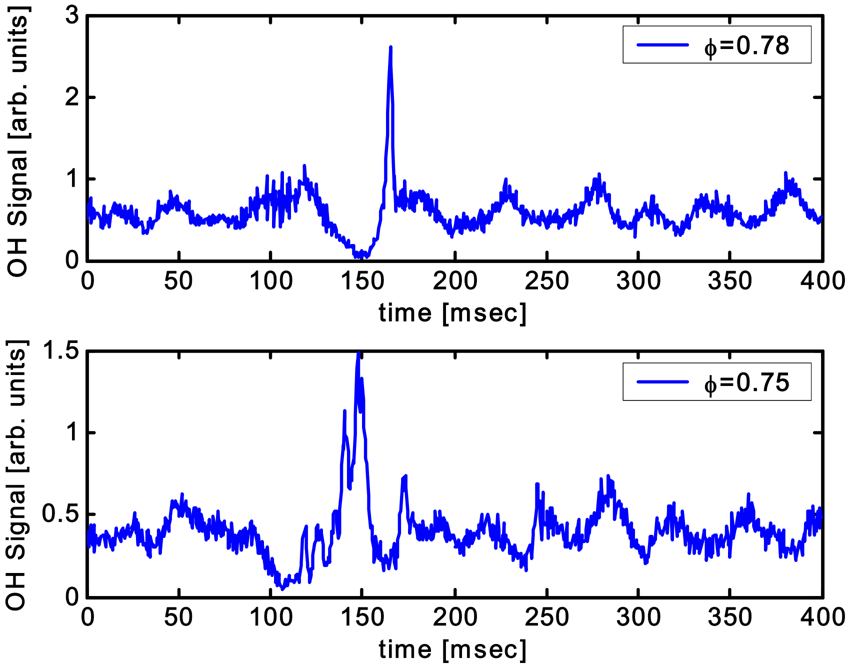

Figure 38. Expanded time series data of OH Signal of precursor events at two equivalence ratios. Note the change in the scale between the two plots.

Moreover, Figure 37 shows that the magnitudes of the extinction and reignition spikes are not repeatable for several events at the same operating conditions. However, investigation of several precursor event time series data revealed that the qualitative behaviors of all the precursors are similar across several flow conditions. Thus these precursor events are considered as one entity over several flow conditions and are not categorized based on the strength of their deviations from the mean.

The sensor developed in this study detects these precursor events and uses their characteristics to infer the proximity to blowout limit. The data reduction and sensing methodology developed is described in detail in section 4.3.

4.2 Precursor events

Before developing sensing strategies based on these precursor events, the precursor events were investigated more closely with high speed visualization of chemi-luminescence from the flame. Figure 39 presents gray scale images (with intensity based coloring) from a movie recorded very close to blowout of the combustor. The cold average axial velocity was 3.9 m/s, the equivalence ratio was 0.39. The movie was recorded at 1930 Hz with exposure time of 180 µsec. The top row shows the images of the flame during regular combustion. The bottom row shows the flame during a precursor event. Note that the time gap between the images is different for the two rows. The top row sequence occurred 135 msec after the bottom row in the movie. The outline of the combustor is superimposed on the first image in each row. The rectangle superimposed on the first image in the bottom row represents the collection volume of the lens based collection system used for the signals presented above. The images were obtained without spectral filtering and represent line of sight integrated visible light emission from the flame.

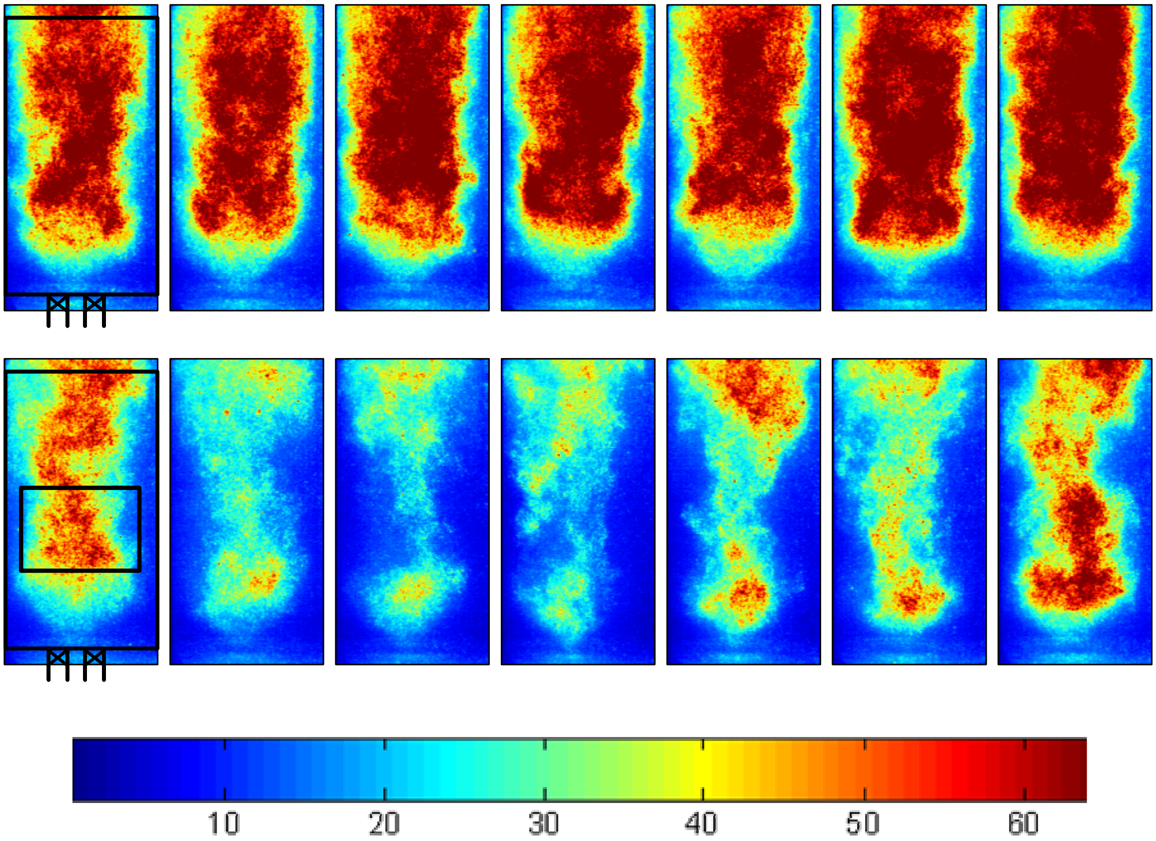

Figure 39. Images of flame chemiluminescence emission for ϕ = 0.73, average cold axial velocity of 3.9 m/s. Top row: flame during regular combustion, images separated by 2 msec. Bottom row: flame during a precursor event, images separated by 4 msec. The top row time sequence occurred 135 msec after the bottom row time sequence, during the same movie. Red regions represent flame emission and blue regions represent no flame emission.

The flame appears to be having a V-shape near the inlet of the combustor and fills the whole combustor above a certain height. The top row images show that the flame emission is roughly occupying the same volume for all the images. However, the local flame zone intensities change from image to image.

The images in bottom row show that there is a large scale flame loss compared to the top row, during the precursor event. The images before and after the sequence shown in the bottom row, appear very similar to the images in the top row and thus were excluded. The flame intensity decreases and then increases during the precursor event. The flame in the mid-height of the combustor appears to be pinched from the sides, and the overall flame appears to almost split into two parts. This is followed by the flame becoming stronger again and filling the whole combustor. This suggests that the unburned fuel that entered the combustor during the extinction phase is rapidly consumed. Afterwards, the regular combustion as shown in top row continues.

This temporary flame loss behavior was also inferred by Hedman *et al*.[74] However, that study used the PLIF technique with slow repetition rate Nd:YAG laser and was not able to get a full sequence of images of the flame dynamics. During the same time period as this dissertation work, another study was published that describes a similar extinction-reignition behavior prior to complete flame loss.[21]

The location of the lens collection volume and the movie image sequence together justify the temporal behavior of the signals observed during the precursor event. Precursor events are now defined to be the extinction-reignition events that occur at random times during combustion. These events are observed near the blowout limit and they increase in number near the limit.

4.3 Sensing Methodology

The precursor events correspond to short duration extinction-reignition events occurring at random times in the combustor prior to LBO. The number of such LBO precursor events in a given time period increases as LBO limit is approached. Therefore, a sensing technique that uses these precursors and their properties can be used to estimate the proximity of the combustor to LBO.

The first step in estimating the proximity to LBO limit is to find a reliable and effective method for identifying these precursors in a time series signal. Since the characteristic of the precursors is a sudden large drop in emission followed by a return to high signal, signal thresholding seems well suited to the task.

The optical signal has a nonzero mean value, and the precursor events produce excursions above and below the mean. Therefore, the threshold criterion could be either an upper threshold or a lower threshold. From a control application point of view, it would be better to use the lower threshold since the flame extinction occurs before the re-ignition. Thus this gives the controller the earliest warning possible, which is desirable.

It should be noted that the sensitivity of this method can vary based on the choice of the threshold criterion. Also as shown above, the mean chemiluminescence signal changes with the combustor power (fuel flow). Therefore the chosen threshold should be weighted by the mean signal value to account for the power changes. Thus the thresholds were chosen to be a fraction of the mean signal value at the given operating condition. The initial results presented below correspond to a threshold of one-quarter of the mean signal for the OH emission sensor, but the trends reported here, are not a strong function of the threshold.

Figure 40 presents the variation of number of events as a function of equivalence ratio, as identified form the time series signal using threshold of ¼ of the local mean signal. The vertical line represents the blowout limit for the conditions used in this data set. The number of events/sec increases as the LBO limit is approached. Thus this parameter can be used to estimate the proximity to the LBO limit. This is one of the parameters used in this study to assess the proximity to the LBO limit.

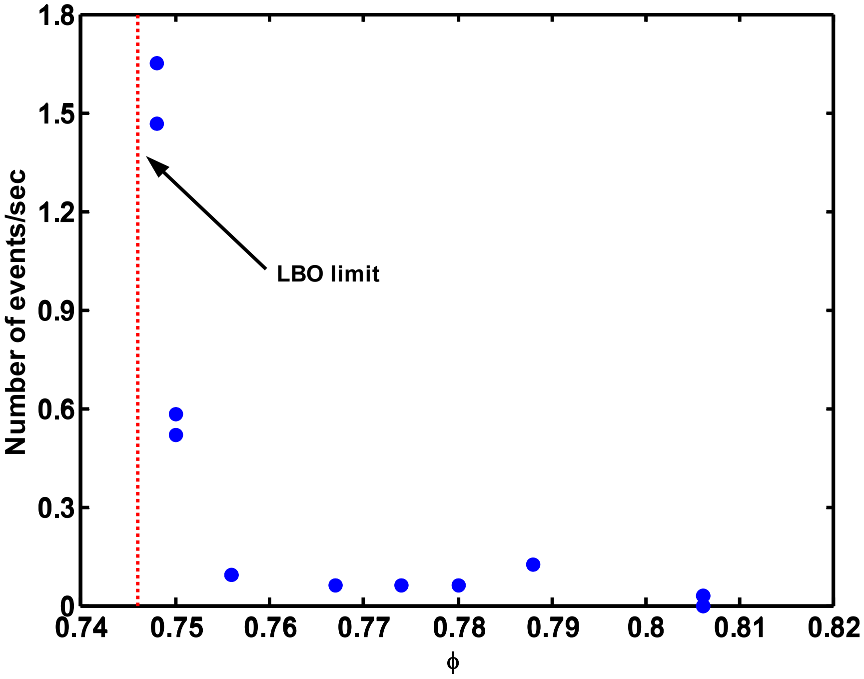

Figure 40. Number of precursor events/sec averaged over 33 seconds, as a function of equivalence ratio.

Since the approach is not based on an *absolute* signal level, it should be robust in the presence of engine/sensor aging, for example, particle or film deposition on an optical port or optical fiber. The specific choice of threshold value for detection will vary depending on the combustor, the optical collection location, and the desired sensitivity and noise rejection of the technique. An example of noise effects is seen in Figure 41. The 30% mean threshold is crossed two times by the signal during the second precursor event shown. However, it can be seen that there is essentially only a total of two events that must be detected from this signal. This multiple counting of events occurs due to the noise in the signal that causes the signal to briefly rise above the event threshold and then fall below again. This can cause errors in estimation of the proximity to blowout.

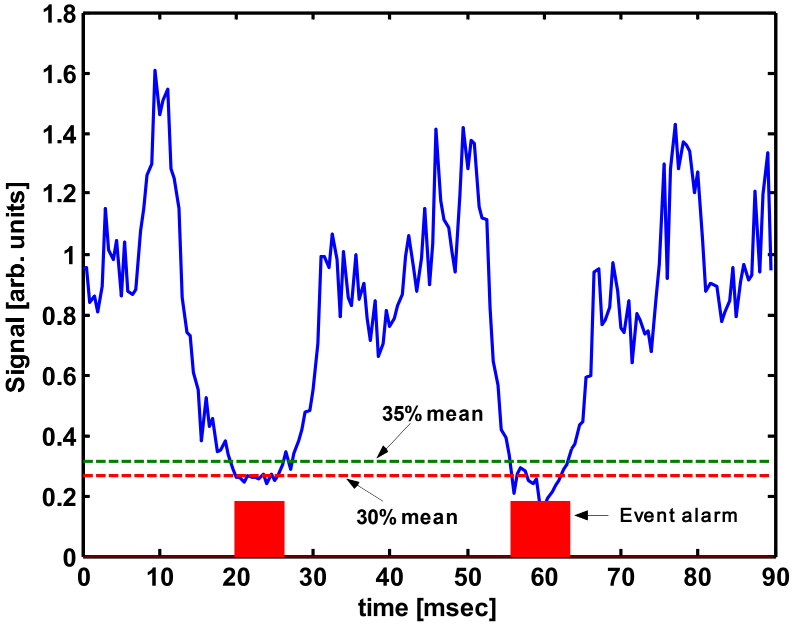

Figure 41. Noise rejection approach based on double thresholding used to detect the LBO precursor events. An event starts when the lower threshold is crossed and ends only when the upper threshold is crossed.

To reduce the number of false alarms due to noise in the signal, a double thresholding approach is useful (see Figure 41). An event "starts" when the signal drops below a lower threshold, and ends only when the signal goes above the higher threshold. The figure shows the alarm event variable which is non-zero when an event is identified. The first precursor event in Figure 41 ends when the signal goes above the upper threshold. Perturbation in the signal causes the signal to go below the upper threshold only. This does not cause multiple counting of the event. In a similar manner the perturbation in the second event does not cause double counting of the event.

It is evident that if the perturbation is high enough, the events shown can still be double counted. The gap between the two thresholds must be varied based on the noise level expected in the signal, in order to accurately estimate the proximity to blowout limit.

The duration of a precursor event, defined as the time gap between the start and the end of the event, is another characteristic of the precursor event. This can be visualized as the width of the event alarm as shown in Figure 41. Figure 42 gives the variation of the average number of events per second (averaged over 33 seconds) and the total duration of the events/second as a function of equivalence ratio. Both parameters increase rapidly as the LBO limit is approached. Thus either could be used as an LBO proximity measure. It is also possible that a combination of the two parameters could be incorporated into a control algorithm for more robustness. It can also be noted that the two curves scale identically till very close to LBO limit and then the duration curve increases faster. This suggests that the duration of the events on an average does not change till close to blowout but becomes longer close to blowout.

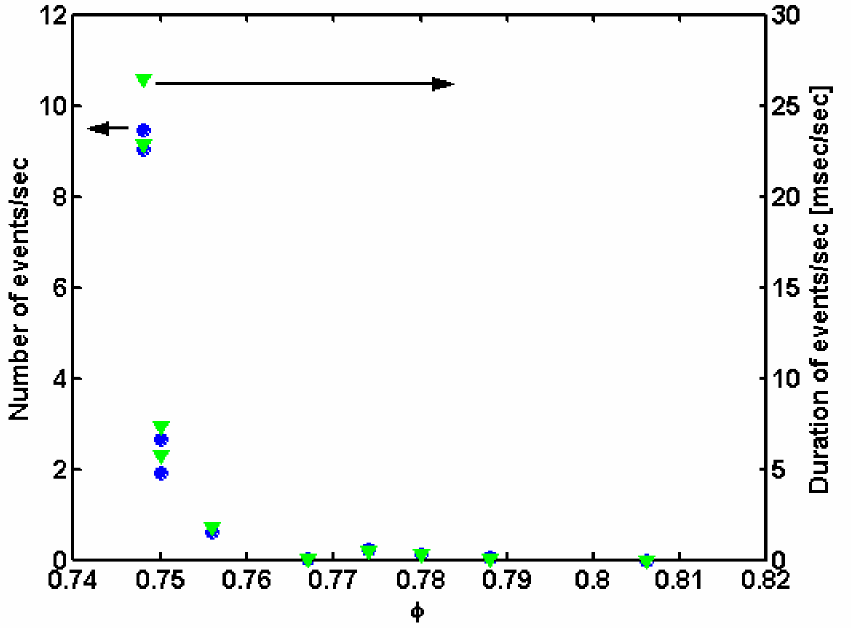

Figure 42. Proximity parameters from OH chemiluminescence signal (lens system). Number of precursor events/sec and the total precursor duration/sec (msec/sec), averaged over a period of 33 seconds.

As noted previously, the precursor detection should have a better time response (than is achieved by averaging over 33 seconds) in order for a control system to respond quickly to an approaching LBO condition. This is readily achieved by modifying the thresholding and event counting approach to compute the number of events/second in a short window of time (say, the one second).

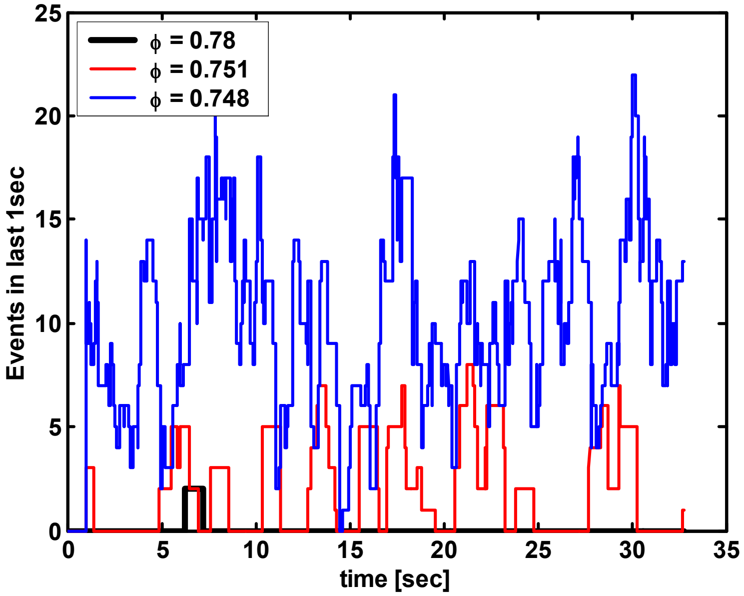

Figure 43. Variation of number of precursors in a moving 1 second time window, with time for ϕ= 0.78, 0.751 and 0.748.

Figure 43 shows the variation of number of events in a moving one second window, over a 33 second record for equivalence ratios of 0.78, 0.751 and 0.748. This data set is the same as those used in the results shown till this point. The blowout equivalence ratio for the conditions was 0.745. It can be noted that the events are not uniformly distributed in time. They seem to appear in groups as the blowout limit is approached. The rise in number of events is clear as LBO is approached. This temporal variation of number of events can be a control input signal that triggers preventive action from the controller when it crosses a threshold.

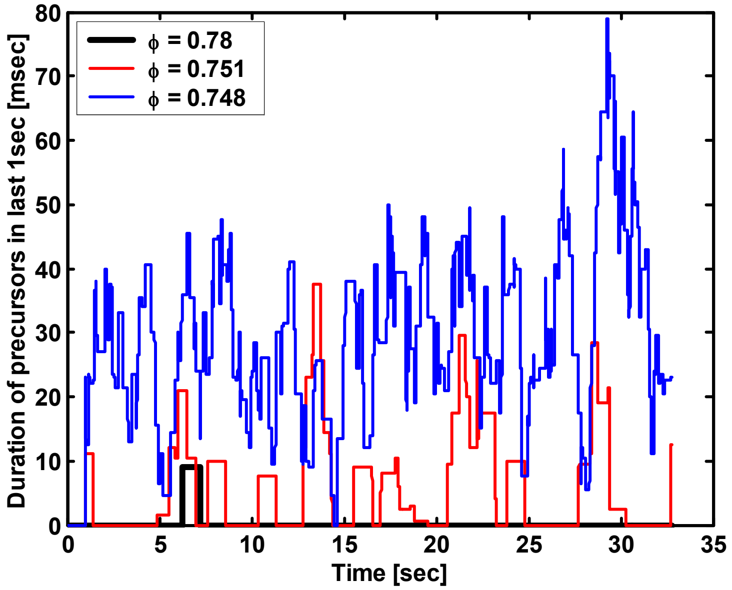

Figure 44. Variation of duration of precursors (in msec) in a moving 1 second window, with time for ϕ= 0.78, 0.751 and 0.748. ϕ_{LBO}= 0.745.

It was noted earlier that the duration of an extinction event also tended to increase as LBO is approached. A controller could also use the event duration, i.e., the time that the signal stays past (or under) the threshold value. Figure 44 shows the total duration of the events in a moving one second window for three different equivalence ratios. The increase in total duration of events is evident as LBO is approached, and is somewhat different than the number of events (Figure 43). This suggests that information on the average duration of events could be used in conjunction with the number of events to produce a robust measure of the proximity to LBO.

Comparing the total number of event and the duration of events for the case of equivalence ratio 0.748 from Figure 43&Figure 44 shows that the duration of the events increases more than the increase in the number of events. This suggests that the duration of the events has an increasing trend in time. As discussed in Chapter 3, the experiments very close to blowout were performed starting with hot walls, and the walls cooled down while the data was recorded. Thus the combustor is expected to become more statically unstable. This suggests that the duration of each event increases as the combustor approaches blowout.

Thus two main characteristics of the precursor events were identified for use in sensing of proximity to blowout limit. These parameters were shown to increase as the LBO limit is approached. The time variation of these parameters can be monitored by a control system and preventive measures employed when these parameters rise above a threshold level.

4.4 Practical sensor

This section discusses the changes needed from the lens based collection system to fiber optic based light collection, the issues regarding the sensor placement in the combustor flow field changes and choice of the light spectra, and their effect on the sensing methodology. The primary change from the data presented before this section and the sections that follow is the implementation of the fiber optic collection of light.

4.4.1 Fiber optic collection

The optical collection and sensor system (lens/ conventional PMT) used to collect the light would not be practical for use in most turbine engines. Thus, the potential of more robust systems based on optical fibers and miniature detectors was investigated. The first issue is the signal quality (e.g., signal-to-noise ratio) of the fiber sensor relative to that of the lens system.

The strength of the signals obtained from each system depends on its light gathering ability, which depends on the system’s collection solid angle, collection volume, and transmission efficiency of the optics. For the lens system, the product of the collection solid angle and collection volume was 190 times greater than for the fiber system. However, the lens system’s transmission efficiency was 20 times worse, due to the lower transmittance of the ND and interference filters. Thus, the fiber system had an overall light gathering ability about ten times less than the lens system. This would result in a maximum decrease of about 3 in signal-to-noise for the fiber system compared to the lens system assuming a shot-noise-limited signal. (Shot noise describes uncertainties associated with the discrete and random nature of photon and electron emission and is governed by Poisson statistics.)

Figure 45 shows time series data obtained using the fiber system near LBO, compared with that obtained with the lens system. These two data sets were not obtained from the same run, but from the same combustor and with the same equivalence ratio. A single precursor event is clearly visible in both cases (at ~250 msec for the lens setup, and ~170 msec for the fiber case).

Away from the extinction event, the fluctuations, or rms, for the fiber signal are clearly larger than for lens based detection. While this is partly due to the reduced signal (and increased shot-noise), the smaller collection volume also plays a role. For the more localized fiber system, the small turbulent reaction zones move in and out of the viewing area more frequently, increasing the OH signal fluctuations. Another difference between the two results is the absence in the fiber data of the large signal spike following the extinction event. Again, this is likely due to the smaller integration region for the fiber system. Fuel and air that stop burning during the extinction event are more likely to convect out of the imaged region when it is smaller. In most other ways, the signals from the fiber system resemble the lens data and are more than sufficient for LBO precursor detection.

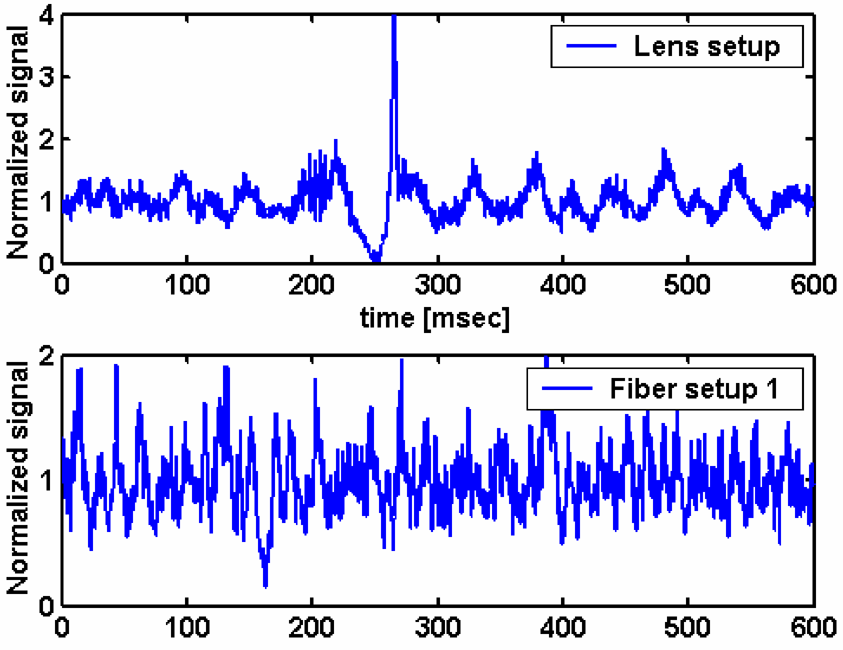

Figure 45. OH chemiluminescence near LBO obtained using the lens-based (top) and fiber-based (bottom) sensor setups. The signal traces are from two different runs, but the same ϕ. The signals are normalized to have a unit mean.

4.4.2 Sensor location

Since the precursors correspond to local extinction and reignition events, the location of the optical sensor becomes very important. The stabilization point in a combustor is often near the injector/inlet. When stabilization is lost, the flame extinguishes over a wide region near that point. Thus the optical port needs to be close to the injectors, but need not be looking directly at the injectors. The optical ports should also be placed such that the fiber can withstand the severe conditions in the combustor. The fiber used in this study could operate effectively at relatively high temperatures (~1200°C). Higher temperature requirements may require cooling. As discussed earlier, partial coating of the fiber in the combustor does not necessarily disrupt the LBO sensing, since the detection method discussed here do not rely on absolute signal, only how the signal changes over short times.

The fiber ports used in our study are located to observe the region of major flame loss in our combustor (see Figure 46). Sensor 1 looks at the same height as that of the lens based collection system, but at a smaller volume of flame. Sensor 2 corresponds to the same probe volume as in sensor 1, but at a region much closer to the inlet of the combustor. This decreases the volume of the flame zone inside of the probe volume for sensor 2. Sensor 3, which is mounted in the head end of the combustor and looks downstream, views the largest region of flame compared to the other sensors.

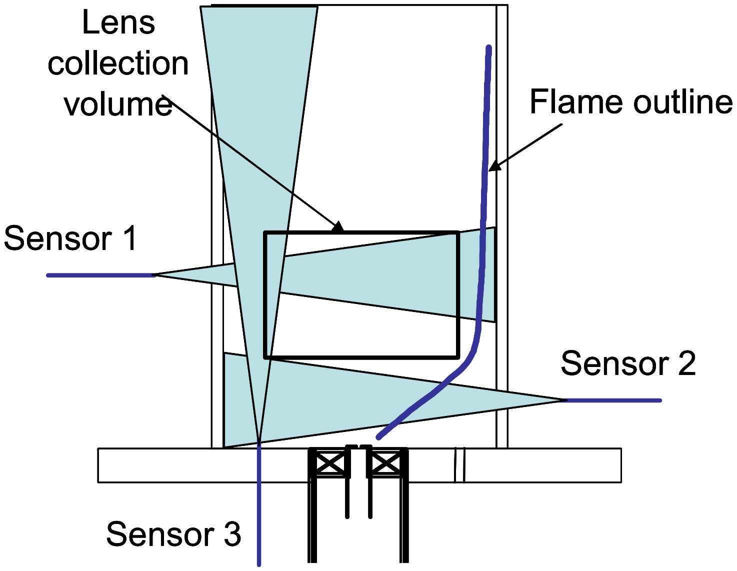

Figure 46. Schematic of the collection volumes of the lens and fiber optic setups

Experiments were performed to test the effectiveness of the sensor locations, with two fiber locations simultaneously studied. Figure 47 shows the comparison of the signals from locations 1 and 2. To facilitate the comparison, the data are normalized to have the same mean. There is a slight variation in the precursor shape in the two locations. The sensor at location 1 sees a longer precursor than at location 2. The time traces on the right in Figure 47 are the signal from the same run, but 3.1 second later. While sensor 1 monitors another extinction event, sensor 2 does not. While the reverse (an event on sensor 2 and not 1) also happens occasionally, sensor 1, the upper sensor, generally sees more events than the lower sensor. This is evident in Figure 48, which shows the 1 second window event count for both locations near the LBO limit. It is also interesting to note a spike in the signals from both sensors 1 and 2 just after the extinction event seen by sensor 1 in the delayed (right) plots of Figure 47. This suggests that the reignition event following the extinction travels upstream towards the fuel injector. Evidence of this has also been observed in the high speed visualization.

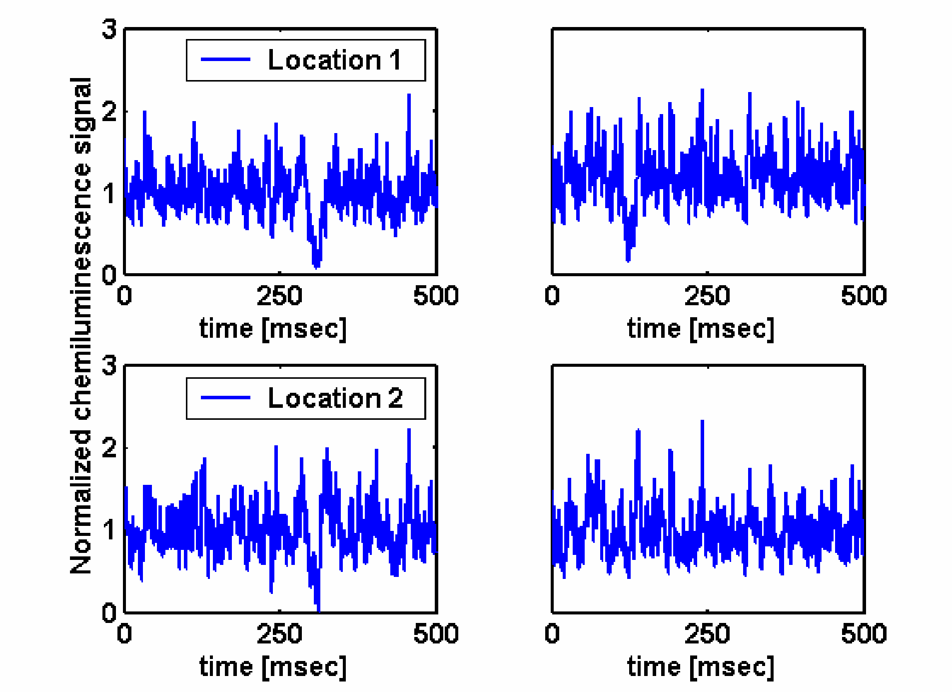

Figure 47. Precursor signals as observed from locations 1 (top) and 2 (bottom). The plots on the right show results for a period 3.1 seconds after the left plots.

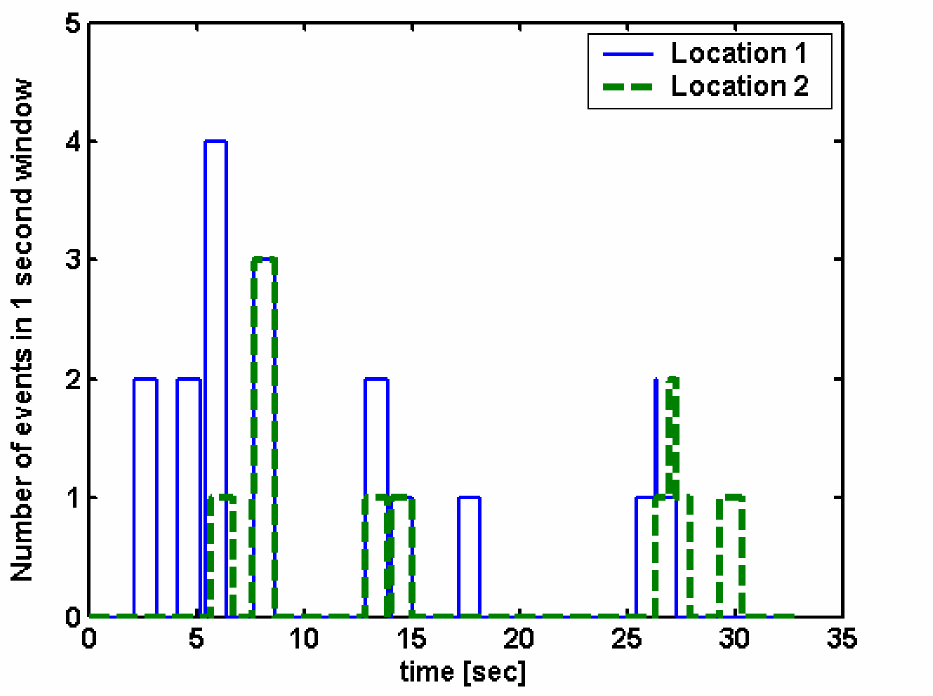

Figure 48. Comparison of detection from fiber locations 1 and 2 for ϕ-ϕ_{LBO} = 0.006.

Figure 49 shows a comparison of signals from sensors 1 and 3, while Figure 50 shows the corresponding number of events in a moving one second window. The sensor at location 3 always records more precursor events than at location 1. Review of the time series data shows that sensor 3, which looks from the upstream (head) end of the combustor, senses all the events seen by sensor 1 (side view) plus additional events. As illustrated in the right side plots of Figure 49, signal loss for sensor 1 is not as pronounced and may not cross the chosen threshold limit. This suggests that a larger portion of the combustion volume seen by the head end sensor experiences extinction.

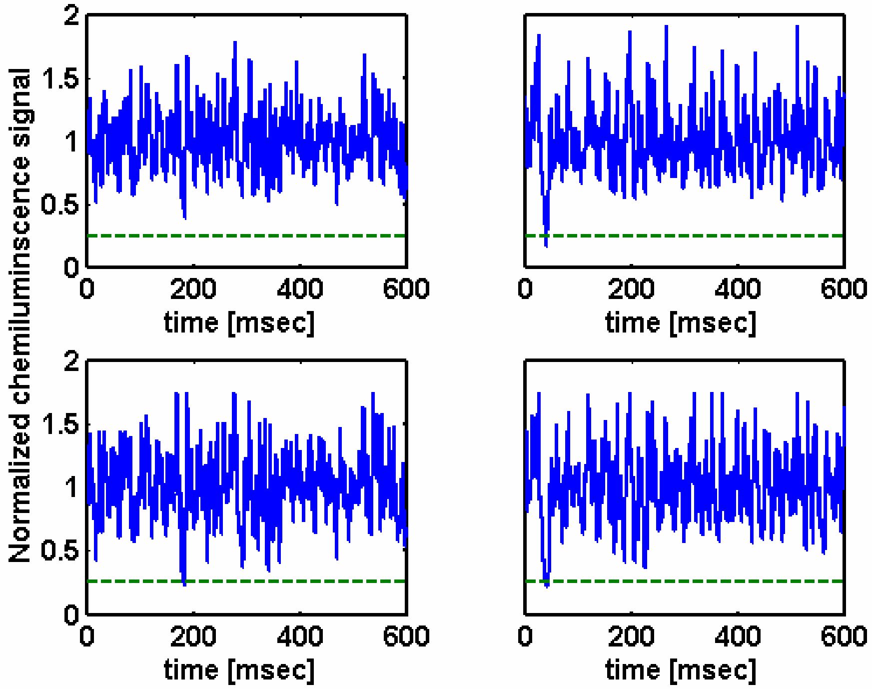

Figure 49. Precursor signals as observed from locations 1 (top) and 3 (bottom) and threshold. The plots on the right show results for a period 2.1 seconds after the left plots.

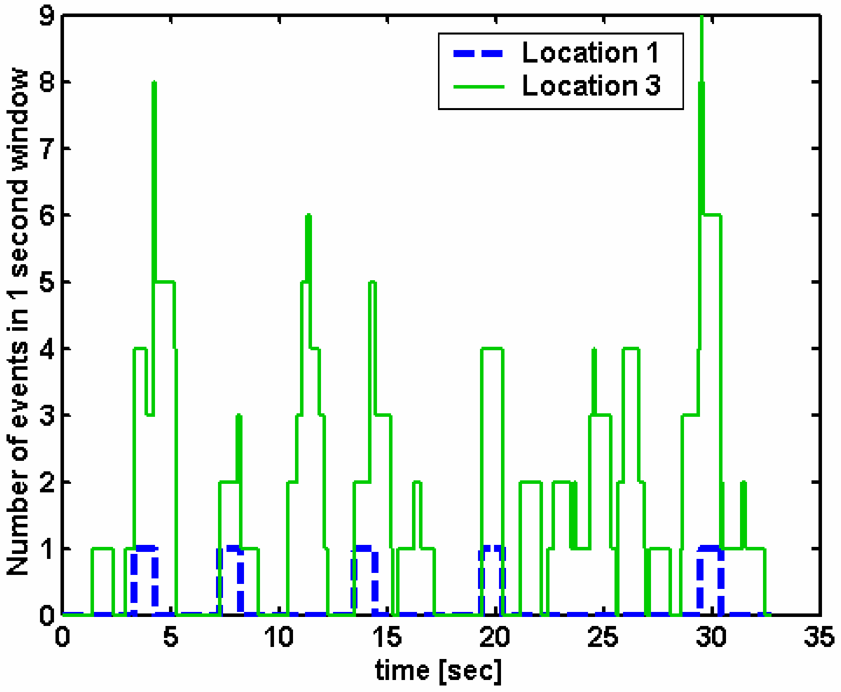

Figure 50. Number of precursors in a moving 1sec window for the fiber locations 1 and 3 for ϕ-ϕ_{LBO} = 0.006.

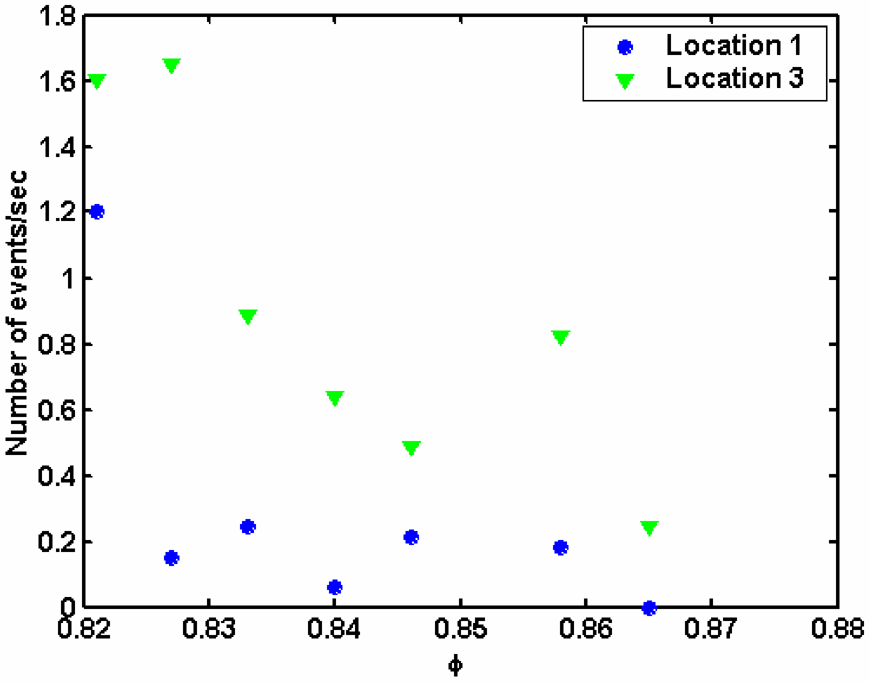

Figure 51. Number of events/sec as sensed by sensors 1 and 3. The data is an average over 33 seconds.

Figure 51 shows the proximity parameter based on number of events per second as seen by sensors 1 and 3. The downstream looking sensor (location 3) is more sensitive to the onset of LBO than the side looking sensor (location 1) for the same threshold-to-mean-signal ratio. Mounting the fiber in the head end of the combustor is doubly advantageous, since this is a cooler region of the combustor and typically more accessible for mounting the fiber. One must remember that the threshold-to-mean-signal ratio was selected to be 25%, and that changing the threshold limit could change the sensitivity of the sensor. Thus, each sensor location could require a different threshold setting for optimal performance.

4.4.3 Combustor configuration

The OH chemiluminescence signal and thresholding approach were used to detect precursor events for two different combustors, a non-premixed, liquid-fueled, single-cup sector model and a methane-air premixed swirl/dump combustor (Figure 57). The thresholds used to detect the events were 30% of the mean signal for the methane-air combustor and 45% of the mean signal for the liquid-fueled combustor. The combustors have very different LBO limits (ϕ_{LBO} for the non-premixed combustor is based on the overall fuel and air flow rates). Thus the data is presented as a function of equivalence-ratio-standoff from LBO, which is the difference in equivalence ratio of operation to that of LBO limit, i.e., ϕ-ϕ_{LBO}. Thus blowout occurs when this parameter is zero. As is evident from the figure, the average number of precursor events increases in both combustors as the LBO limit is approached.

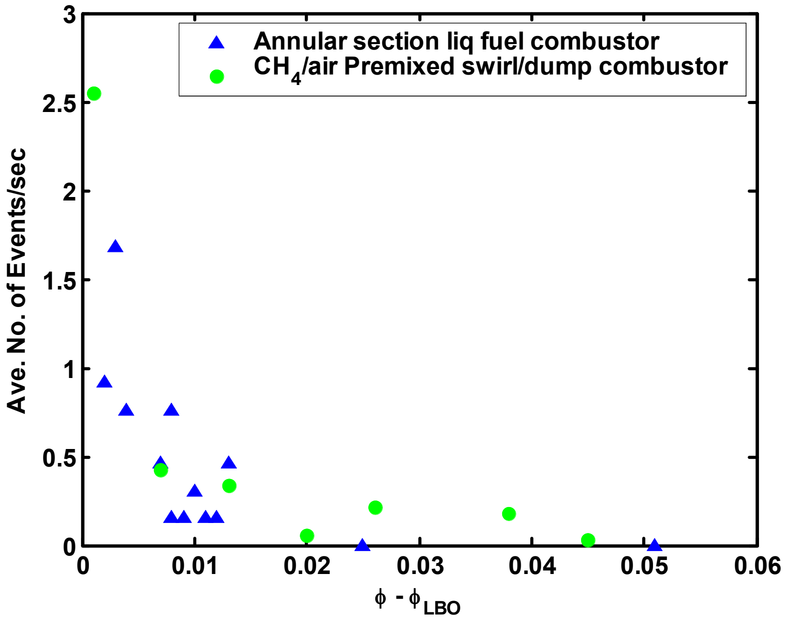

Figure 52. Number of chemiluminescence-based, LBO precursor events/sec in two combustors as a function of proximity to the LBO limit (ϕ_{LBO} = 0.821 for the methane combustor and 0.352 for the liquid-fueled combustor).

These results show that chemiluminescence from a combustor can be effectively used to detect LBO precursors and assess the proximity to LBO. This can be achieved in both premixed methane/air swirl dump combustor and liquid fueled partially premixed combustor. Although data has been shown for only two of the combustors, this method was found to give similar results in other variations of the swirl dump combustors studied.

4.4.4 Choice of wavelength

All the prior results were based on OH chemiluminescence signals, which occur in the ultraviolet spectrum. Visible CH chemiluminescence signals also show the capability to detect these LBO precursors (see Figure 53). The time traces shown were obtained simultaneously from the swirl dump combustor during a run close to LBO limit. The experiments were performed with the room lights turned off and thus there were no significant visible background radiation that can interfere with the measurement. The signals were normalized to have unit mean for comparison and a threshold of 50% mean is also shown. Although the general behavior with time is the same for both OH* and CH*, there are small differences during the events. The OH* extinction events are usually more distinct compared to the CH* events. Thus the thresholding method might not give the same results for both.

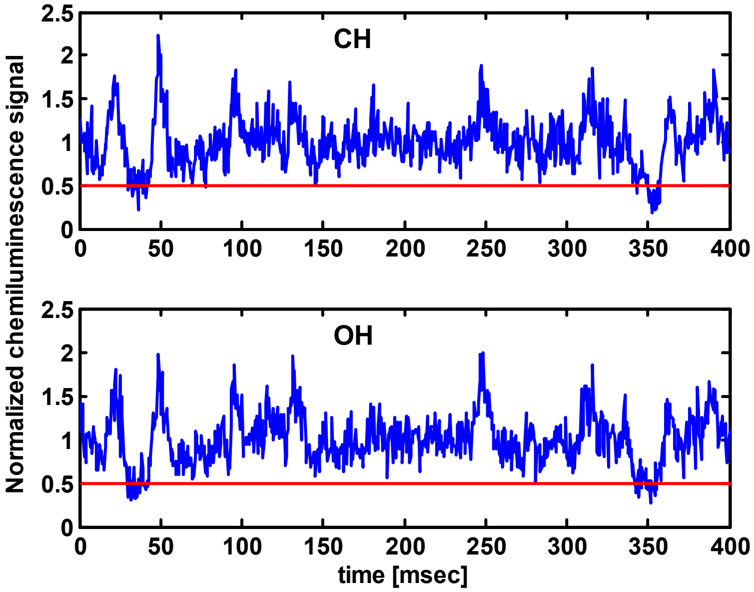

Figure 53. Chemiluminescence signal from the combustor showing both CH and OH signals close to blowout.

Also the black body radiation from the hot walls may interfere with the blue CH emission while the UV OH emission does not have significant interference. Further, CO_2 chemiluminescence which is predominant in that combustor[78] could also decrease the sensitivity of the method if the dependency on the reaction rates is different for CO_2. Further investigations are needed to explore this aspect of choice of wavelengths.

4.5 Summary

This chapter investigated the near blowout behavior of the swirl dump combustor. The chemiluminescence emission from flame was used to study the combustion process. In particular chemiluminescence emission from OH radical was used since the UV radiation does not have interference from the black body radiation of hot walls. General unsteadiness in the combustor observed was used to deduce the proximity to blowout by spectral and statistical methods.

Detailed analysis of the time series data revealed temporary flame loss events near blowout limit. These events were investigated through high speed visualization and were found to be large scale change in the flame shape followed by recovery of the flame. These local extinction-reignition events were recognized as precursor events to blowout of the combustor. They were identified from the time series data by use of thresholding methods. The number and duration of these events were found to increase as the LBO limit was approached. Double threshold method was developed to reduce multiple counting of the events due to noise in the signal.

In order to develop a practical blowout sensing system, miniature photomultiplier tubes and fiber optics were used. The behavior of the sensor data was found to depend on the collection volume of the sensor. Three different locations of the fiber sensor were used and were found to give different sensitivities to blowout precursors. The shape of the precursor events were observed to vary with each sensor location. Sensor location 3 was found to give the highest sensitivity to blowout precursors. This might also be the most practical because this region is expected to have relatively lower temperatures.

Furthermore, a fiber probe viewing downstream can be installed easily in the inlet section to view through the swirl vanes or the cooling air holes.

The method of identifying precursor events to blowout was also found to be effective in predicting approach of blowout in both methane/air swirl dump stabilized combustor and liquid fueled partially premixed swirl combustor. The method was also found to be effective in variations of the gas fueled combustor. It was also shown that CH chemiluminescence could also be used to detect the onset of blowout by detecting precursor events.

The next major part of this research work is the implementation of this sensor in a blowout avoidance control system. Further, understanding the fluid mechanics of the precursor events would allow us to explain the various characteristics of the precursor events observed.

Chapter 5

Control of LBO

Chapter 4 described various sensing methodologies for detecting proximity to LBO limit. This chapter illustrates the application of the threshold-based sensing method in conjunction with an active control system to avoid blowout of the combustor. Two types of control systems are illustrated. The first controls the fuel flow rate to minimize NOx emissions while keeping the combustor from blowing out. The second controller activates an alternate stabilization method without changing the overall fuel-to-air ratio.

Section 5.1 describes the development of total fuel control for minimizing pollutant emissions. Section 5.2 describes the alternate stabilization method developed for fuel split control. Section 5.3 presents the control methodology developed to avoid blowout without altering the power setting of the combustor, and the control results. Section 5.4 summarizes the results from this chapter.

5.1 Total fuel control for minimizing NOx

When equivalence ratio is increased from a lean value towards stoichiometric, while keeping the air flow constant, the combustor gains static stability. However, burning a richer mixture increases the penalty of NOx emissions from the combustor. Thus there exists an optimum for operating the combustor as safely as possible with minimum possible NOx emissions.

A control system was built to minimize the NOx emissions from the combustor by decreasing the total fuel flow rate, while watching for blowout precursor events from the optical sensors. The exhaust gases from the combustor were sampled from the center of the combustor exit and fed to a gas analyzer. The analog NOx emissions output from the gas analyzer was connected to a control computer. The output from the control computer was used to actuate a set of solenoid valves for controlling the fuel flow rate to the combustor (see Chapter 3 for details). The air flow rate was maintained constant throughout the experiment. The control computer operated at 20 kHz. The gas analyzer had a slow time response due to delays caused both by the flow time through the sampling line and the response of the detector. The overall time delay was around 15 seconds.

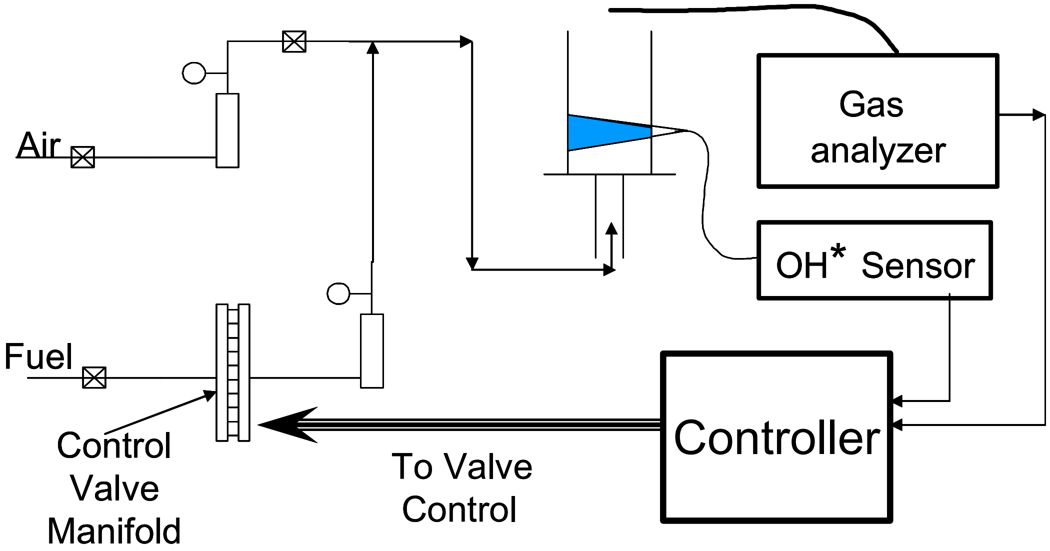

Figure 54. Schematic of the flow control system and instrumentation for total fuel control.

The control algorithm for minimizing the NOx reading was a simple search-based optimization approach. The controller makes a change in the flow rate and then waits for 20 seconds to get the new reading from the gas analyzer and then modifies the fuel flow rate accordingly to go in the direction of lowering NOx. Another part of the controller monitors the signal from the optical sensor for blowout precursors. The threshold value was set to 50% of the mean signal over the last one second. When precursor events are encountered, the controller increases the fuel flow rate by a fixed value for each event detected.

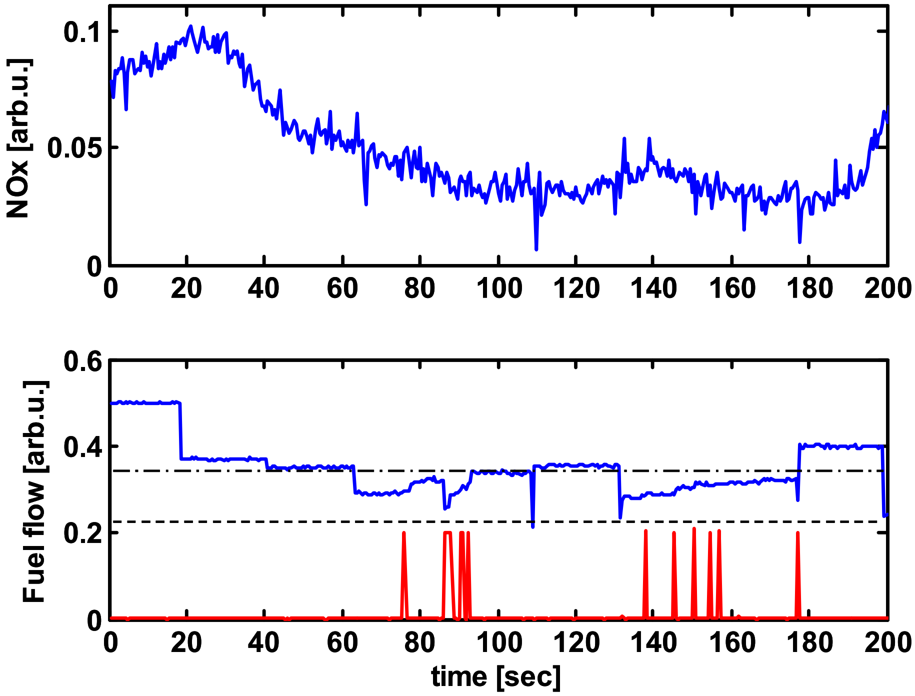

Figure 55. Time series data from total fuel control experiments. The top plot shows the variation of NOx emissions as a function of time. The bottom plot shows the fuel flow rate as a function of time and the alarm signals (the blips) detected. The nominal operation (dot-dash) line and the blowout flow rate (dashed line) are also indicated.

Figure 55 shows the data obtained from the operation of this controller. It can be seen that the fuel flow was increased whenever LBO precursor events were detected. The events occurred when the fuel flow rate was low enough that the combustor was near the LBO limit (dashed line) for the given air flow rate. The data acquisition system was acquiring data at a slow rate and thus was missing some of the event alarm signals. The combustor was operating at a nominally fixed operating condition near the blowout limit as shown by the dot-dashed line on the plot. This operating condition depends on the threshold picked for detecting the precursor events and the increment value per event. Thus these parameters become the criteria for the operability limit of the combustor.

While the data shown was recorded for only 200 seconds, the combustor was operated over a much longer time at the same nominal conditions. Thus it was shown that the combustor could be operated with essentially minimum NOx emissions without loss of stability. More importantly, the controller was able to achieve this operating point without *a priori* information on the blowout limit of the combustor. The main shortcoming of the implemented control system is that the power output from the combustor was not set, rather the power was adjusted to minimize NOx. Nevertheless, this simple control system outlines the feasibility of using the sensing methodology for avoiding blowout of a combustor.

5.2 Fuel split Control

A more practical control system would allow for stable combustor operation at a power level independently chosen. Part of such control system would thus require varying the relative stability without changing the power output - in this case, the total fuel flow rate. To enhance combustor stability without changing power requires either some method of strengthening the existing stabilization mechanism or providing a better one. While external heat or energy can be added to the combustor, for instance in the form of an electric spark, the method used here was to enhance the existing stabilization points better by increasing the local equivalence ratios near the stabilization points through pilot fuel addition.

Pilot flames are one of the common methods used in industrial combustion systems for stabilizing a combustor. The pilot flame typically burns closer to stoichiometric conditions and anchors the weaker flame of a lean main mixture in the high velocity conditions of the combustor. The overall fuel is split into main and pilot flows and the pilot fuel is injected into the combustor at specific locations so as to strengthen the stabilization points. This non-uniform distribution of fuel inside the combustor is expected to strengthen the stabilization points while not seriously weakening the other regions, which are deprived of fuel. However, this method may increase the NOx penalty due to locally richer operation.

5.2.1 Alternate stabilization

The first step in developing such a control system is to find an alternate stabilization mechanism that is effective in stabilizing the combustor when the main flame is about to blowout. This mechanism should not have high NOx penalties nor should it hamper detection of blowout of the combustor. It should also have a fast time response and be easy enough to implement without major changes to the combustor, in order to minimize the cost of modification.

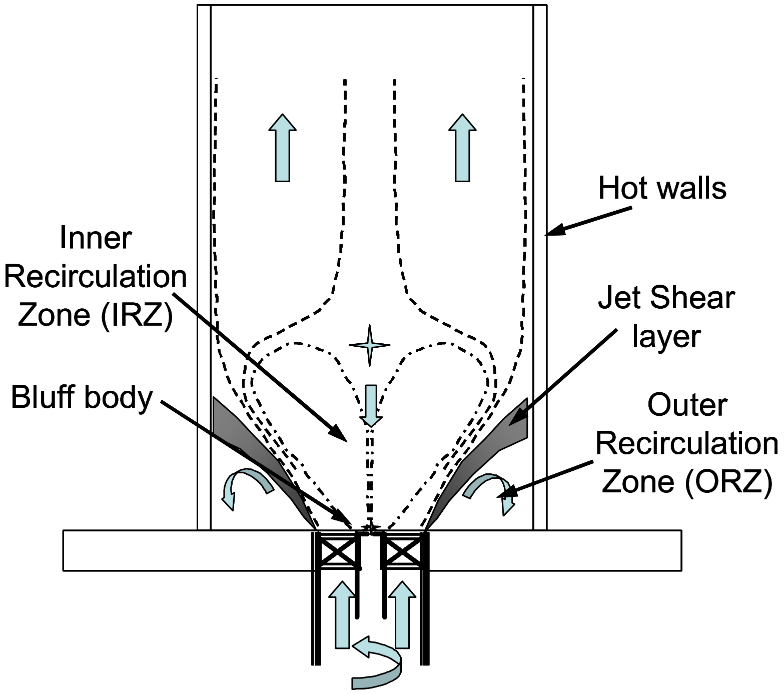

Figure 56. Schematic of the combustor with various stabilization mechanisms.

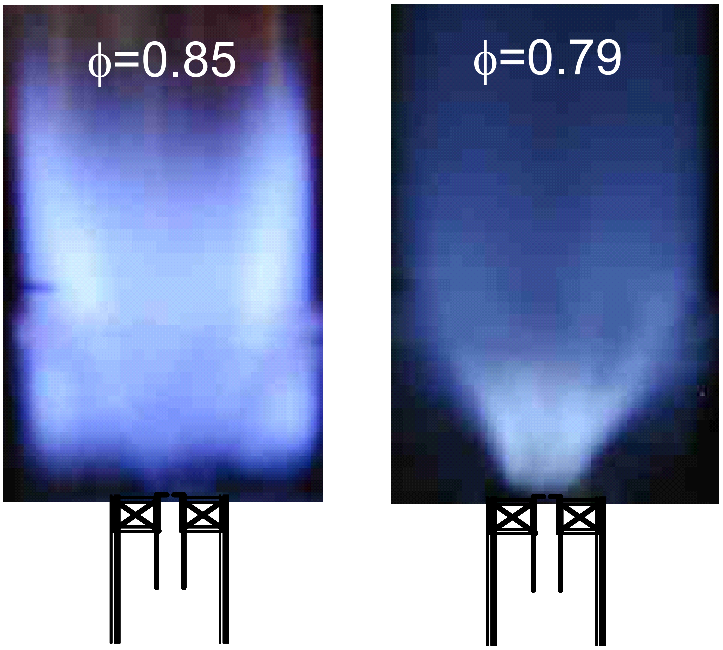

Figure 57. Long exposure photograph of the flame for two different equivalence ratios.

The current swirl-dump stabilized combustor has the following possible stabilization mechanisms (see Figure 56): the central recirculation zone (CRZ) created by the swirl, the outer recirculation (ORZ) created by the dump plane, the annular bluff body in the center of the injector, the hot combustor walls or a combination of these. Figure 57 shows photographs of the flame for two different equivalence ratios. The combustor blowout limit was 0.75 at the flow rates used. As the blowout limit is approached, the outer recirculation flame is lost. The flame appears to be stabilized on the inner edge of the annular swirling jet and extends all the way to the wall. Thus the stabilization is likely either be due to the bluff body or the inner recirculation zone.

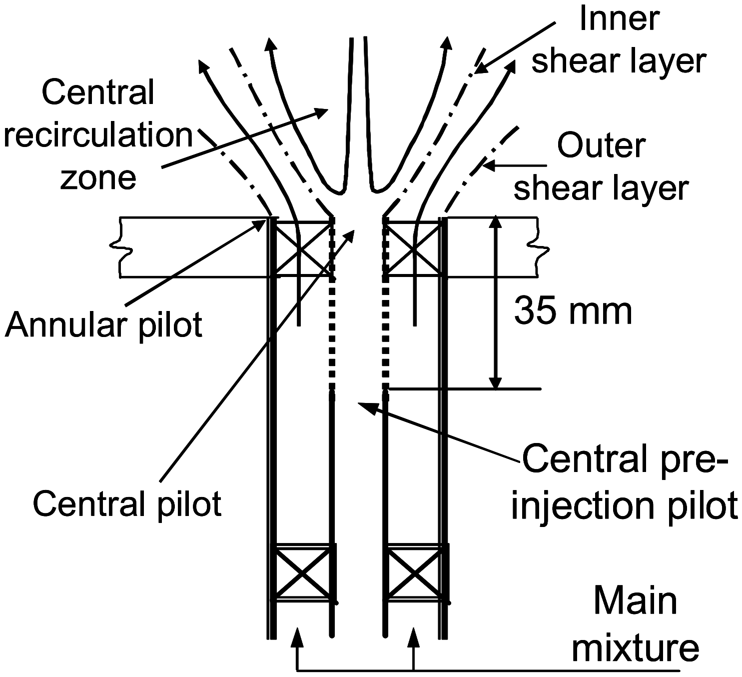

Figure 58. Schematic showing the various pilot options discussed.

The different locations tested for injection of the pilot fuel are shown in Figure 58. A central pilot injects fuel into the axis of the combustor and into the inner recirculation zone, while the annular pilot injects fuel near the outer shear layer. The central pilot was injected through a single hole in the center of the central bluff body of the swirler. This arrangement was expected to increase the equivalence ratio near the base of the flame seen in the average images, and thus would be expected to stabilize the combustor. The annular pilot injects fuel into the outer shear layer between the main premixed jet and the outer recirculation zone through a set of 8 holes along the perimeter of the main flow jet. This arrangement would be expected to stabilize the outer edge of the mixture and could help stabilize the flame near the hot walls, which in turn could stabilize the near inlet flame through the inner recirculation flame.

The third pilot arrangement was the central pre-injection pilot. The pre-injection pilot is a modification of the central pilot, where the pilot flow tube is not inserted all the way up to the inlet of the combustor. By introducing the fuel ahead of the final swirler, it has some time to radially mix into the inner regions of the primary fuel/air mixture. This arrangement introduces the fuel to the near inlet flame region seen in the average flame photographs (Figure 57). This arrangement also replaced the central bluff body with an annular ring like bluff body formed by the inner hub of the swirler, allowing part of the flow to go through the center. This decreased the swirl near the center and removed the bluff body wake from the flow field.

Experiments were conducted to determine the effectiveness of each of these piloting schemes. To compare the effectiveness of each, experiments were conducted at constant air flow rates, and the overall fuel flow rate was decreased while maintaining a fixed pilot flow fraction. The total equivalence ratio at blowout for various pilot fractions was recorded. For a piloting method to be effective, the blowout equivalence ratio should decrease as the pilot fraction is increased. Figure 59 shows the resulting blowout equivalence ratios for the three pilot methods studied.

The results show that the central pilot was not effective in decreasing the blowout equivalence ratio of the combustor. There was a marginal improvement in the overall blowout equivalence ratio at low pilot fractions (3-6%). At higher pilot fractions, the combustor is less stable. This may be due to the changes in the recirculation zone due to the momentum introduced by the pilot jets into the center of the combustor. For example, it could move the stagnation point in the combustor if it reduced the strength of the central recirculation region by increasing the axial momentum there. Changing the jet velocity (by changing the injection hole diameter) and the equivalence ratio of the pilot flow (by adding air to the pilot) in the central pilot configuration did not change the behavior of the combustor significantly. In summary, central pilot injection was counter productive, reducing the combustor stability.

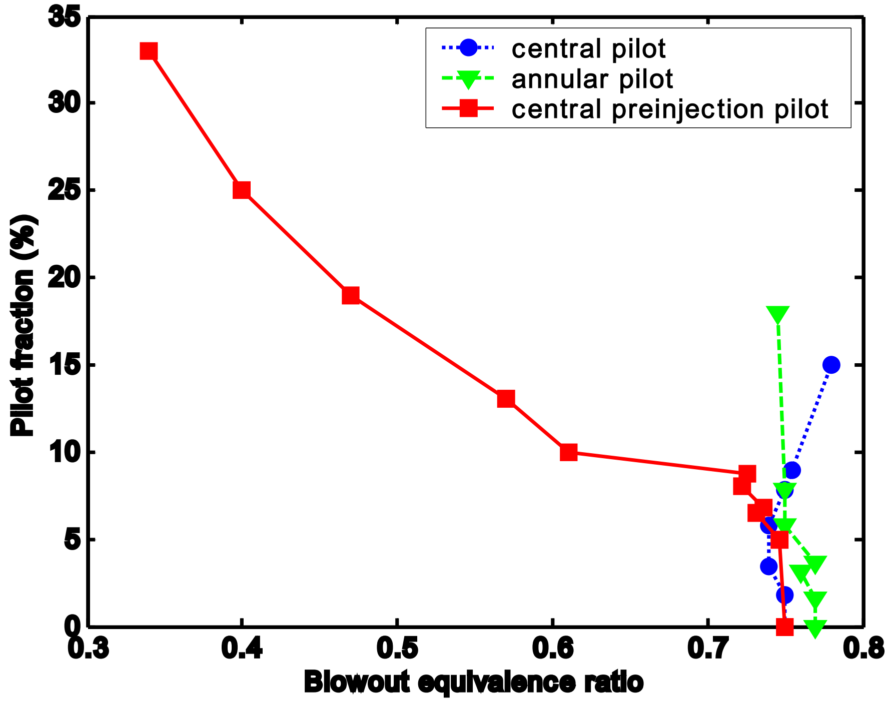

Figure 59. Effect of various pilots on the blowout equivalence ratios.

The annular pilot, on the other hand, reduces the overall blowout equivalence ratio, but only slightly as the pilot fraction is increased beyond 5%. This combustor configuration had a slightly higher blowout equivalence ratio at zero pilot fraction compared to the other configurations. This was because the combustor was newly manufactured to incorporate the annular pilots, while the other two configurations were modifications of the original combustor. The lack of effectiveness of the annular pilot may be due to the fact that the flow field in the outer shear layer mixes the pilot fuel with the main flow too quickly. If the fuel is well mixed with the main flow by the time it reaches the flame zone, there is little change in local fuel-air ratio and thus little effect on flame stabilization.

The central pre-injection pilot was found to be effective in decreasing the LBO limit for pilot fuel fractions above ~5%. Increasing levels of piloting produced ever lower overall LBO limits. It was necessary, however, to add some air to the pilot fuel injector to produce the results shown in Figure 59. This requirement, although not investigated fully, could be due to the increased velocity of the pilot jet with the addition of the air, or the partial premixing provided. The air flow needed to generate effective piloting also produced a velocity at the exit of the pilot tube that nearly matched that of the surrounding annular main flow velocity. Thus the shear layer between the two flows is reduced, which would lower mixing between the two streams.

Based on these results, the central preinjection pilot with air addition was selected for implementing the LBO control system. Additionally, a constant fraction of the total air is sent through the pilot injector in order to maintain a nominally constant velocity field. Thus in all the experiments involving control system (whether controller is ON/OFF), the fuel flow rates are varied between main and pilot flows maintaining the ratio between the main and pilot air flow rates.

5.2.2 Effect of pilot on LBO sensing

Since the pilot injection could change the near-LBO dynamics of the combustor or the spatial extent of the active combustion region, it also might influence the efficacy of the LBO precursor sensing. Thus the effect of piloting on the sensing technique was investigated through open loop tests. Figure 60 shows results obtained at different overall equivalence ratios and different pilot fuel fractions. The LBO limit for each pilot fraction is indicated by the vertical lines (as indicated previously, the LBO limit moves to leaner mixtures with increasing piloting). The event rate (averaged over 32 seconds) is indicated for each pilot case.

The threshold based sensing approach described in Chapter 4 successfully tracks the change in the LBO limit. The number of events increases rapidly as the LBO limit is reached for a given pilot setting. The number of events detected far from blowout is nearly zero, though it appears to increase slightly for higher pilot fractions. Thus this pilot configuration is effective in stabilizing the combustor and does not hinder the blowout proximity detection method.

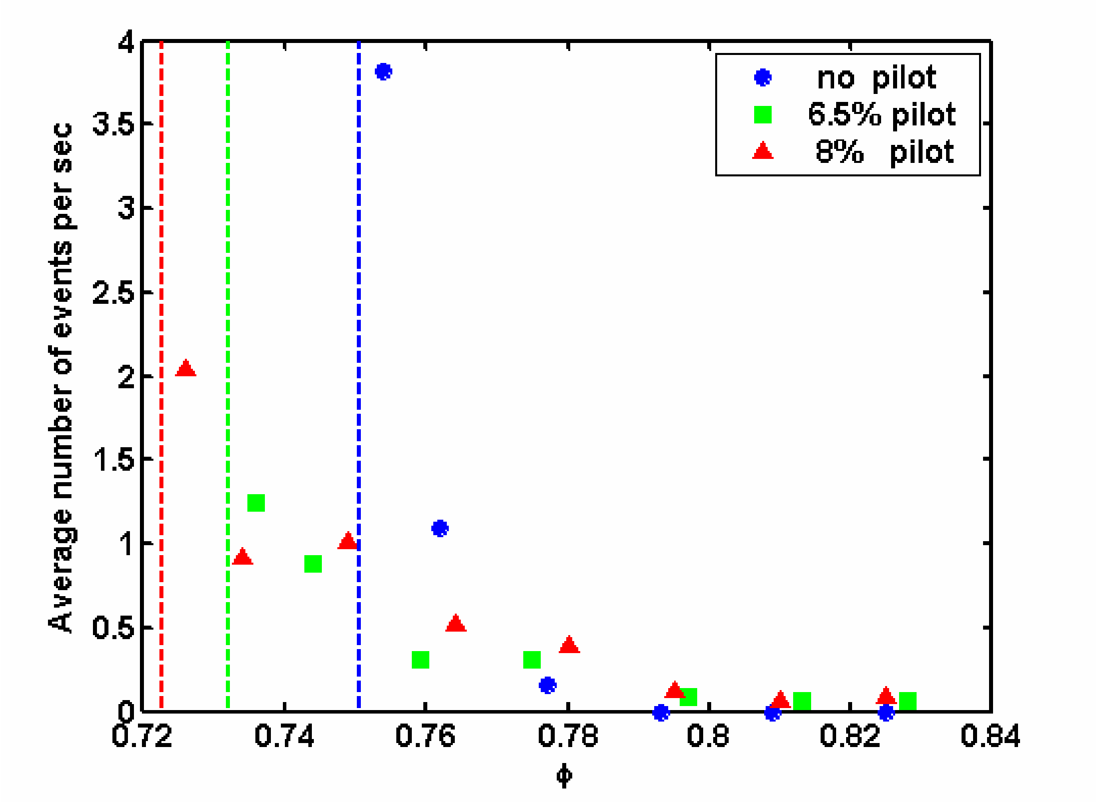

Figure 60. Average number of events per sec as a function of equivalence ratio for various pilot fractions, with nominally same velocity field. The dotted lines indicate the respective LBO limits for each case.

5.2.3 Effect of pilot on NOx

Because the pilot introduces local regions of higher equivalence ratio, it could also increase the overall NOx emissions from the combustor. The rest of the combustion region, however, has a lower equivalence ratio since part of the fuel has been redirected to the pilot. Thus it could produce lower NOx levels. Since the LBO limit for the piloted system is leaner, the piloted combustor allows operation at a lower overall equivalence ratio without loss of safety. Thus it is important to determine the effect of piloting on NOx emissions.

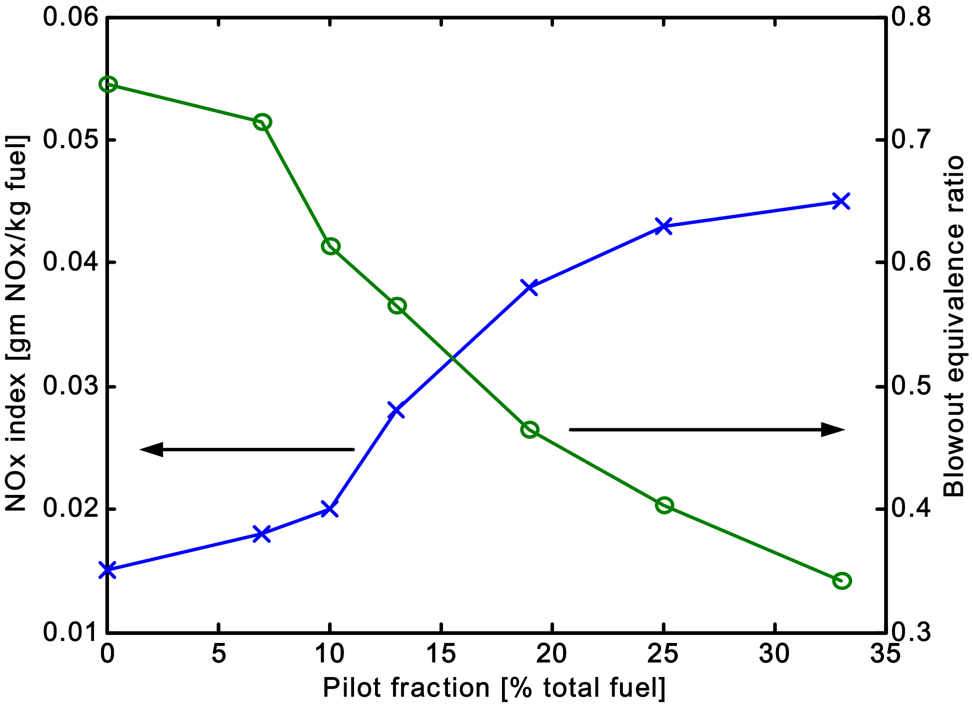

Figure 61. Variation of NOx emissions (x) and overall equivalence ratio at blowout (o) as a function of pilot fraction for a fixed air flow rate.

Figure 61 shows that the NOx emission index increases as the pilot fraction increases. At a given overall equivalence ratio, zero pilot fraction case produces the least NOx emissions. This indicates that increasing the pilot fraction increases the NOx penalty and thus acts contrary to the primary objective of reducing pollutant emissions. However, one should also take into account the fact that the combustor is made more stable and thus the operable regime is extended to leaner mixtures by increasing the pilot fraction. The figure also shows the overall equivalence ratio at which the combustor blew off at a given pilot fraction. This blowout limit can be determined by a separate set of experiments where the nominal velocity field and the pilot split are kept constant and the overall fuel is decreased until LBO occurs. This plot shows the benefits of higher pilot fractions. The combustor can be operated at an overall leaner mixture to produce lower NOx emissions.

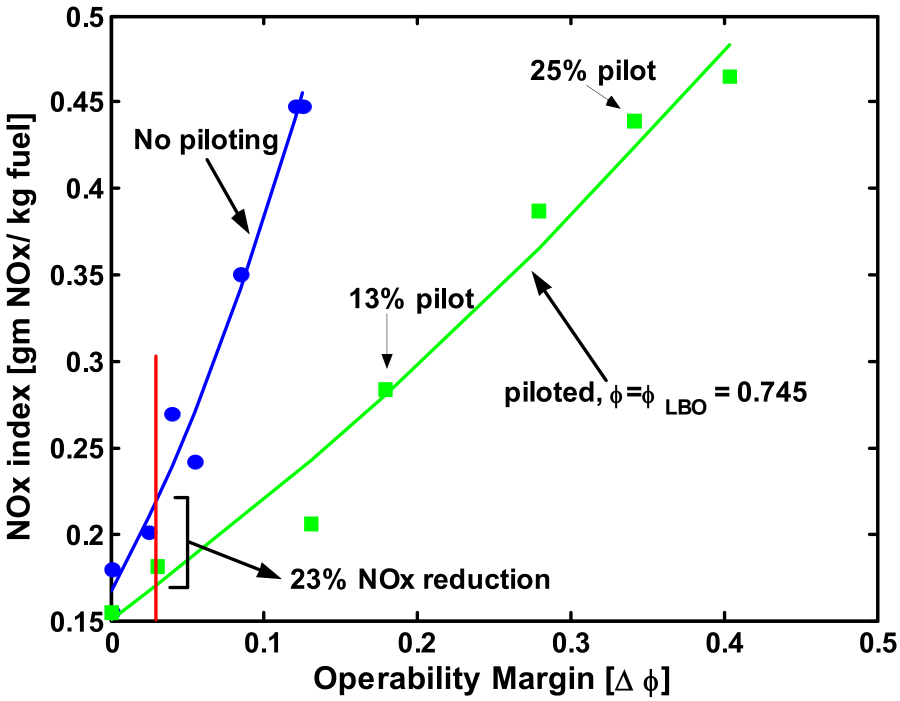

Figure 62. NOx as a function of operability margin for piloted and unpiloted operation of the combustor.

To compare NOx emissions for piloted and unpiloted conditions, it is necessary to define an operability margin that includes the added stability provided by piloting. For piloted conditions, the operability margin is defined to be the difference between the operating equivalence ratio and the LBO limit for the same pilot fraction. A comparison of piloted and unpiloted cases is shown in Figure 62, which provides the NOx emission index (EINOx) as a function of the operability margin. The overall equivalence ratio for the piloted case was maintained at the LBO limit of the unpiloted combustor. It should be noted that EINOx decreases with a decrease in pilot split fraction, but this also decreases the operability margin. Also, it can be seen that piloted combustor has a lower NOx index compared to the zero-pilot combustor *for the same operability margin*. For example at a margin of 0.04 (6.5% pilot fraction), EINOx is reduced by 25% compared to the unpiloted case. A similar result has been observed in turbulent, premixed, coflow flames.[79]

5.3 LBO control methodology

The observations so far can be summarized as follows. There are (nonperiodic) precursor events that occur before LBO, and they can be detected by observing the optical emissions from the combustor. Piloting increases the stability of the flame in the combustor and thus moves the LBO limit to leaner values. Thus there is a gain in the operability range by increasing the pilot fraction, but there is a penalty in increased NOx emissions. Thus there is an optimum to be reached between these conflicting factors. This section describes the control methods used to operate the digital solenoid valves in order to rapidly control the fuel split, the control algorithm and tuning employed to optimize the combustor operation, and results of the combustor under closed-loop control.

5.3.1 Fuel valve control

The parameter controlled by the controller is the ratio between the pilot and main fuel via the valve manifold. The miniature solenoid valve manifold was operated in PWM (pulse width modulated) mode at 25 Hz. The opening and closing times of the valves induced a cutoff and saturation, respectively, in the response to a commanded duty cycle signal. To mitigate the undesired effects due to valve opening and closing delays, the PWM command was increased by the appropriate valve response times and the command was distributed among two valves such that no single valve had to operate at over 50% duty cycle. The opening and closing times were both found to be 1% of the PWM period, or 0.4 milliseconds. Therefore, a command to open 2.9 valves results in two completely open valves, one valve receiving a 51% duty cycle command (and outputting 50% duty cycle due to opening time response), and a second valve receiving a 41% duty cycle command (and outputting 40%). The command signal resolution is 1% duty cycle (valve control parameter), and with the ten valve setup, varied from 0% to 1000%, with each 100% corresponding to another fully open valve.

5.3.2 Control algorithm

In the current setup, control authority is available over the fraction of total fuel distributed to the pilot. The OH chemiluminescence signal provides the feedback necessary to control the pilot/main fuel split fraction. The control algorithm is an event based control in which the absence of LBO precursors leads to the decrease of pilot fuel fraction to minimize NOx. When LBO proximity is detected, the control system responds by increasing the pilot fuel fraction. The main objective of the control algorithm is to maintain the pilot split fraction at a minimum while maintaining operational stability. In this arrangement, the controller has no input about any flow conditions (fuel or air flow rates, pressure, etc.) in the combustor, except for the precursor detection.

Control actuation is based on the number of precursor events detected in a time window, as seen in Figure 63. An alarm is declared if more than a critical number of precursors are observed in a specified time window. When an alarm is declared, pilot fraction is increased (by X%). This increment is proportional to the number of events counted during the observed time window. This actuation effectively distributes a larger fraction of total fuel to the pilot when LBO proximity is close (more events in a given time). The control algorithm declares an ongoing event when the sensor signal drops below the lower threshold, and it continues until the signal returns to a point above the upper threshold. During this time, small increments (of Y%) are made to the pilot fraction. Thus during longer events, which indicate closer proximity to LBO, the system will provide a larger increase in pilot fuel fraction. If no alarms occur during a preset time limit (T), the combustor is considered to be in a safe operating condition, and the pilot fraction is decreased (in multiples of Z%). The decrement is proportional to the time elapsed since the last detected alarm. This improves the response time of the controller to changes in operating condition of the combustor. As noted previously, two threshold levels are used: a lower threshold for event start, and an upper threshold for event end. This allows for better noise rejection, and can be customized to suit specific combustors. To account for the drift in the signal levels due to power setting variations and partial soot deposition on the fiber tip, the mean value of the signal, which is used to normalize the thresholds, is updated every second with the average of the sensor signal over the previous second.

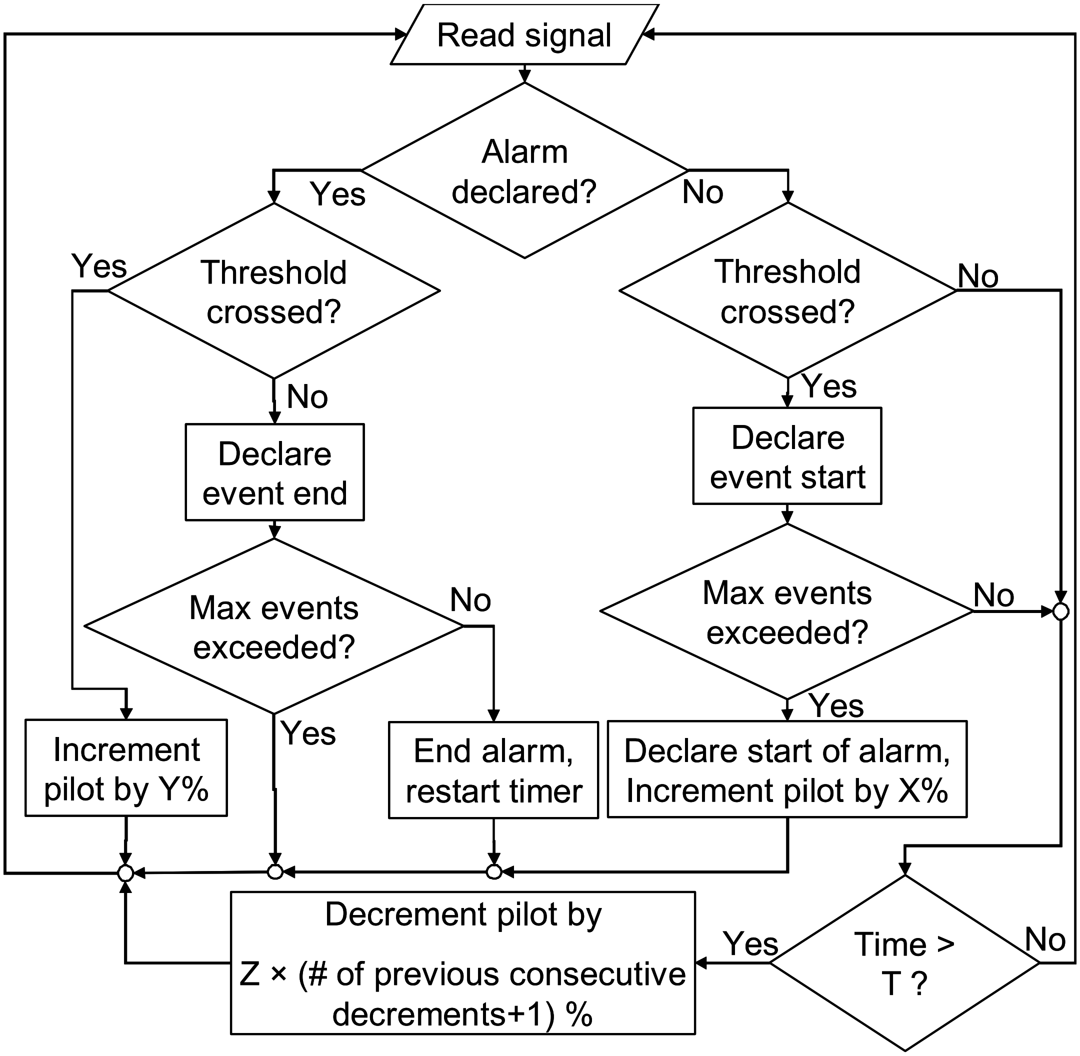

Figure 63. Algorithm followed by the controller.

Several parameters may be manipulated to achieve an acceptable tradeoff in terms of response time and sensitivity. The threshold values can be tuned to change the precursor event detection sensitivity. Time based quantities such as signal mean, alarm count, and time limit depend upon the duration of the time window in which these parameters are evaluated. Longer times for calculating the mean can lead to increased possibility of false alarms due to power setting changes in the engine. Shorter times increase the likelihood that the mean will be affected by the precursors, thus influencing the sensitivity of the event detection method. The threshold values used will also affect the noise rejection capability of the sensor. Since the algorithm uses the absolute numbers for events instead of average number per time window, the length of the time window used to count the number of events will also become a parameter which affects the response of the controller.

Sensitivity of the control actuation is governed by the increments (X and Y), decrement (Z) and the wait time before decrement (T) to the pilot split fraction which describes the magnitude of the system response. The critical number of events for declaring the alarm will determine how close to LBO limit we can approach with this algorithm which avoids LBO. The waiting time T and the critical number of alarms add some dead response zone in the controller, which will reject noise and limit sensitivity.

5.3.3 Closed-loop control results

The control system was tested under two cases: one where the operating conditions were nominally steady and a second case where the air flow rate was independently varied. For both cases, the time window was set to one second, and the threshold levels were set at 35% and 40% of the mean signal. In addition, the maximum number of alarms allowed before the system begins to increase the pilot fuel was two (in the one second window).

To test the behavior of the controller at constant conditions, an experiment was conducted at an overall equivalence ratio that would result in blowout without any pilot fuel. Therefore, the system was started (before the controller was turned on) with two valves open. It can be seen from Figure 64 that the controller eventually attains a nearly stationary condition. The minimum allowable pilot fraction appears to be 14% based on the effective safety margin set by the chosen controller parameters. Since extinction precursors do occur somewhat randomly and because the controller always tries to keep lowering the pilot fraction in the absence of alarms, the system drifts between the minimum pilot fraction and a higher value of ~18%.

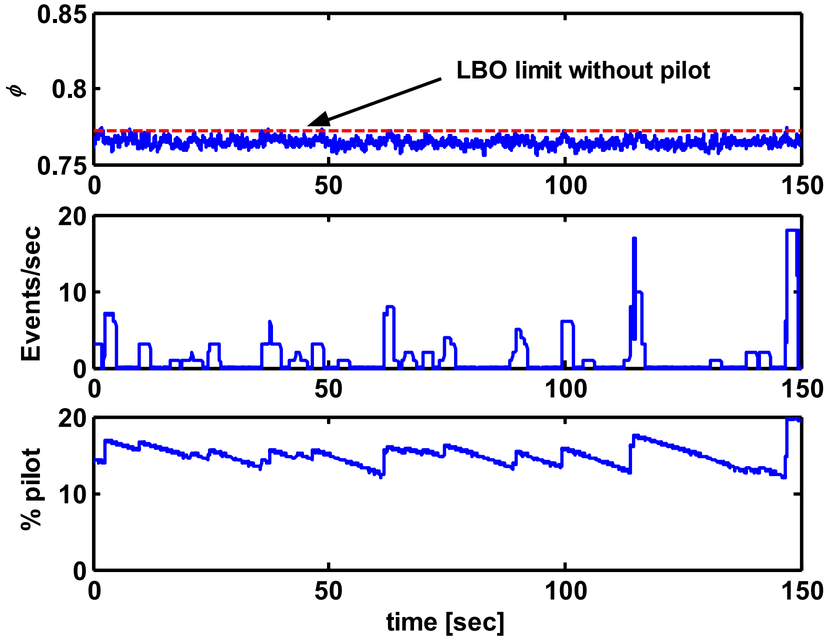

Figure 64. Response of the integrated control system to nominally stationary operating conditions.

Figure 65 shows the behavior of the closed-loop system when there are fluctuations in the operating conditions. In this case, the starting conditions were chosen such that the combustor was stable without piloting. The air flow was manually varied, with the overall equivalence ratio changed at a maximum rate of 0.03 sec^{-1}. It can be seen that the controller did not take action until the LBO limit was approached (at $t \cong 54$ s). It successfully suppressed blowout by turning on the pilot. For 60<t<100 s, when the combustor was below the unpiloted LBO limit but the air flow was essentially constant, the system operated in a nearly stationary mode. When the air was finally decreased to a point where the equivalence ratio was no longer below the unpiloted LBO limit, the controller eventually diverted all the fuel back to the main flow. The relatively slow response of the system in decreasing the pilot is due to the very conservative set of valve decrement parameters chosen.

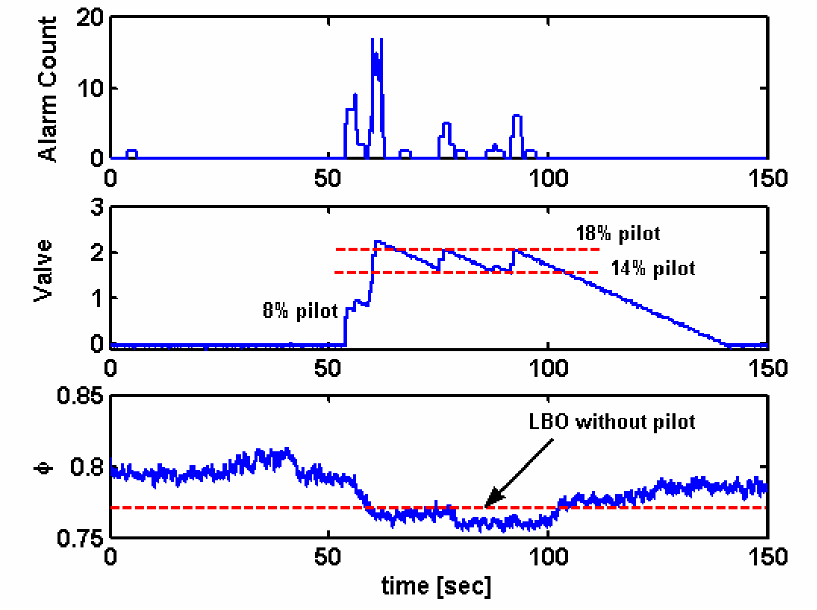

Figure 65. Response of the integrated control system to varying operating conditions.

The results presented above were obtained with constant increments for each event detected and constant decrements. However, the algorithm shown in Figure 63 is a more sophisticated control algorithm that responds proportional to the input and increases the decrement steps if no events were detected for a long time. The next experiment included the proportional decrement with the number of prior decrements, and a non-zero Y%. Thus when there are events closer together or if the events are longer, the controller increases the pilot fraction more than just X%. Figure 66 shows the response of the modified controller to the external variation of the flow conditions. The equivalence ratio was changed by changing the airflow rate, keeping the total fuel flow rate constant. The nominal LBO limit is also shown on the plot. The number of events/second observed and the pilot fraction set by the controller are also shown.

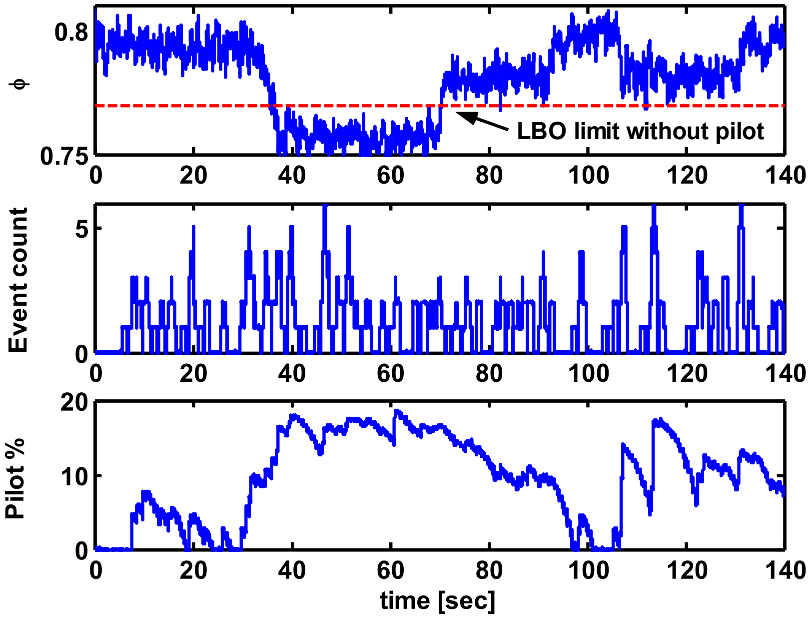

Figure 66. Response of the integrated control system to varying operating conditions.

As expected, the controller responded faster to the changes in the conditions. The number of events/sec was also maintained at a lower value by the controller. This is because the controller increases the pilot fraction by a larger amount for longer events, which indicate operation closer to LBO limit. The parabolic decrease in the pilot fraction when the combustor is safe is due to the non-constant decrements. The stationary point reached by the controller for the times 40<t<70 sec is roughly the same as that achieved by the previous control algorithm, confirming that the combustor characteristic is not affected by the controller.

5.4 Summary

This chapter demonstrated the use of the sensing methodology developed in Chapter 4. Results from total fuel control for minimizing NOx emissions were presented.

In order to develop controllers for fixed power settings, piloting was used as an alternate stabilization method. The central pre-injection pilot was found to be the most effective piloting method of the methods used. The total fuel was split into the main and the pilot flows and the pilot fuel fraction was adjusted by the controller. An event based control algorithm was used to prevent the combustor from blowoff. These experiments were performed with the controller having only the input from the blowout sensor, while the operating conditions were manually changed. The results show that the LBO sensor developed in this study can be used in conjunction with a control system to prevent the combustor from blowing off. Further control strategies with control authority over both the total fuel (or air) and the pilot fraction can be used to minimize the NOx emissions while maintaining required power output.

Chapter 6

Stabilization Processes and LBO Precursor Dynamics

In Chapter 4, extinction-reignition events were identified as precursors to combustor blowout. These events became longer and occurred more frequently as the LBO limit is approached. This behavior was similar over a wide range of flow rates. This chapter describes studies that explore the causes of these events in more detail. Various characteristics of these events that were previously observed are explained by the findings.

Section 6.1 covers background material on swirl- and dump-stabilized combustors. Section 6.2 presents the dynamics of the flow and combustion processes during the extinction phase of a precursor event. Section 6.3 discusses in detail the reignition phase of precursor events. Section 6.4 discusses the blowout events. Section 6.5 investigates the flame structure during the reignition event of a precursor. Section 6.6 describes the overall blowout phenomenon in a swirl dump stabilized combustor. Section 6.7 gives the inferences from this understanding that explain certain unexplained observations from the previous chapters.

6.1 Background on blowout of swirl dump combustor

The flow field in swirl- and dump-stabilized combustors has been studied in detail over the last two decades.[45,63] This flow field is challenging due to the interaction of swirl, vortex dynamics, turbulence, heat release, and chemical reactions. In high heat release combustors, the swirl and dump plane (sudden expansion) together cause a vortex breakdown along the combustor axis, which results in an Inner Recirculation Zone (IRZ); the dump plane also creates an outer recirculation zone (ORZ). The flame is stabilized due to heat and radical feed back from the recirculation zones.

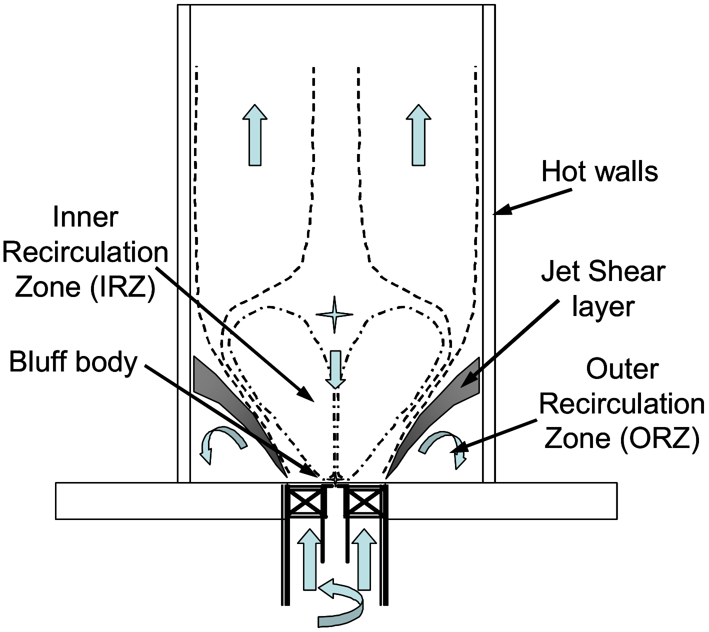

Figure 67. Schematic of flow features in the swirl dump stabilized combustor.

Figure 68 shows a typical signal from the fiber probe very close to blowout of the combustor and an expanded time trace showing three types of behavior: 'regular combustion', a 'precursor' event and a 'blowout' event. The spatial distribution of the flame associated with these different signal behaviors is presented in Figure 69, which includes frames from the high-speed chemiluminescence movie that was simultaneously recorded with the probe data. The circles in the time trace correspond to the instances when the frames were captured.

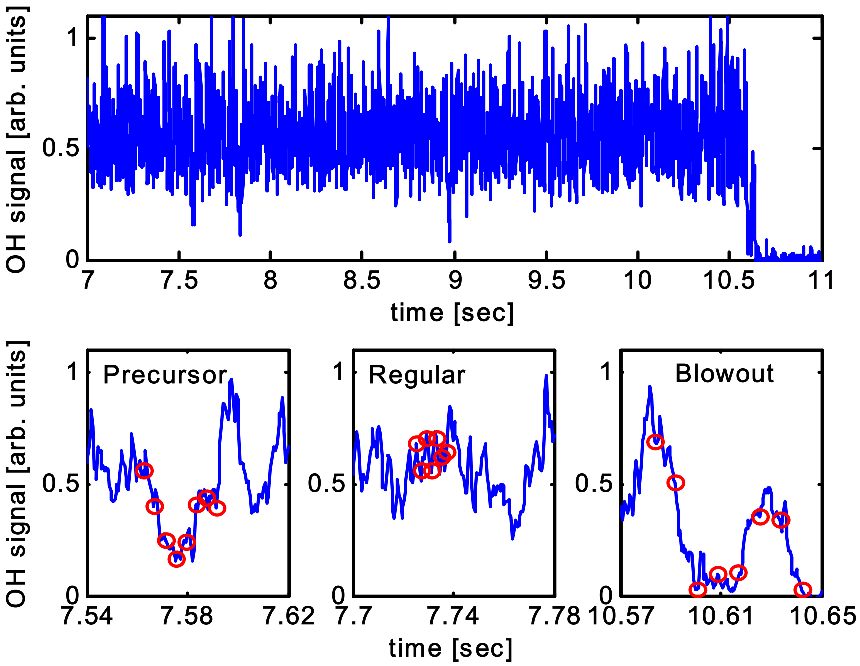

Figure 68. Chemiluminescence time series signal from the fiber near blowout. The bottom row shows the expanded data at specific instances corresponding to a precursor event, regular combustion and a blowout event. The circles on the data represent the instances of the images presented in Figure 69.

The line-of-sight averaged images show that the flame (combustion zone) typically occupies most of the length and width of the combustor during regular combustion. During a precursor event, the overall intensity (heat release) occasionally decreases for a short duration, but is soon restored. In the third sequence, the flame does not fully recover, which shortly later results in blowout of the combustor. For this blowout event, the signal level from the sensor drops and does not recover fully.

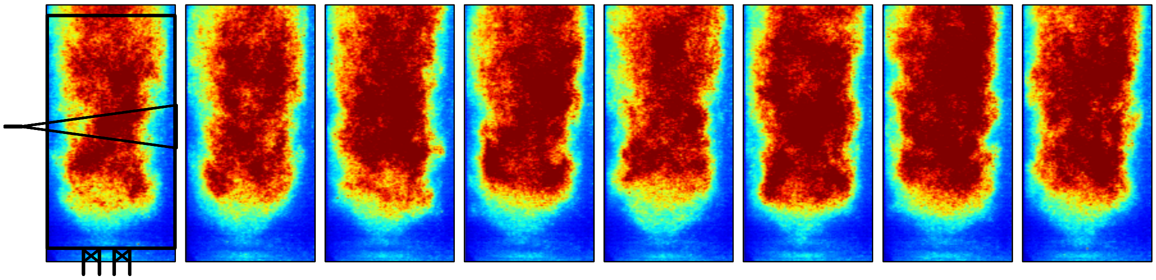

(a) Regular combustion

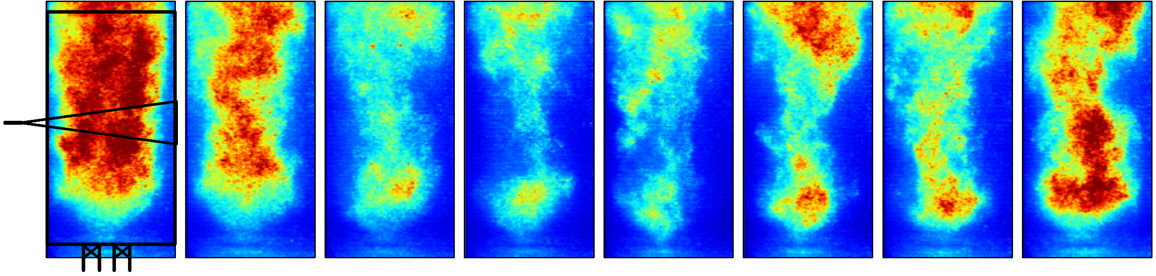

(b) Precursor event

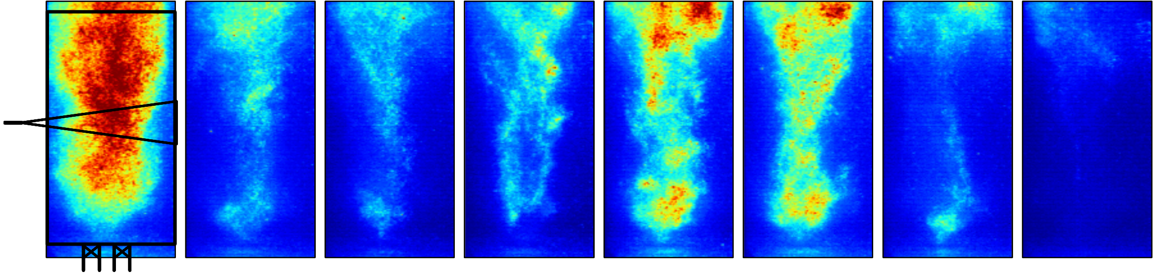

(c) Blowout

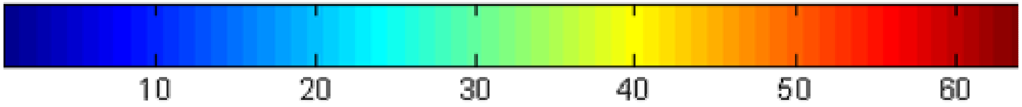

Figure 69. Chemiluminescence movie frames showing regular combustion, precursor event, and blowout event. All these frames are from the same run with constant flow conditions. The image separation for first, second and third rows are 2, 4, 8 msec respectively. The fiber collection volume and the combustor outline are superimposed on the first image in each row. The time instance of these images corresponds to the circles shown in Figure 68.

6.2 Extinction phase of the blowout precursor events

The chemiluminescence images reveal that there are large regions where there is no or little chemiluminescence intensity during a precursor event. No detectable chemiluminescence implies no chemical reactions (or a much reduced reaction rate) in those regions. Thus it can be concluded that there is no combustion occurring there. The first question to be addressed is whether these regions (without chemiluminescence) in a precursor event are filled with hot products or cold reactants.

6.2.1 Droplet scatter imaging results

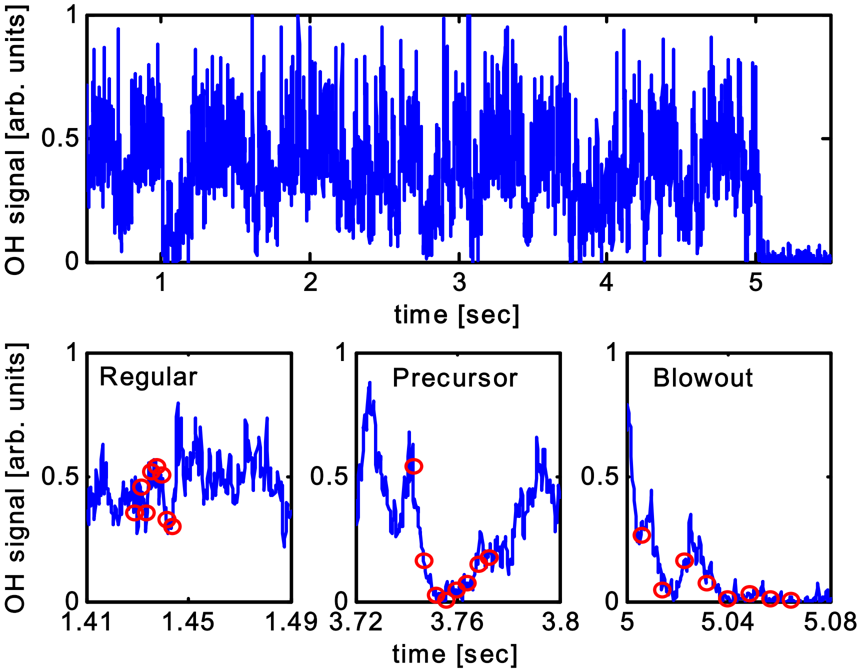

Figure 70. Chemiluminescence time series signal from the fiber near blowout. The bottom row shows the expanded data at specific instances corresponding to regular combustion, a precursor event and a blowout event. The circles on the data represent the time instances of the droplet scatter images presented in Figure 71.

The droplet scatter imaging technique was used to find the distribution of cold unburned gases in the combustor as a function of time. Simultaneous with the high speed movie, the OH chemiluminescence data was recorded from the fiber sensor. Figure 70 presents the variation of the OH chemiluminescence signal from the sensor, with expanded views for regular combustion, a precursor event, and a blowout event. The corresponding droplet scatter movie images are shown in Figure 71. The circles in the signal time traces represent the time instances that correspond to the images presented in Figure 71.

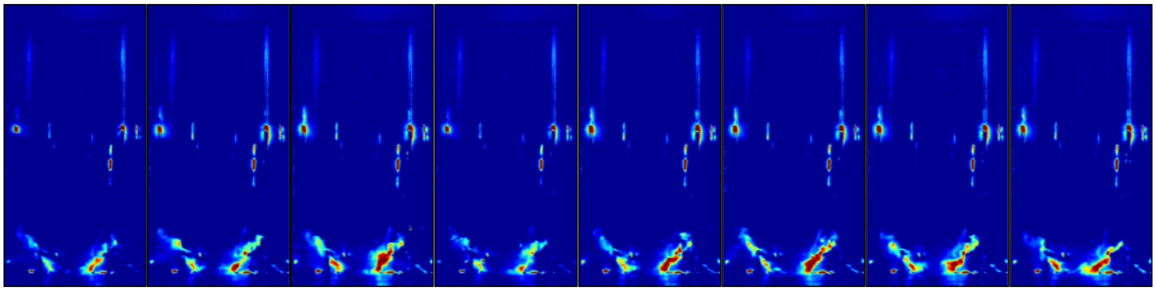

(a) Regular combustion

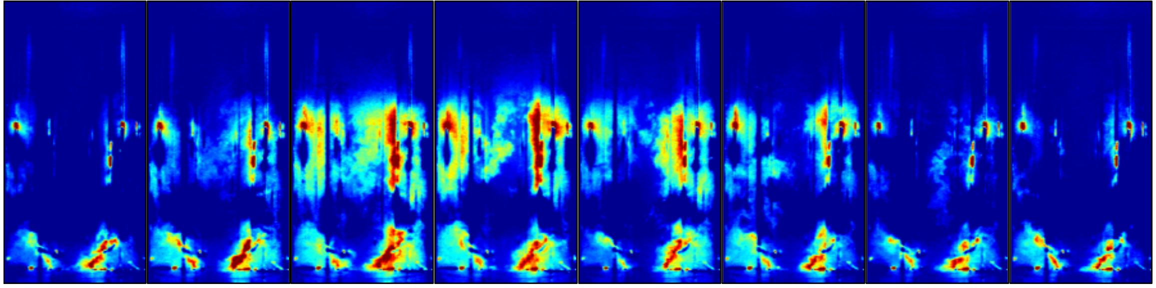

(b) Precursor event

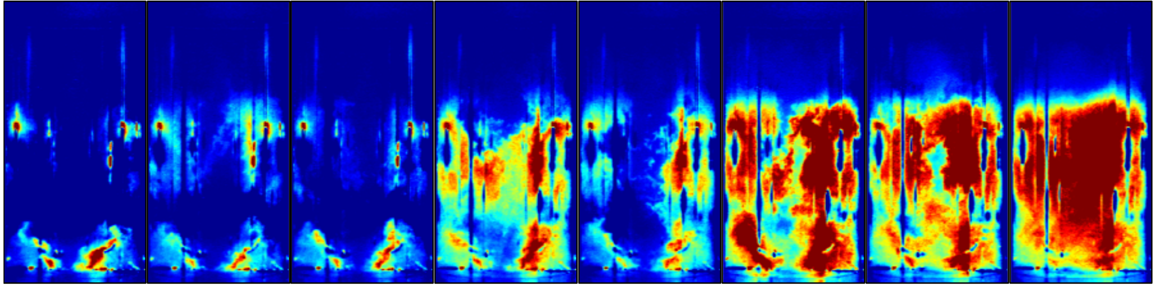

(c) Blowout event

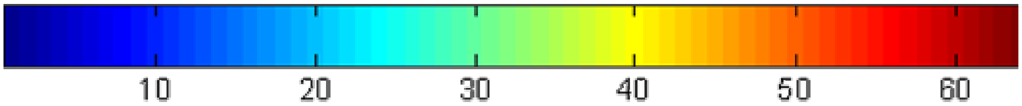

Figure 71. Droplet scatter movie frames showing regular combustion, precursor event, and blowout event. All these frames are from the same run with constant flow conditions. The image separation for first, second and third rows are ~2.1, 4.2, 8.4 msec respectively. The combustor outline is superimposed on the first image. The time instance of these images corresponds to the circles shown in Figure 70.

Figure 71 shows images of elastic laser scattering from oil droplets seeded into the reactants; the images in the figure were acquired during a precursor event. The jet of cold reactants leaving the annular swirl vanes is easily seen as the V-shaped (dark = high signal level) structure at the inlet. The ORZ, which did not have chemiluminescence, does not have droplets. This suggests that the gases in the ORZ are not pure cold reactants; rather they have mixed with some products (and are hotter), which leads to a reduction in both droplet size and number density.

During the precursor events, the seeded oil droplets fill the same region that did not have chemiluminescence; thus the gases in that region must be cold reactants. These images also reveal that cold gases fill the regions around the IRZ before the whole flame is split into two parts. During the first three images of the precursor event sequence, droplet scattering starts appearing on the circumference of the combustor at mid height. As time progresses, the droplet filled region increases in area, and the ORZ is now populated by droplets. This and the chemiluminescence images show that the cold reactant regions form first around midway up the combustor, which is the region just above the IRZ. The outline of the IRZ is clearly visible in the droplet scattering images where the cold gases wrap around the IRZ before they enter the IRZ, leading to full flame loss at mid height.

The beginning frames of the blowout sequence also indicate that cold gases first envelop the IRZ and then cut the flame shape into two parts. The extinction phases of the precursor event and the blowout event as observed from both chemiluminescence and droplet scatter imaging appear to be similar. In both cases, the IRZ is surrounded by cold reactants and the reacting zone is almost cut at the mid height of the combustor. The difference between these processes appears to be in the reignition phase.

The chemiluminescence intensity in the IRZ decreases when the precursor event starts (see Figure 70). When the cold gases are surrounding the IRZ, it is inevitable that the cold gases mix with the gases in the IRZ. Introduction of more cold reactants rather than hot products decreases the ability of the IRZ to ignite unburned packets. When the feedback from the burning packets around the IRZ decreases, the IRZ cools down and thus there is cold gas (seen as droplets) in the IRZ. Some of the frames show that there are droplets entering the IRZ from the top center. This is consistent with the prediction of Sotiropoulos[52] that the bubble type vortex breakdown exchanges fluid with its surroundings from the downstream end of the bubble. This is expected to weaken the ability of the IRZ to stabilize the combustor, and unless the perturbations that started the local extinctions cease, the IRZ will not be able to hold the flame. When this happens, the droplets start being visible inside of the IRZ, which suggests that the gas inside is cold reactants.

6.2.2 Partial extinction events

Figure 72 shows the variation of fiber sensor signal as a function of time. Also shown are the mean signal level for this run and 50% of mean level, which may be considered as a threshold for detection of precursors. There are several deviations from the mean value but only a few of them cross the threshold. This suggests that there are other deviations from the mean that are not detected by the threshold.

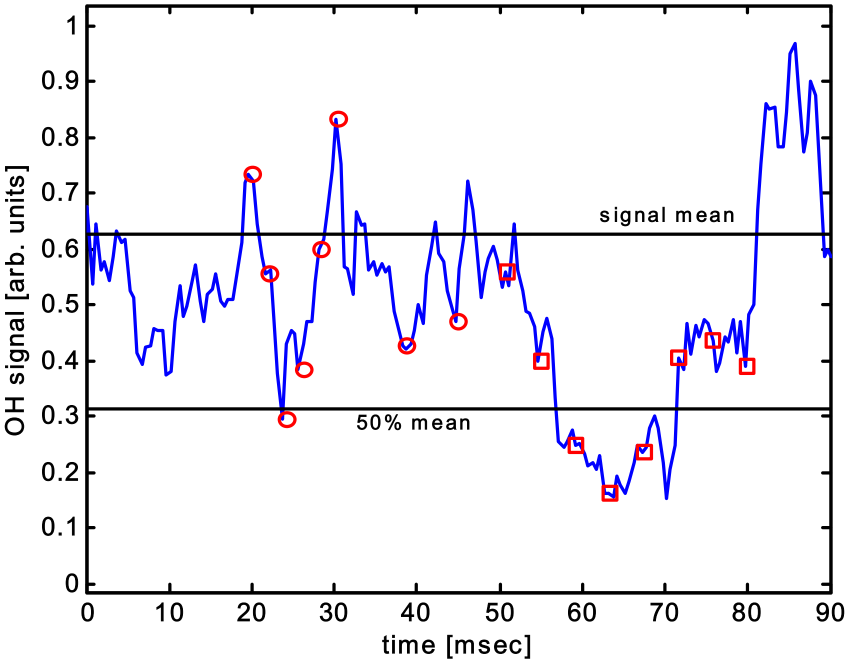

Figure 72. OH chemiluminescence data showing intensity variation prior to a precursor. The circles represent the time locations of the partial precursor images shown in fig. The squares represent the time location of precursor event images shown in Figure 73. The lines represent the level of the signal mean and 50% mean.

Figure 73 presents high speed movie images of flame distribution during the time trace shown in Figure 72. The images in the top row correspond to the circles in the time trace and the bottom row corresponds to the squares. The first six images show a decrease and increase in intensity (and thus reaction rates) in the region above the IRZ. The shape of the IRZ appears to be unchanged during this partial extinction reignition event (partial precursor event). The last two images show the flame distribution at the lowest value of the signal during two other partial precursor events (refer Figure 72).

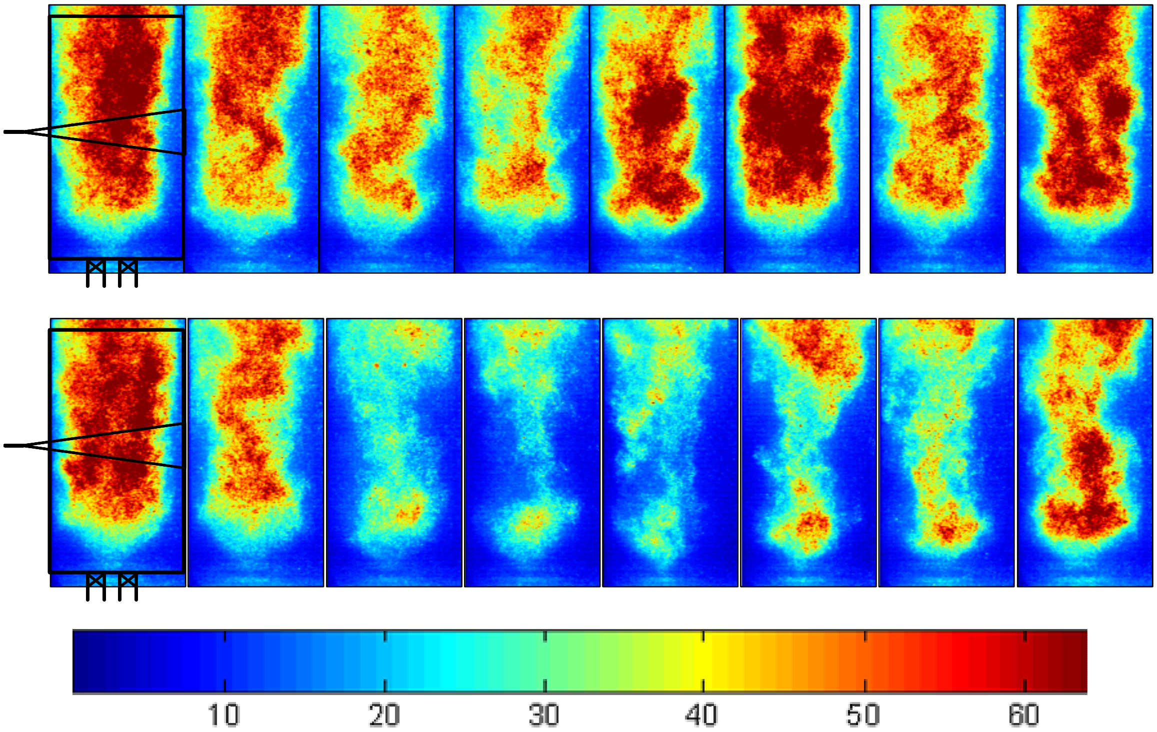

Figure 73. Chemiluminescence movie frames showing partial precursor event, two other partial precursor frames, and a precursor event. The first six images in the first row shows the sequence of images (separated by 2 msec) during a partial precursor event. The 7th and 8th image in the first row are images from two other partial flame loss events. The time locations of these frames are represented in Figure 72 as circles. The second row shows images during a precursor event. The time locations of these images are represented by squares in Figure 72.

The bottom row of Figure 73 shows the same precursor event described earlier. The flame is lost in the mid height and also the IRZ shape changes during the precursor event. The partial precursor events were found in abundance throughout the fiber data even for equivalence ratios where there were only a few precursor events identified. Moreover, there were at least two partial precursor events immediately prior to every precursor event observed. Thus precursor events appear to be an extension of these partial precursor events.

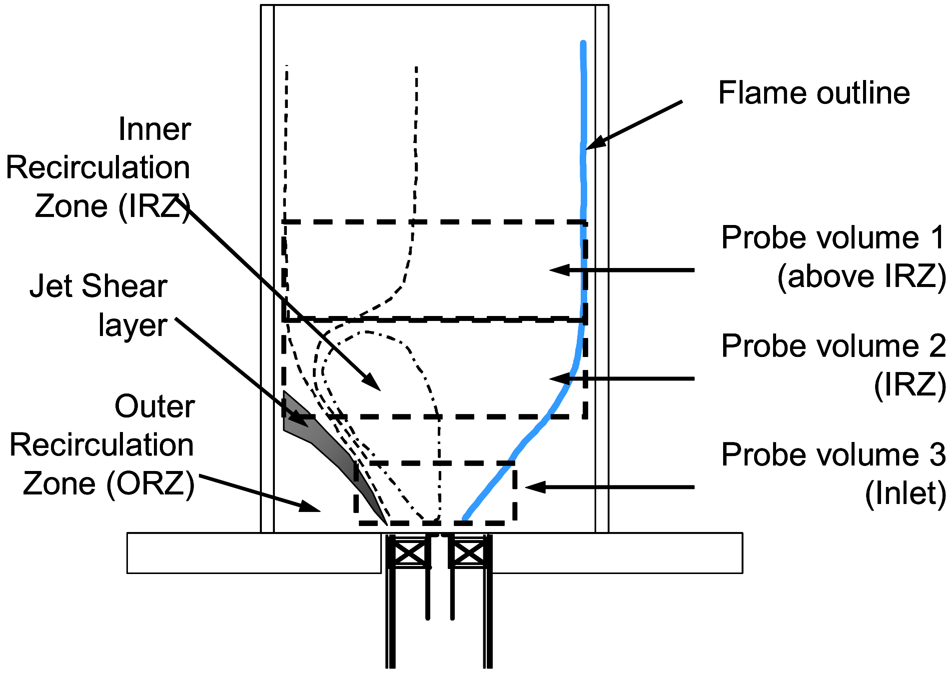

Figure 74. Illustration of the probe volumes used for integrated intensity comparisons. Also shown in figure are the stabilization mechanisms and the outline of the flame in the combustor.

To quantify the information from these images, the chemiluminescence movie frames were reduced to a set of signal traces, by spatially averaging the chemiluminescence in three different flame zones in the combustor. The flame zones are indicated in Figure 74, while Figure 75 shows the time traces of the average chemiluminescence intensities from the three zones. The time trace shows the events very close to and including blowout event. Thus partial precursor event, precursor event and blowout event are shown.

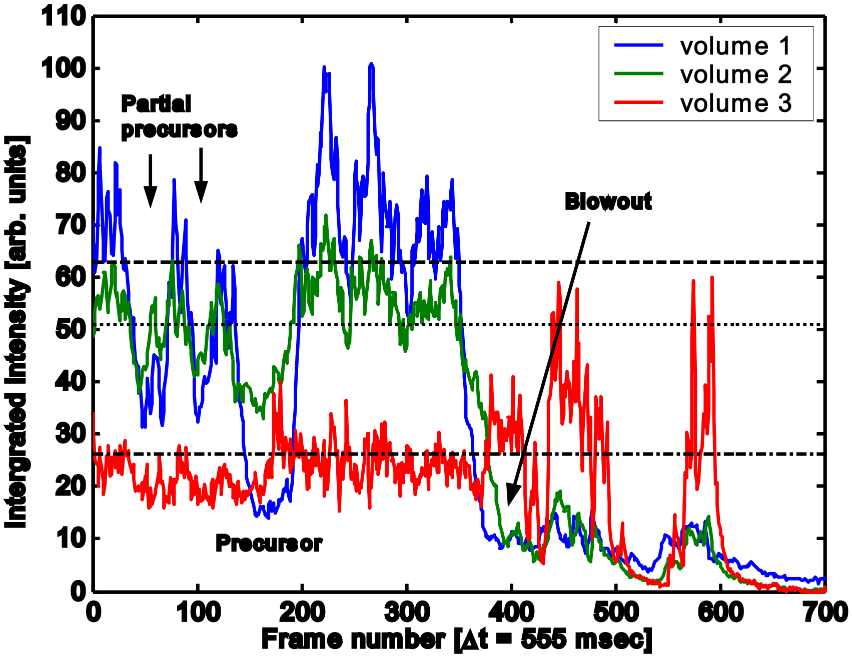

Figure 75. Frame-to-frame variation of integrated intensity values from chemiluminescence movie showing partial precursor events, precursor events and a blowout event. The horizontal lines represent the mean values for each of the integrated signals.

The intensity average for probe volume 1 was the highest while volume 2 was second. The average intensity for the whole 4 second long movie is shown as the horizontal lines. The plot shows that there were two partial precursor events prior to the precursor event. These plots suggest that the flames in the IRZ (volume 2) and the flame above (volume 1) are related; their intensity values follow each other very closely. During partial precursor, the top zone intensity drops but the IRZ flame emission is nearly constant, dropping only slightly. Based on the discussion of the bubble mode vortex breakdown in Chapter 2, we know that there are packets of hot gases leaving the bubble region (our IRZ), and it is these hot packets that most likely ignite the unburned gases that go around the IRZ. The ignited flame packets will be convected downstream of the IRZ. This explains the observation that when close to blowout, the first large scale loss of flame happens just above the IRZ. This suggests that partial precursor events are extinction events that are not strong enough to cause the IRZ to lose the flame.

In both the precursor and blowout events, the intensity in IRZ appears to decrease at a slower rate compared to the region above. Also when the intensity in volume 1 reaches its lowest, the intensity in the IRZ appears to decrease further. This is due to the cold gases surrounding the IRZ mixing with the gases inside the IRZ. The intensity from volume 3 does not appear to change significantly except during the reignition phase of the precursor event and during the blowout process.

6.3 Reignition phase of the precursor events.

Figure 76 shows the reignition phase of the same precursor event shown in chemiluminescence movie images. The lines drawn on the first seven images are to facilitate visualizing the movement of flame structures in print. The circles show the tracking of flame packets (reaction zone around hot/burning gases) as it travels upstream. The arrows show the direction of motion of the flame structure from the current frame to the next frame.

In general, the flame near the exit of the combustor travels upstream through the axis of the combustor. On closer inspection of the chemiluminescence images, it can be seen that the flame travels downwards in a double helical pattern. The lines drawn on the first few images show the two helical flame structures rotating about the axis of the combustor. The two sets of circles show the movement of the flame packets downward. When a bright flame packet reaches the inlet region, the flame zone near the inlet expands sideways as indicated by the arrows. Although not indicated with arrows, the flame packet marked by the first set of circles also expands and strengthens the bubble like flame near the inlet region.

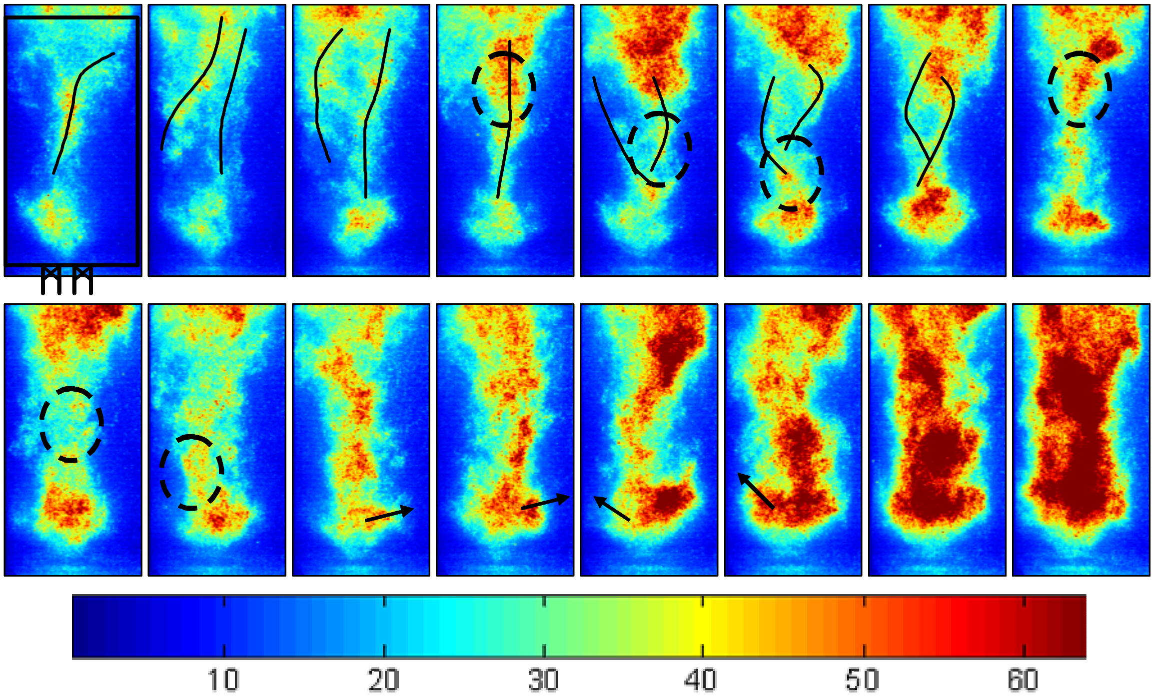

Figure 76. Chemiluminescence movie frames showing the reignition phase of a precursor event. Regular combustion, precursor event, and blowout event. The images are separated by 1 msec. Order of the images is left to right, top to bottom.

After the extinction phase, the double helical structure forms on the top half of the combustor and a set of packets of burning gases are sent downward. Each of the flame packet increases the strength of the bubble. When the flame packets are able to restore the IRZ with hot gases, the original flame is restored. When the flame packet that reaches the inlet is not "strong enough," it cools down (likely due to mixing with cold gases) and there is no change to the flame shape and the double helix pattern continues.

The structure of the flame in the first row appears as if it were enveloping the double helical structure shown in Figure 77(a) adopted from Ruith *et al.*[51] However, the movement of the flame packets is towards the inlet while the particles in Figure 77(a) are convected downstream by the flow. This inconsistency is addressed in detail in Section 6.5.2. Also, the IRZ appears to become bigger in a "rolling up" fashion similar to the formation of the bubble type vortex breakdown seen in Chapter 2 (see Figure 77(b)). It is well known that the bubble type vortex breakdown is the flow feature in stable operation of the swirl- and dump- stabilized combustor (see Section 6.1). Thus the images suggest that the bubble type structure is developing from a double helical structure.

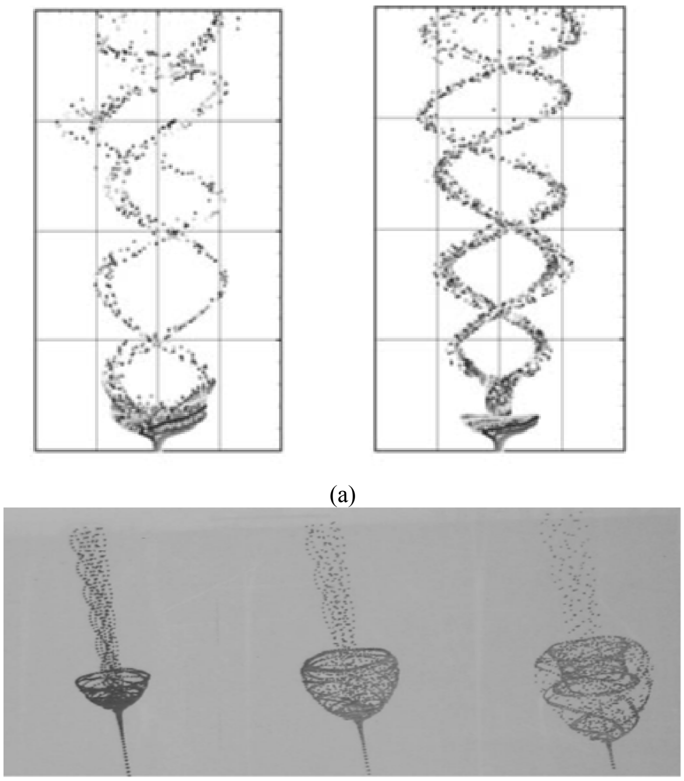
(a)

(b)

Figure 77. Images of particles in vortex breakdown: (a) The rotating double helical pattern.[51] The helical structure of the flame appears to be enveloping these helical flow features. (b) Depiction of the "rollup" during formation of bubble vortex breakdown.[57] The flame near the inlet follows similar rollup during reignition phase of precursor.

6.4 Blowout events

Figure 78 shows sequences of chemiluminescence and droplet scatter images during blowout of the combustor. The flame extinction phase appears to be the same as the precursor events, as discussed earlier. The flame structure still appears to be double helical and the flame packets can be tracked moving downward after the extinction phase. However, the flame appears to be weaker (lower chemiluminescence) than during reignition phase of a precursor event.

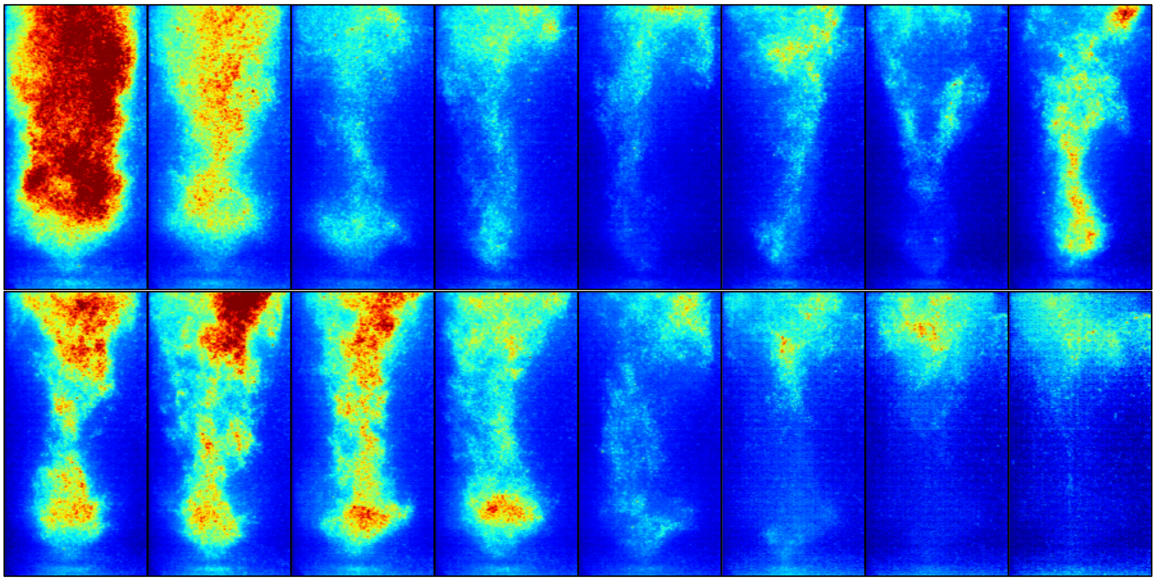

(a) Chemiluminescence imaging

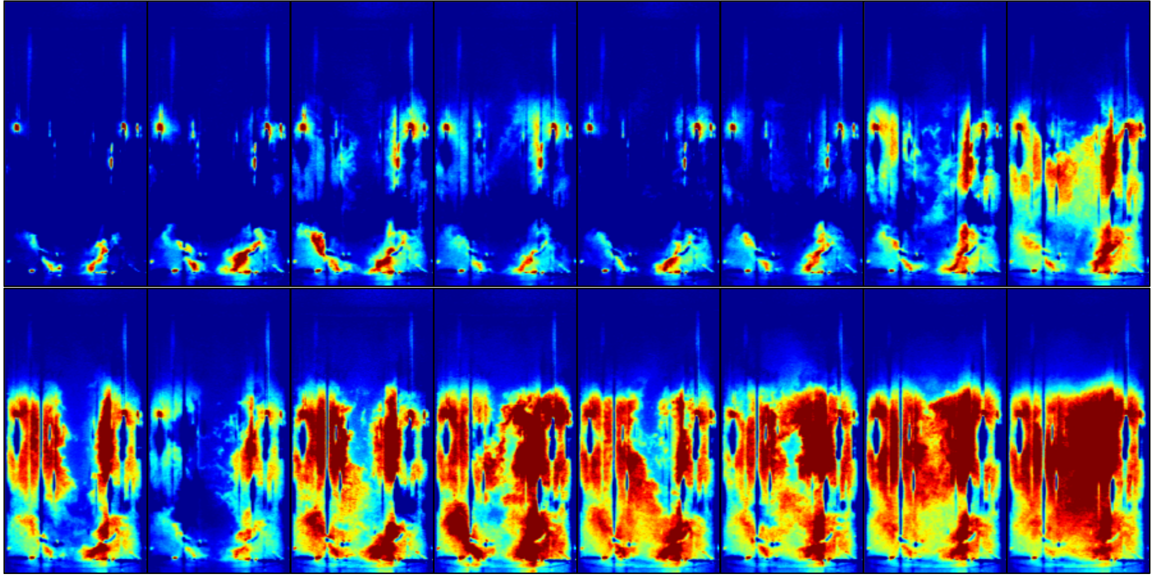

(b) Droplet scattering imaging

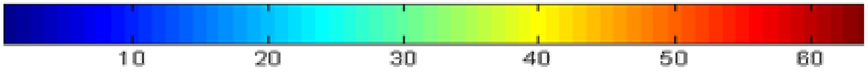

Figure 78. Sequence of chemiluminescence and droplet scattering images showing blowout events. The images in sequences are separated by 4 msec and 4.2 msec respectively.

The chemiluminescence images show that the bubble expands after a burning packet arrives at the inlet. The bubble flame, which was seen restored in a precursor, is not restored to the normal size in the blowout event. The droplet scattering images show that, as time lapses, the strength of the flame in the double helix pattern also decreases, and thus the downward flame packets are not sufficient to restore the flame, and the flame blows out.

6.5 The double helical flame

The next question to be addressed is what causes the double helical patterns and the IRZ. It is already known that there are several modes of vortex breakdown (see Chapter 2). The IRZ results from the bubble type vortex breakdown (VBD) mode in the combustor. In Section 6.3 it was shown that the flame shape during the reignition event appears similar to the streakline pattern in a double helical mode of VBD. The flame propagation in the double helical flame, however, is not consistent with double helical VBD.

6.5.1 Flame propagation speed

The chemiluminescence/droplet-scattering images indicate that hot gases move downward near the axis of the combustor. The rate of propagation of these flame packets/hot gases can be estimated from their movement between frames and the framing rate; the result is on the order of 30 m/s. Assuming u'/U=5%, u'~2.5 m/s, with a S_L=0.5 m/s, we get a u'/S_L=5. This results in S_T/S_L of 9 based on correlations.[28] The numbers used were estimated based on LDV measurements in the liquid fueled combustor discussed in Chapter 4. While this combustor does not have the counter swirl arrangement, the overall swirl number and the flow rates were similar. The average cold flow velocity in the combustor is around 5 m/s in the downstream direction. Thus the turbulent flame must be propagating against the average flow at least at a speed of 35m/s. Thus the required laminar flame speed must be ~ 4 m/s.

This value is much greater than typical flame (propagation) speeds for methane-air mixtures, as shown from Table 2, unless the mixture is preheated to above 900K. But from the droplet scatter images, it is clear that the droplets exist for several milliseconds in the center of the combustor prior to the downward propagation of hot gases, proving that the temperatures are far below 800 K (refer to Appendix A), the boiling point of olive oil. Thus the downward propagation of the chemiluminescence/flame packets must be due to negative velocities in this region of the combustor. There needs to be a negative velocity path (streamline) in the shape of a double helix that appears just after the extinction phase.

Table 2. Table of laminar flame speeds [m/s] for methane/air flame for several equivalence ratios from GRI MECH 3.0

Equivalence ratio	**Temperature of the unburnt mixture [K]**			
	298	600	900	1200
0.70	0.20	0.93	2.74	6.12
0.75	0.24	1.04	2.90	6.36
0.80	0.28	1.15	3.04	6.51

6.5.2 Negative velocity flow field

This section discusses the presence of negative velocity paths in the form of double helix during reignition events. The time average shape of the hot/reacting gases moving downward appears to be similar to the tornado flame mode (Chapter 2). But in the 120 mm long combustor used in these studies, the tornado flame mode is not stable (see Chapter 3). To understand this flame structure better, another experiment was conducted. In this case, a 190 mm long quartz tube was employed. This long tube, as shown in Chapter 3, is able to hold a tornado flame after stability is lost in the lower portion of the combustor.

Figure 79 shows the chemiluminescence movie frames of the tornado flame. Figure 79 shows frames that cover the full length of the longer quartz tube combustor. The airflow rate used was the same, but the equivalence ratio was lower than the blowout limit of the 120 mm long combustor. The movie was recorded at 1.9 kHz and 100 μsec gate time. The frames shown here are separated by roughly 1.1 milliseconds. The last (tenth) image shown is an average image averaged over 105 msec, including frames 1-9. This average image has the same structure as the photograph of the tornado flame shown in Chapter 3. The frames show that there is a stable region of combustion near the end of the combustor. The two vertical lines seen in all the images in Figure 79 at about 1/4th width from either side are reflections of stray light from the circular quartz walls of the combustor.

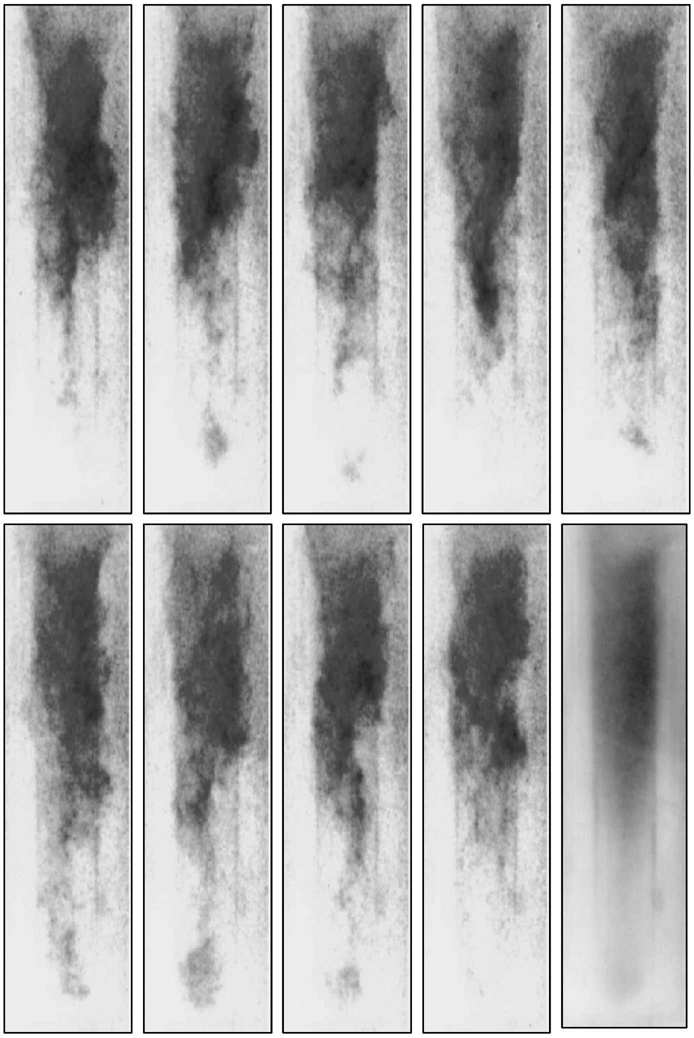

Figure 79. Sequence of (inverted grayscale) chemiluminescence images near inlet of longer combustor with equivalence ratio 0.75 (below LBO limit of short combustor). The images are separated by 1.1 msec. The time sequence of the images is from left to right. The last image is an average of frames over 105 msec.

Bradley *et al.*[45] have shown that this mode of combustion is mainly stabilized by the hot walls of the combustor. In frames 2-9, there appears to be a double helix shaped flame rotating due to the swirl. The helix can be recognized easily in frames 4-6. Frame 5 shows a projection view of the two helical structures. These helical shapes are similar to those observed in the reignition phase of the precursor event in the shorter combustor. The double helical flame structure was observed clearly only during the precursor events. Frames 5-8 show a small packet of the flame being convected towards the inlet of the combustor. These observations suggest that the recovery mechanism used by the flame during the precursor event, as seen in Section 6.3, is through this tornado type mode (which is stabilized, at least temporarily, by the hot walls of the combustor).

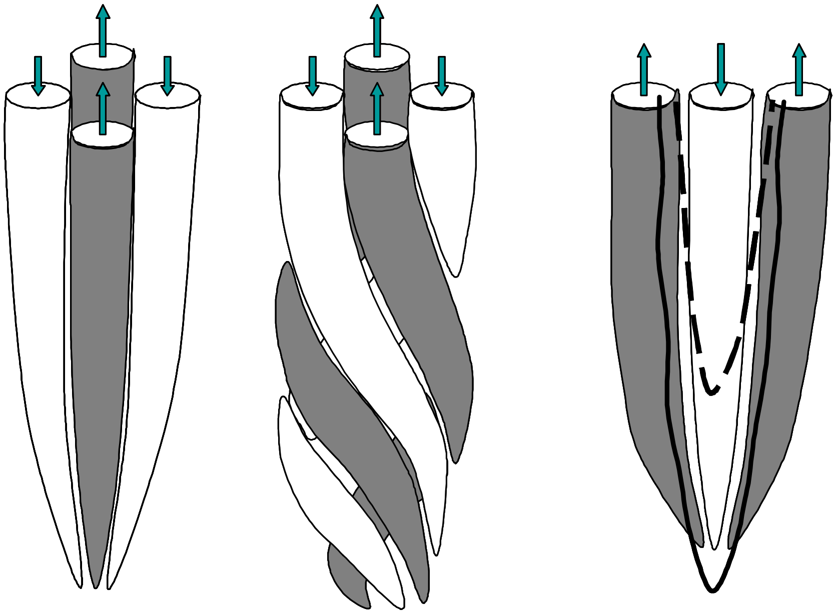

Figure 80. Illustration of flow field in the helical flame mode. (a) Two pairs of flow tubes with alternating velocity directions. The dark ones have flow going upward and the white ones have flow going downward. (b) Twisted configuration of the tubes. This structure rotating about its axis is the expected flow field in the helical VBD. (c) Illustration of flame propagation in a flow field with alternating flow directions. The white represents the hot/burning gases flowing downward and the dark flow tubes are cold reactants flowing upwards. The flame propagates as illustrated by the two curves superimposed. The helical flame mode is a twisted configuration of this flame that rotates about its axis.

Figure 80 shows an illustration of the dominant mode of the velocity field in the helical VBD. The flow field can be visualized as two pairs flow tubes with flows in alternating directions (see Figure 80(a)). This structure, when twisted about the axis, gives the instantaneous flow structure of the helical VBD. This structure rotates in time, about the axis of the flow, due to the swirl. The flow field in the helical flame is a set of helical paths with alternating upward moving cold unburned gases and downward moving hot/reacting gases. The hot gases that were convected downstream during regular combustion, now convect upstream through the negative velocity flow tubes. This can cause hot products and colder reactant gases to mix at the shear layer between these flow tubes and cause a flame.

This flame would propagate against the unburned gases in the interface between the hot and cold flows. This is illustrated in the untwisted structure in Figure 80(c). This propagation of the flame downstream into the upward flow causes a stationary structure of the flame that appears to be a fixed helical path just rotating about the axis. Disturbances in the flow field can cause lower velocities in the unburned flow that permit flame packets to reach the inlet occasionally. This explains the behavior of the tornado flame and also justifies that helical VBD occurs following the extinction phase of a precursor or a blowout event.

6.5.3 Vortex breakdown mode shift

The next issue to be addressed is the switching of the VBD modes during a precursor event. As discussed in Chapter 2, the vortex breakdown modes can switch between bubble and helical modes based on the radial redistribution of the axial momentum. Thus the current explanation reduces to explaining the transition from bubble to spiral type VBD due to decrease in the heat release rate in the IRZ. The mechanism proposed here is along similar lines of the mechanism of transition given for cold flow transition between these VBD modes (refer Chapter 2).

The hot gases in the IRZ appears as a large bluff body to the flow upstream and thus induces the flow to go around it. When the heat release decreases, the convective forces overcome the dilatation and decrease the size of the IRZ. The streamlines need not diverge as much as when there was more dilatation (heat release). This decreases the radial component of velocity, which in turn impedes the feeding of axial vorticity into circumferential vorticity that is required for bubble type VBD. Thus the bubble loses “strength” and shrinks in size. This further increases the axial component of velocity at inlet and thus forms a bootstrapping mechanism that leads in to forming the helical VBD.

The mechanism for the transition from the spiral VBD mode back to the bubble mode would be quite the opposite. When the hot gases return to a region near the inlet, the dilatation from the heat release would appear as a larger bluff body and cause the incoming streamlines to diverge. This would increase the radial velocity near the inlet and assist in redistribution of axial vorticity into circumferential vorticity. This would further decrease the axial velocity component and thus induce the streamlines to diverge more. The recirculation of the hot gases also helps increase the strength of the combustion process and increases the dilatation. Overall, this process has positive feedback and would lead to recovery of the bubble type VBD.

6.6 Description of the blowout phenomenon

This section summarizes the overall blowout process as indicated by the findings in the previous sections of this chapter. The combustor is stabilized by the bubble type vortex breakdown, which forms the IRZ. The incoming premixed gases go around the IRZ and start mixing, in a turbulent manner, with the gases from inside the IRZ. Some hot packets that leave the IRZ enter the reactant gas stream and ignite the gases. These gases now follow the streamlines around the IRZ and burn. Some of these new product gases enter the IRZ from its downstream end. Thus the IRZ has a continuous inflow and outflow of radicals and heat. The remaining reactant gases and products go past the IRZ and are convected out of the combustor. These gases will flow along the walls of the combustor as they swirl. This exchange keeps the walls hot.

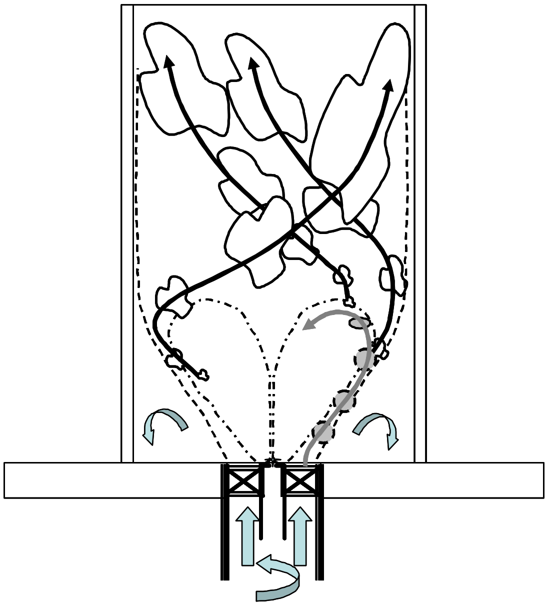

Figure 81. Illustration of the regular combustion process.

When the mixture is made leaner, the heat release decreases and thus the sustaining exchange of fresh radicals and heat is decreased. Small intermittent perturbations, possibly due to local extinctions of the flame due to high strains, cause the entrainment into the IRZ to consist of colder gases or less effective ignition sources. Thus the IRZ becomes colder and less able to ignite the surrounding reactants. Thus there may be packets of reactants just convected around the IRZ and through the exit of the combustor. This causes more cold packets to enter the IRZ and weaken it further. There comes a point in time when there are enough cold packets entering (and leaving the IRZ) that the reactants outside are no longer ignited. This forms a hole in the stream of burning gases convected downstream of the IRZ. This causes the partial precursor events described earlier.

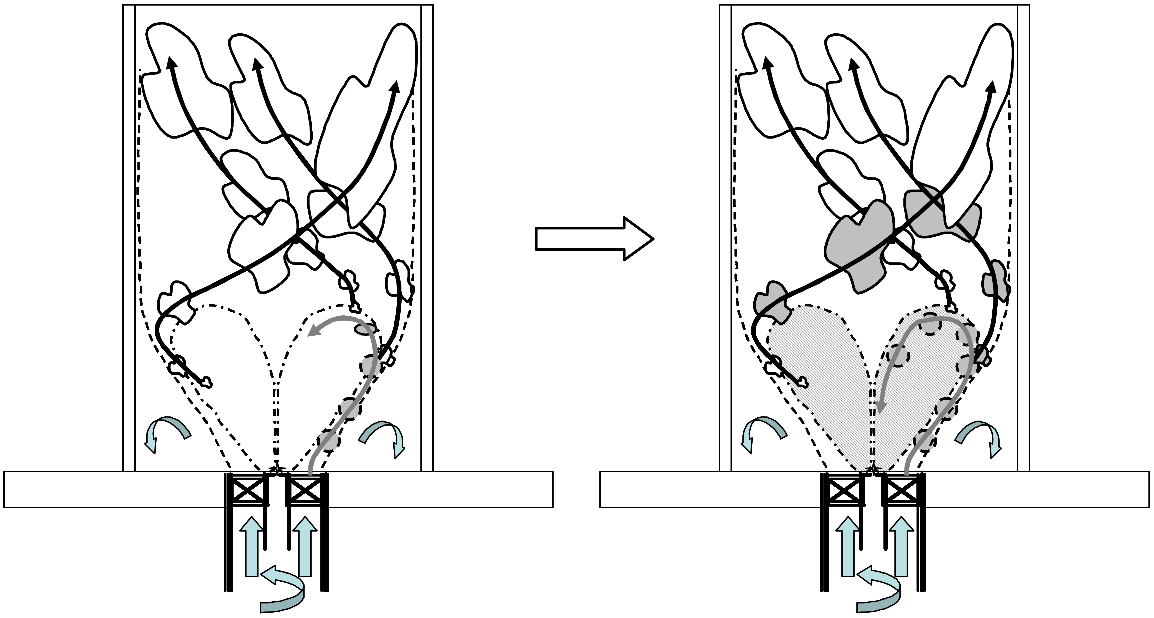

Figure 82. Illustration of a partial precursor event. The a few of the packets that leave the bubble are not burning.

The probability of local extinctions increases as the equivalence ratio is decreased and the overall flow rate is maintained. This causes the number of times the partial precursors occur to increase. This causes the IRZ to cool down more and thus most of the packets that leave the IRZ are now ineffective in igniting the outer mixtures. The IRZ is now enveloped by cold gases and the IRZ gets colder. The decrease in dilatation can cause the bubble to decrease in size. This is the extinction phase of the precursor/blowout event.

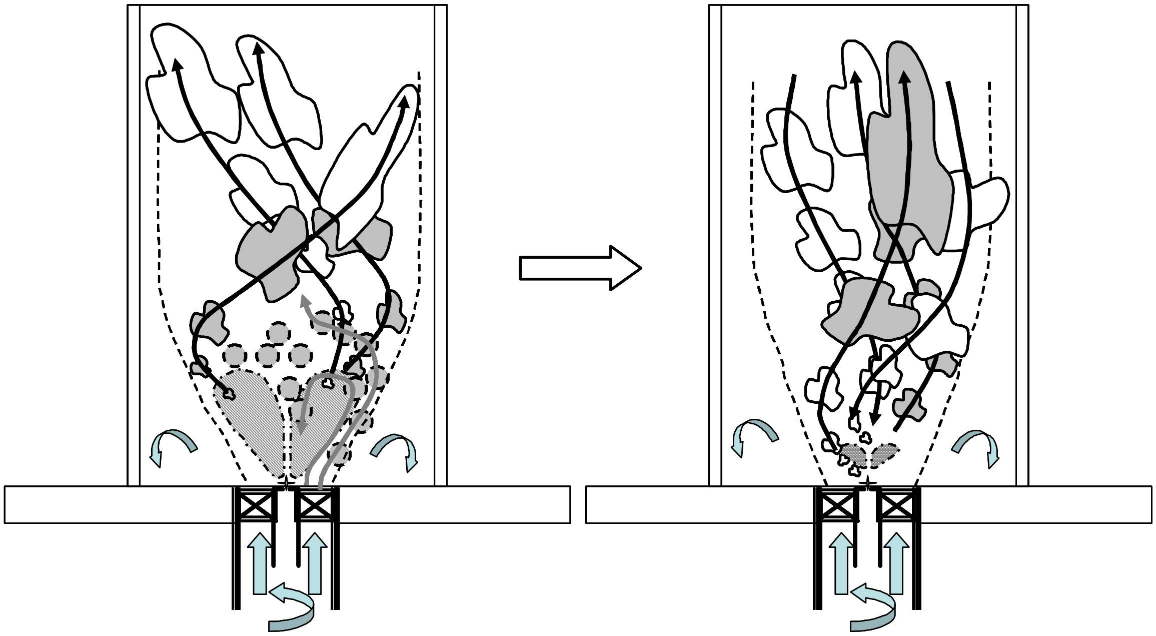

Figure 83. Illustration of the extinction phase of a precursor event. The bubble shrinks in size and becomes colder. The helical mode now has both upward and downward paths for the gases.

When the extinction phase is nearly complete, the bubble decreases in size, which decreases the redistribution of axial momentum into radial direction. The onset of bubble-to-helical type VBD mode shift occurs. This creates a path for hot gases from further downstream to return through the helical negative velocity paths. These packets could start a reaction near the inlet and cause heat release (and thus expansion) to occur. This expansion starts the positive feedback for the formation of bubble type VBD mode. This causes the IRZ to develop again, thus restoring the regular flame shape. This is the reignition phase of the precursor event.

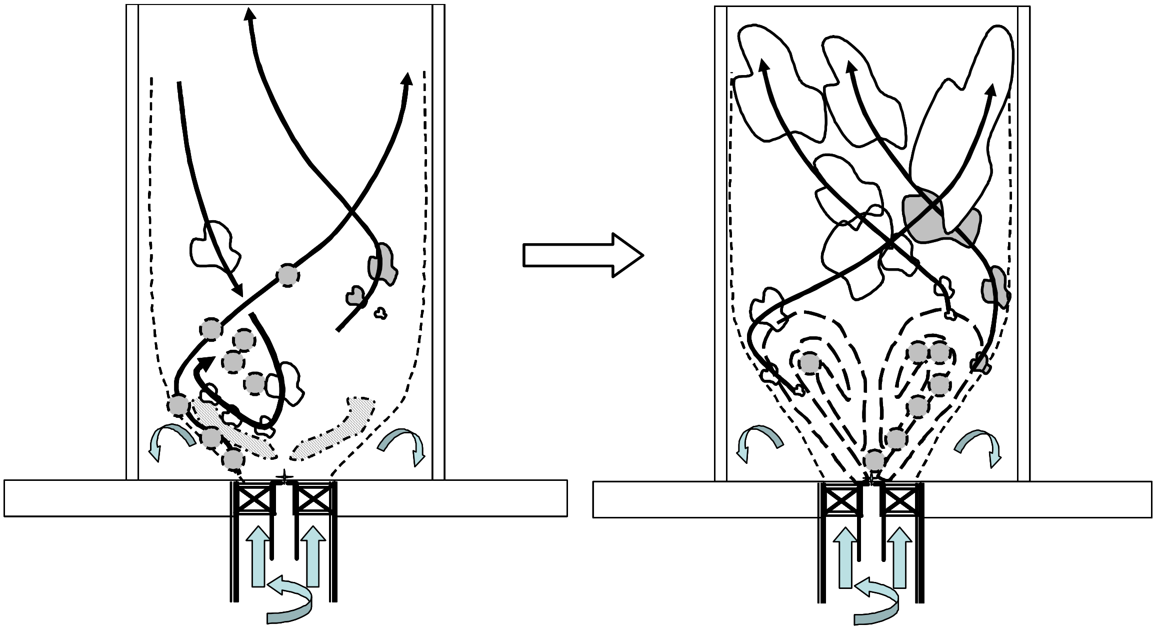

Figure 84. Illustration of the reignition phase of a precursor event. The burning gases that propagate downward cause dilatation near the inlet which causes onset of formation of bubble VBD.

The formation of bubble type VBD mode depends mainly on starting a heat release reaction near the inlet. This depends on the equivalence ratio and temperature of the incoming mixture, and the heat and radical concentration in the burnt gas packets moving upstream through the negative velocity paths. The burning packets of gas that were convected downstream during regular combustion just prior to the extinction phase may lose heat to the walls and may not be effective in igniting the mixture when convected upstream through the negative velocity paths. The walls, which were maintained at a high temperature during regular combustion, are cooling down since there are non-burning packets flowing near them. Thus after a few consecutive precursor events, the heat losses to the walls may be such that the hot gases propagating upstream do not cause sufficient heat release to instigate the transition to bubble VBD. Thus the reignition process is not completed and thus the flame never recovers, causing blowout.

6.7 Inferences

This physical model of the blowout process in this combustor explains several of the observations in the previous chapters. For instance, the effect of sensor location observed in Chapter 4 can now be explained based on the location of the probe volume for each of the sensors (Section 4.4.2). It is evident that the signal from sensor location 2 will not produce a large number of precursors as the bubble flame shrinks in size and occupies the volume close to the inlet. Probe volume 3 on the other hand, does observe most of the non-burning packets that leave the IRZ during the partial precursor events due to the swirling nature of the flow. Thus this sensor's signal is expected to have more excursions from the mean than the signal from the sensor at location 1.

Another set of observations from Section 5.2.1 were regarding the effectiveness of the piloting approaches in extending the operability of the combustor. There are two reasons for the higher efficiency of central preinjection piloting over central piloting. First, preinjection piloting increases the equivalence ratio of the fluid that wraps around the IRZ. This ensures that the packets that enter the IRZ release more heat, and thus effect the formation of the bubble VBD, which is more stable. Second, the lack of a central bluff body for the preinjection case causes the velocity profile near the axis to be more jet-like and less wake-like. Ruith *et al.*[51] have shown that jet-like profiles favor the formation of the bubble VBD over the helical mode. This also explains the reason for increased stability when part of the total air was sent through the pilot flow. However, the jet-like flow does move the bubble downstream, which might reduce the stability of the IRZ.

The transient behavior was reported to be dependent on the temperature of the walls. This suggests that the heat losses to the walls play an important role in the blowout process. In case of combustors with thermal barrier coated walls, the decreased heat transfer will affect the rate of approach of the imminent blowout. The operable regime will be extended slightly and the number of events observed will be altered. More importantly, the whole blowout phenomenon outlined by this physical model will occur as long as the combustor has a bubble type vortex breakdown during combustion.

Chapter 7

Conclusions and Recommendations for Future Work

7.1 Summary and Conclusions

The first major objective of this work was to develop a sensing methodology for determining proximity to lean blowout (LBO) of a combustor that is compatible with active avoidance control. This was accomplished by detection of LBO precursors. The second objective was to explain the dynamics of LBO and the LBO precursors in a gas-turbine type combustor. The combustor primarily used for this study was a swirl- and dump-stabilized, atmospheric pressure device, which did not exhibit dynamic combustion instabilities. The sensing methodology was also observed to be effective in predicting the approach of blowout in a liquid fueled partially premixed annular sector swirl combustor. The combustor was made to approach blowout by decreasing the fuel flow rates while maintaining constant air flow.

The first part of the thesis work concentrated on finding a sensing methodology to be able to predict the onset of approach of blowout of the combustor. Optical methods were used to monitor the combustor in this study. The sensor system was based on miniature photomultiplier tubes and fiber optics. The fiber optic system would be easy to implement in practical combustion systems as the electronics can be remotely placed and could be shielded from the harsh combustion environments. It was found that the flame shape changed temporarily prior to the actual blowout of the combustor. These temporary events were found to be composed of local extinction and reignition phases. These extinction/reignition events were found to be precursor events to the blowout of the combustor, i.e., they occurred at conditions that were close to blowout, but not where the combustor could still operate “stably” for extended periods of time.

Threshold based methods were developed to identify these events in the time-resolved sensor output. A double-threshold approach reduces noise sensitivity, and the thresholds are based on the time-localized mean signal, reducing sensitivity to power setting and degradation of the sensor or optics. The number and the average length of each event were found to increase as the LBO (fuel-air ratio) limit is approached. This behavior is used to predict the proximity to lean blowout. Three different sensor locations were investigated and the precursor characteristics were explained. The precursor events were found to exist in both gas-fueled, premixed, swirl dump combustor and liquid-fueled, partially premixed, swirl-dump stabilized, annular sector combustor. However, the exact characteristics (shape, duration, etc.) change from one combustor to another.

The second part of this study demonstrated that the sensing methodology is compatible with active control. The sensor was incorporated into a control system that monitored the approach of blowout and then actuated an alternate stabilization mechanism to stabilize the combustor near blowout. Enhanced stabilization was achieved by redirecting a part of the main fuel to a pilot injection flow, along with a fraction of the airflow. Three different pilot fuel injection methods/locations were investigated and the central preinjection pilot was found to be the most effective in stabilizing the combustor and decreasing the overall equivalence ratio for LBO. The sensing methodology, without modification, was still valid for the combustor with pilot stabilization.

An event based control algorithm for controlling the combustor from blowing out was also developed in this study. This event based controller does not require a model of the combustor or inputs about the operating conditions (flow rates etc). Two control strategies were developed: 1) Reduction of NOx emissions by reducing the total fuel until LBO limit was approached, 2) Stable operation of the combustor with low NOx emissions for a fixed power setting. The second algorithm was proven to stabilize the combustor even when the combustor loading and equivalence ratiowas rapidly changed (by changing the air flow rates).

The final part of this study focused on understanding the physical mechanisms behind the precursor events in the swirl- and dump-stabilized combustor. In this part of the study, high speed movies of flame chemiluminescence and laser sheet scattering from oil droplets seeded into the reactants were analyzed to elucidate the physical processes that cause the extinction and the reignition of the combustor during the precursor event. A theory for coupling of the fluid dynamics and combustion during precursor and blowout events is proposed. Overall, the flame is primarily stabilized by recirculation associated with a (symmetric) bubble-type vortex breakdown. The local extinctions of the flame are likely due to perturbations induced by high strain and low equivalence ratios. The vortex breakdown mode shifts from the bubble type to a spiral/helical mode.

The helical mode allows hot products to feedback from farther downstream to the combustor inlet region during the reignition phase of a precursor event. If the feedback is strong enough to cause strong dilatation near the inlet to bring about a shift of the vortex breakdown mode back to a bubble type, the flame is restored in the combustor. If not, the combustor never recovers from the extinction phase and the combustor blows out. This theory is consistent with the behavior of the combustor near blowout as observed in sensing and control experiments.

This dissertation presents the first detailed study of the unsteady dynamics that occur near blowout of a swirl dump stabilized combustor. This study is the first to provide a physical model of blowout phenomenon in swirl dump combustors and includes coupling of vortex breakdown dynamics in conjunction with combustion process near blowout. This model could also be used to select the optimum location of the optical sensor in the combustor. Further, this information could be used to develop a simplified model to simulate the acoustic radiation from the combustor during the precursor events and thus can be useful in selecting the right shape of the wavelet functions to detect the precursor events.

This physical model could now be used to model practical combustors in terms of reactor models. The recirculation zones could be modeled as stirred reactors while the flow around them as plug flow reactors, with a mixing zone feed back between them. When the IRZ temperature decreases below a certain value, the flow field can be assumed to switch to the helical mode and can be modeled by another set of plug flow reactors. This physical model could also assist in designing computational methods for simulating blowout of combustors. The model indicates that computational studies of blowout of combustors will be effective only if they can accurately capture the local flame extinctions and local heat release changes that lead to changes in the vortex breakdown mode.

This physical model of blowout phenomenon, along with the sensing and control strategies developed in this study could enable design of combustors with wider operability regimes. This could have significant payoffs in terms of reduction in NOx emissions from the combustor. One could also predict the length of the combustor for which there is a possibility of the return flow of hot gases to reignite the combustor after extinction. The physical model can also be used to predict the maximum time available for the control actuation to respond to a precursor event. It can also predict the maximum rate of change in the conditions allowed for safe transients.

This dissertation investigated only atmospheric pressure, single swirl, premixed gas combustor with no dynamic instability. However, practical gas turbine combustors operate at higher pressures, have dynamic instabilities that can drive the combustor near blowout temporarily, have counter- or co-swirl configurations and can be partially premixed. This work assumes that the main stabilization mechanism is the inner recirculation zone and thus the flame is similar to the V-shaped flame in this dissertation. Combustors with other stabilizations may have other dynamics of blowout although a similar bifurcation-like dynamics could be expected.

The Reynolds number (Re) of the combustor used in this work is on the order of 40000. Practical combustors operate at higher pressures. The velocities at the inlet may be of the same order or higher than that in this work. The characteristic length near inlet may be of the same order or relatively higher in certain combustor configurations. The temperature and the viscosity are comparable. Thus the Re in practical combustors may be expected to be higher than that used in this work. Higher Re usually produces helical breakdown and combustor designs usually ensure bubble breakdown during normal combustion. Thus all practical swirl combustors can be expected to have bubble breakdown during combustion and helical breakdown in cold flow. Thus most practical combustors are expected to behave similar to the physical model developed in this study.

In the case of a can-annular combustor arrangement in a practical gas turbine engine, all these dynamics are applicable directly. However, in the case of an annular combustor arrangement where there are no separations between adjacent injectors, the heat transfer to the walls is decreased. The decreased heat transfer will affect the rate of approach of the imminent blowout. Thus the behavior of the number of precursor events with equivalence ratio will be altered. However, the flow field can be expected to be similar to that in the combustor studied in this dissertation. In case of counter swirl injection of air, the flow field may be more complex and may depend on the swirl distribution. Nevertheless, the local flow field near a burner head can be expected to be similar to the one in this work. Thus the physical model developed here is applicable locally in each of the burner heads.

An additional issue to be addressed in the multiple burner design is the effect of precursor event from one burner on the neighboring burner. Loss of dilatation in one burner results in less constriction on the flow fields of adjacent combustors. This can allow for stronger bubble breakdown mode in the adjacent burners making them more resilient to flow perturbations. The flame/hot gases from the neighboring flames can help restore the combustion through the helical mode. The neighboring flames can act as additional heat sources for this combustor and thus can help stabilize the flame. However, if the adjacent combustor acts as a heat source for a burner, the heat losses may cause flame loss in the adjacent burner. Thus there might be a cyclic propagation of precursor event in an annular array of burners.

In case of liquid fueled combustor, during regular combustion the liquid fuel is evaporated very quickly due to the hot gases in the IRZ near the inlet. However, during a precursor event, the droplets may not evaporate and thus may stay as liquid for longer time and may even absorb the heat from the hot gases that are brought back upstream through the helical flow structures. This may result in an ineffective reignition phase and thus result in earlier blowout of the combustor. Thus non-premixed liquid fueled combustors may have different dynamics near blowout than premixed systems. Gas fueled systems can be expected to have relatively faster mixing and will follow the physical model presented in this dissertation.

The placement of sensor in these cases is not very critical and can be placed in such a way as to collect light from several combustors together, and thus can detect large scale flame losses. Thus there is no need to have one sensor per injector. There can be a grid of sensor collection lines of sight such that all the combustors are covered by four or five sensors. In case of precursor event propagation from one burner to another, sensors can be placed at lesser number of the combustors.

7.2 Recommendations for Future Studies

The sensor methodology and control system development is at its primitive stage, since the objective of this thesis work was to explore the possibility of a control system that detects and avoids blowout of a combustor. Improvements in the sensing methodology can be made in terms of finding a better method for isolation of the precursor from the noise in the signal. The analysis method used here does not exploit all the information that is present in the signal time trace. Future studies should explore other parameters, like the deviation of the signal from the mean during each precursor event, the shape of the curve, and whether there are multiple events in close succession (clustering). One can also explore if the occurrence of a precursor event is affected by the preceding precursor events. Future studies should also consider the behavior of the sequencing of the events in time and how it changes as the LBO limit is approached. If there is a relation between the clustering of the events and the proximity to LBO limit, then that information can also be used to estimate proximity to blowout. Understanding the temporal behavior of the clusters can also provide knowledge of the time available for effective actuation, which will help design effective active control systems that avoid blowout.

Finally this sensing methodology is yet to be used in a practical, industrial scale combustor. The installation of the sensor fiber optic collection must be customized for the specific combustor. Also the placement of the sensor depends on the flow field in the combustor and that might pose some challenge during choosing the placement of the fiber. The engineering difficulties of installing the sensor in a harsh environment were not explored in this work. However, there are studies in literature that involve fiber optic probe for optical diagnostics in industrial combustors.[80]

The alternate stabilization method for actuation employed here is combustor specific and thus needs further investigation in terms of what aspects of the central preinjection pilot helped the recovery of the flame, even when the overall equivalence ratio was lower. This will lead to understanding the relative strengths of each of the stabilization mechanisms present in the combustor.

The control system developed in this work was primarily a proof of concept system and thus is open for improvements. The strategy of using actuation based on each event as opposed to when the event count exceeds a certain value can be improved if the temporal behavior of the precursors is understood better. The controller could also be made self learning in a new combustor based on neural network based concepts.

An improved understanding of the dynamics of vortex breakdown and the time constants for the mode shifts would help provide estimates for the expected duration of precursor events. This information would be helpful to improve the sensing by providing another means of noise rejection. Understanding of the bifurcation dynamics of this phenomenon could also result in a model based approach to sensing the proximity to blowout limit.

The blowout of the 120 mm long combustor was explored in detail in this study and it was stated that the 200 mm long combustor does not blowout at the same equivalence ratio as the 'tornado' flame is stable in the longer combustor. Future work could explore the behavior of this flame as it blows out at lower equivalence ratios. The study will also throw light on whether the all the flames have some kind of precursor phenomena before loss of static stability, or if there are some exceptions.

The combustors investigated in this study did not have dynamic instability. Dynamic coupling of pressure and heat release can cause violent fluctuations in reaction rates and can cause the combustor to blowout. The vortex breakdown dynamics is now coupled with large scale pressure and velocity fluctuations which may result in new dynamical behavior of the combustor. Future works can study the effect of dynamic instability on blowout detection.

The physical model of blowout is based on the notion that turbulent flames, when very close to blowout, have several local extinctions and partial combusted packets. The understanding of this process is still in primitive stages and should be explored further. For instance, there are some studies that suggest local extinctions of simple flames depend on the time history of strain rate experienced at that point. Future work may involve exploring the applicability of this idea to turbulent flames, probably starting with a simple turbulent jet flame. Optical diagnostic methods like PLIF and CARS can be used to study the instantaneous reaction zone position. This in conjunction with PIV can lead to understanding the dependency of the reaction zone extinctions and the strain rate time history.

The dynamical behavior of the combustor could be modeled by simple, lumped element models based on the understanding of the physics from this dissertation. This approach would give simple mathematical expressions governing the temporal distribution of the precursor events. The stable and the unstable states of the flame could be considered as two different limit point solutions to the governing equations at different parameter (probably equivalence ratio or velocity) settings. The perturbations to this system can be modeled as a Poisson process. The distribution of perturbations in the flow parameter and the distribution of the magnitude of disturbances can also be a control parameter in this analysis. This study can lead to understanding of how the disturbance distribution affects the number of events curve, or the durations as a function of equivalence ratio. This will eventually direct better design of the combustors with desired turbulent fluctuation distributions for better operability.

Appendix A

Droplet evaporation and Mie scatter calculations

The olive oil droplet Mie scatter flow visualization experiments used tiny droplets seeded with the premixed reactants and were used to mark the cold gases. This section is devoted to justifying the idea that the oil droplet imaging can be used to identify the presence of cold reactant packets in the combustion flow field.

When a liquid droplet moves through a constant temperature field the heat conduction to its surface will heat the liquid and if the temperatures are sufficient, the liquid in the surface can evaporate. If the conditions persist for a long enough time, a droplet can evaporate fully. The intensity of the scattered light is proportional to the surface area of the droplet. Thus the intensity of the scattered light from a droplet will decrease as it moves through the flame.

$$\begin{aligned} &D^2(t) = D_o^2 - Kt, \\ &\mathit{where} \\ &K = \frac{8k_g}{\rho_l C_{p,g}} \ln\left(B_q + 1\right) \\ &B_q = \frac{C_{p,g}\left(T_\infty - T_{boil}\right)}{h_{fg}} \end{aligned} \qquad \text{Equation 1}$$

The diameter of the droplet changes in time according to Equation 1. The variable T_∞ corresponds to the temperature of the gas surrounding the droplet. D is the diameter of the droplet at time 't' and D_o is the initial droplet diameter. The other constants corresponding to the expression are listed with their relevant values, in Table 3.

Table 3 List of properties used in the droplet evaporation calculations

Variable	Description	**Value**
ρ_l	Density of olive oil	**918 kg/m^3**
C_{pg}	Specific heat of olive oil	**3000 J/(kgK)**
h_{fg}	Heat of vaporization of olive oil	**1500 kJ/kg**
k_g	Thermal conductivity of gas near droplet surface	**0.0962 W/(mK)**
T_{boil}	**Boiling point of olive oil**	**572 K**

The droplets exiting of the droplet generator are expected to have a distribution of particles of several sizes, with 2 micron droplet being the most in number.[76] A Chi-square distribution assumed with total of 1000 droplets in an observation volume of fluid moving through the flame (see Figure 85). The conceptual experiment conducted here is to observe a fluid volume seeded with the droplets that convects through the flame based on local velocities, with 1 microsecond steps in time. The temperature profile of the flame is assumed to be a linear profile from unburned to burned gases. The flame thickness is assumed to be 1 mm. A flame fixed reference frame is used in this analysis. The unburned gases move towards the flame with the flame speed. The local velocities were calculated based on a linear relationship with the assumed temperature profile.

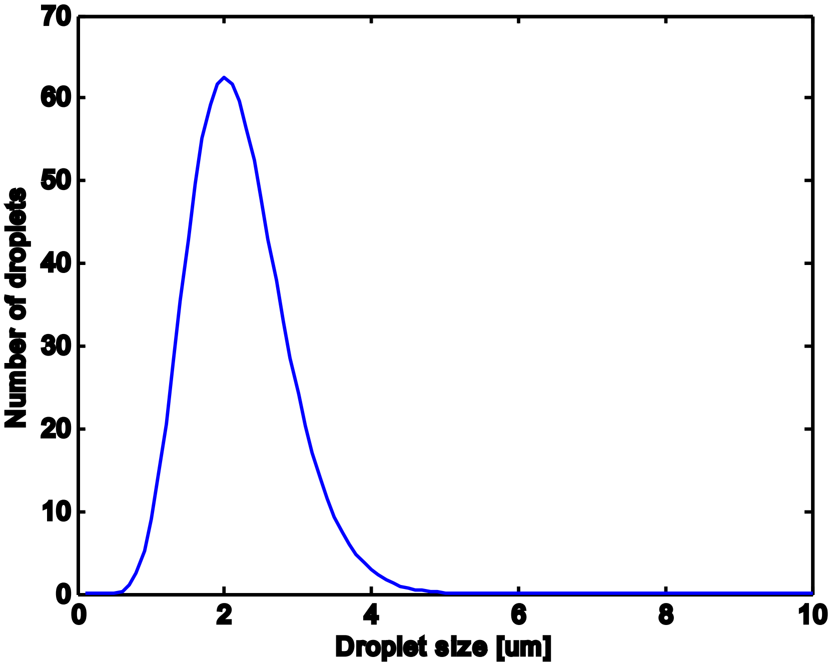

Figure 85. Initial droplet distribution assumed in these calculations.

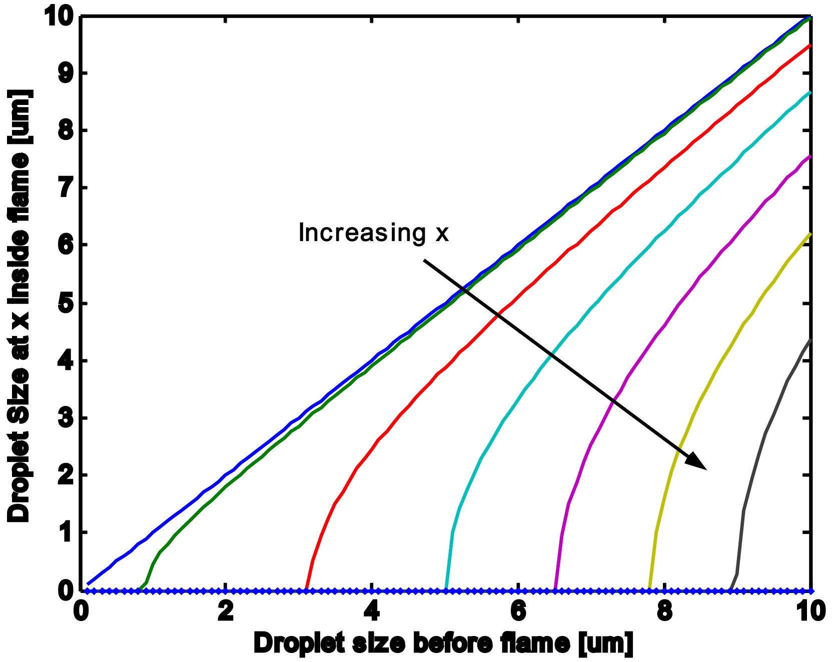

Figure 86. Variation of droplet diameter (in microns) as a function of the initial droplet diameter for various distances through the flame, x. The curves shown are for a step in x of 0.1 mm, with the first curve at x = 0.1 mm.

Each droplet is assumed to be evaporating independent of the other droplets. The use of the D-square law for this calculation assumes that these droplets do not interact with each other. Figure 86 shows the diameter of the droplets with various initial sizes, as the observed volume moves through the flame. The very first curve gives the same values as the initial sizes as that is the location of x = 0.1 mm through the flame, where the temperature is not yet above the boiling point of olive oil. The successive curves are each 0.1 mm downstream of the previous curves. It can be seen that the small droplets are evaporating at an earlier location and the larger droplets are decreasing in size as x increases.

This causes the number of large droplets to decrease while the number of smaller droplets increases. Figure 87 shows the distribution of droplets as the fluid volume moves through the flame. The general shape appears to be similar and the curve shifts parallel to itself towards the lower diameters. This behavior might be different in a real flow where the droplets may coalesce or break up and change the distribution of the droplets. The effect of droplet interactions and break up are neglected in this analysis. The first two locations have the same droplet distribution since the temperature is not higher than the boiling point of olive oil. There is a rapid change in the droplet distribution at x = 0.2 mm. At x = 0.3 mm, almost all the droplets present are less than 1 micron in size. At x = 0.4 mm there are no droplets present in the fluid volume.

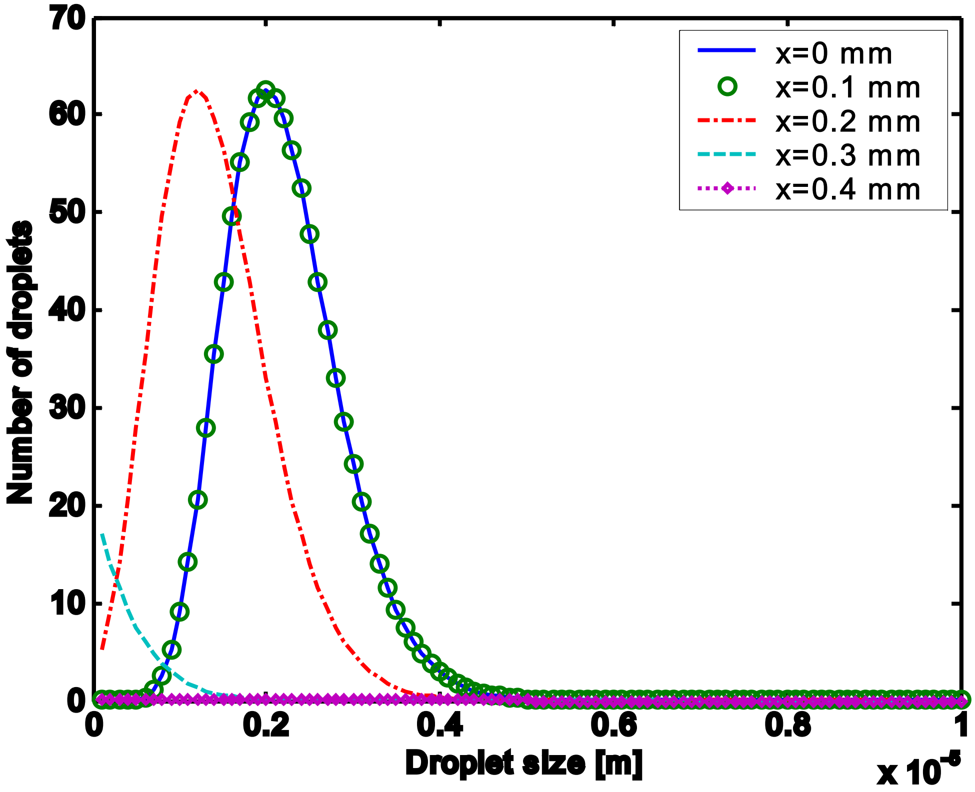

Figure 87. Distribution of droplets at various x locations. Droplets with sizes above 1 micron cease to exist past 0.3 mm.

The variation of intensity of the Mie scattering will result from the change in diameter of the droplets. The change in refractive index due to change in temperature of the droplets is not considered in this analysis. Holding other parameters (like laser intensity, sheet thickness, collection volume, etc.) constant, the Mie scattering intensity changes as the total surface area of the droplets. For droplet diameters of the order of 1 micron, the scattering from the droplets is not a pure Mie scattering (intensity proportional to square of diameter) or Rayleigh scattering (intensity proportional to fourth power of diameter) but a transition between them. In this analysis the sum of squares of diameter for all the droplets is used as a representative value for the intensity as this will give the worst case estimate of the loss of intensity from scattering. Figure 88 shows the variation of intensity as a function of the distance through the flame for three different flame speeds. Also shown in the figure is the temperature profile used in this study. The temperatures correspond to combustion of room temperature methane/air premixed mixture at equivalence ratio of 0.75. The low equivalence ratio is used for all the cases shown here, as this will result in over predicting the penetration depth of the droplets through the temperature gradient. The three flame speed values used were 30, 60 and 90 cm/s. The first two flame speeds are realistic in strained premixed methane air flames at equivalence ratio of 0.8.[70] Although 90 cm/s is higher than realistic values, it is used to give a worst case estimate of droplet penetration through the flame. The results in Figure 86 and Figure 87 correspond to a flame speed of 30 cm/s.

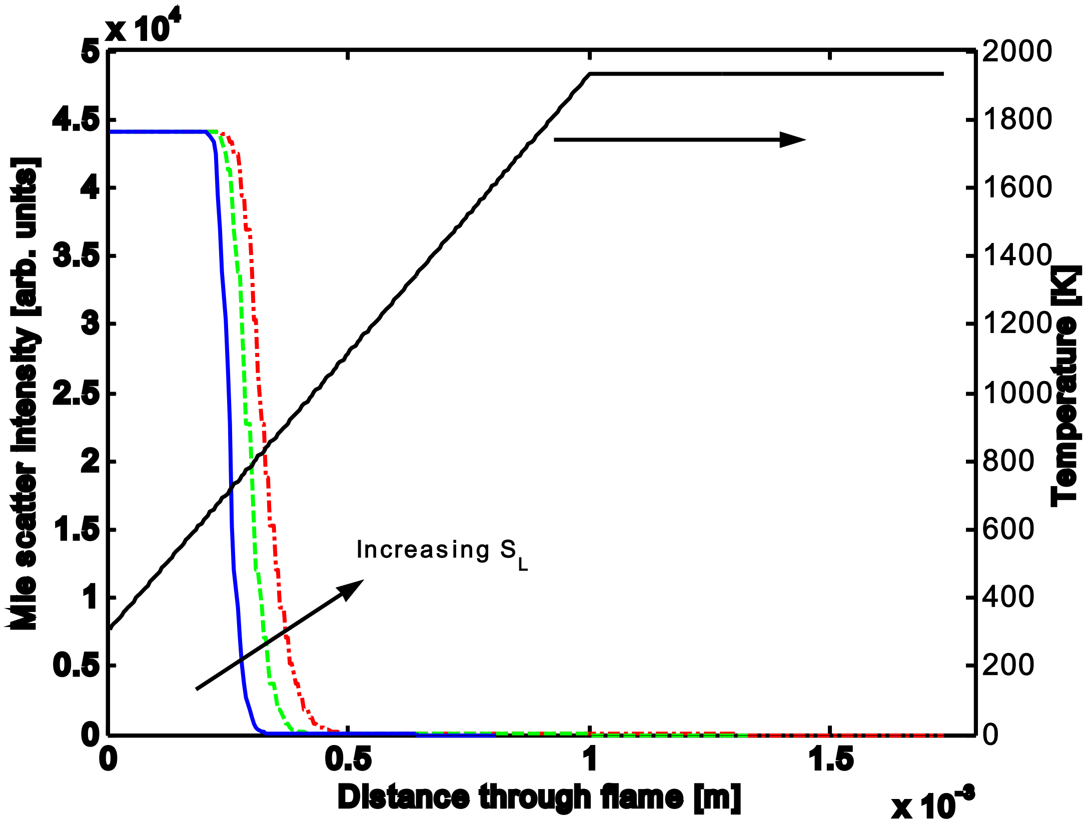

Figure 88. Variation of Mie scattering intensity as a function of distance traveled through the flame zone. The three curves correspond to flame speeds of 30, 60 and 90 cm/s. The temperature profile used for the flame is also shown.

Mie scattering intensity values decrease to 10% of their initial values when the droplets have reached a temperature of 750, 850 and 930 K respectively for the flame speeds of 30, 60 and 90 cm/s. This suggests that there will be very little scattering signal captured in the camera, when the temperature of the droplets become higher than around 800 K. The turbulent flow field may impose a different temperature history on the droplets compared to that used in this simple analysis. Nevertheless, this analysis points out that if there is scattering intensity from a region of the combustor, those droplets could not have gone through a hotter temperature history than that experienced by the droplets in this analysis. This justifies the usage of droplet scattering imaging to identify the regions of cold reactants.

References

1 Bowman, C.T., "Control of combustion-generated nitrogen oxide emissions: Technology driven by regulation", Proc. Comb. Inst., Vol. 24, 1992, pp 859-878.

2 Correa, S.M., "A Review of NOX Formation under Gas-Turbine Combustion Conditions", *Combustion Science and Technology,* Vol.87, 1993, pp.329-362.

3 Turns, S.R., "An introduction to combustion: Concepts and applications", 2nd ed., McGraw-Hill publications, 2000.

4 Correa, S.M., "Power Generation and Aeropropulsion Gas Turbines: From Combustion Science to Combustion Technology", *Proc. Comb. Inst.,* Vol. 27, 1998, pp. 1793-1807.

5 Lefebvre, A. H., "Gas Turbine Combustion", Taylor & Francis publishers, Philadelphia, 1998.

6 Mongia, H.C., "Aero-Thermal Design and Analysis of Gas Turbine Combustion Systems: Current Status and Future Direction," *AIAA Paper* 98-3982, 1998.

7 Tacina, R., Mao, C. P., and Wey, C., "Experimental Investigation of a Multiplex Fuel Injector Module for Low Emission Combustors", paper no. AIAA 2003-0827, 41st AIAA Aerospace Sciences Meeting, Reno, NV, Jan 6-9, 2003.

8 Richards, G. A., McMillian, M. M., Gemmen, R. S., Rogers, W. A., and Cully, S. R., "Issues for Low-Emission, Fuel-Flexible Power Systems", *Progress in Energy and Combustion Science,* Vol. 27, 2001, pp. 141-169.

9 Ducruix, S., Schuller, T., Durox, D., and Candel, S. M., "Combustion dynamics and instabilities: Elementary coupling and driving mechanisms", *Journal of Propulsion and Power*, Vol. 19, No. 5, 2003, pp. 772-734.

10 Wohl, K., Kapp, N.M., and Gazley, C., "Flame Stabilization and Quenching", *Proc. Comb. Inst.*, Vol. 3, 1951, pp. 3-21.

11 Nicholson, H., and Field, J., "Some Experimental Techniques for the Investigation of Mechanism of Flame Stabilization in the Wakes of Bluff bodies", *Proc. Comb. Inst.*, Vol. 3, 1951, pp. 44-68.

12 Chen, T. H., Goss, L. P., Talley, D., and Mikolaitis, D., "Stabilization zone structure in jet diffusion flames from liftoff to blowout", paper AIAA-89-0153, *27th AIAA Aerospace Sciences Meeting*, Reno, NV, Jan 9-12, 1989.

13 Gutmark, E., Parr, T. P., Hanson-Parr, D. M., and Schadow, K. C., "Simultaneous OH and Schlieren visualization of premixed flames at the lean blow-out limit", *Experiments in fluids,* Vol 12, 1991, pp 10-16.

14 Kostiuk, L.W., Bray K.N.C., and Cheng, R. K., "Experimental study of premixed turbulent combustion in opposed streams. Part II – Reacting flow field and extinction", *Combustion and Flame*, Vol. 92, 1993, pp. 396-409.

15 Bayliss, A., Leaf, G. K., and Matkowsky, B. J., "Pulsating and chaotic dynamics near the extinction limit", *Comb. Sci. and Technol.*, Vol. 84, 1992, pp. 253-278.

16 Gorman, M., El-Hamdi, M., and Robbins, K. A., "Chaotic dynamics near the extinction limit of a premixed flame on a porous plug burner", *Comb. Sci. and Technol.*, Vol. 98, 1994, pp. 47-56.

17 Kurosoy, E., and Whitelaw, J. H., "Extinction and relight in opposed flames", *Experiments in Fluids*, Vol. 33, 2002, pp. 75-89.

18 Sardi, K., Taylor, A.M.K.P., and Whitelaw, J.H., "Extinction of turbulent counterflow flames under periodic strain", *Combustion and Flame*, Vol. 120, 2000, pp. 265-284.

19 Roquemore, W. M., Reddy, V. K., Hedman, P. O., Post, M. E., Chen, T. H., Goss, L. P. Trump, D., Vilimpoc, V., and Sturgess, G. J., "Experimental and Theoretical studies in a Gas-fueled research combustor", paper AIAA-91-0639, *29th Aerospace Sciences Meeting,* Reno, NV, Jan 7-10, 1991.

20 Chao, Y.C., Chang, Y.L., Wu, C.Y., and Cheng, T.S., "An Experimental Investigation of the Blowout Process of a Jet Flame", *Proc. Comb. Inst.*, Vol. 28, 2000.

21 De Zilwa, S.R.N., Uhm, J.H., and Whitelaw, J.H., "Combustion oscillations close to the lean flammability limit", *Comb. Sci. and Technol.*, Vol. 160, 2000, pp 231-258.

22 Black, D.L., and Smith, C.E., "Transient lean blowout modeling of an aero low emission fuel injector", paper AIAA-2003-4520, 39th AIAA/ASME/SAE/ASEE Joint propulsion conference, Huntsville, AL, Jul 20-23, 2003.

23 Lucenko, M., Vanderleest, R. E., Onge, K. J. St., "Method and apparatus for detecting burner blowout", United States patent number 5581995, Dec 10, 1996.

24 Snyder, T. S., Rosfjord, T. J., "Active gas turbine combustion control to minimize nitric oxide emissions", United States patent number 5706643, Jan 13, 1998.

25 Nair, S., "Acoustic Characterization of flame blowout phenomenon", PhD dissertation, Georgia Institute of Technology, Atlanta GA 30332, May 2006.

26 Strehlow, R. A., and Savage, L. D., "The concept of flame stretch", *Combustion and Flame*, Vol. 31, 1978, pp. 209-211.

27 Law, C. K., "Dynamics of Stretched Laminar Flames", Proc. Comb. Inst., Vol. 22, 1988, pp. 1381-1402.

28 Peters, N., "Turbulent Combustion", Cambridge monographs on mechanics, 1st ed., Cambridge University Press, 2000.

29 Muller, C.M., Breitbach, H., and Peters, N., "Partially premixed turbulent flame propagation in jet flames", *Proc. Comb. Inst.*, vol. 25, 1994, pp. 1099-1106.

30 Schefer, R. W., and Goix, P. J., "Mechanism of flame stabilization in turbulent, lifted-jet flames", *Combustion and Flame*, vol. 112, 1998, pp. 559-574.

31 Durbin, M.D., and Ballal, D.R., 1996, “Studies of Lean Blowout in a Step Swirl Combustor”, *Transactions of the ASME*, Vol. 118, pp 72-77.

32 Longwell, J. P., “Flame Stabilization by Bluff Bodies and Turbulent Flames in Ducts”, *Proc. Comb. Inst.*,Vol. 4, 1953, pp. 90-97.

33 Williams, G., Hottel, H., and Scurlock, A., “Flame Stabilization and Propagation in High Velocity Gas Streams”, *Proc. Comb. Inst.*, Vol. 3, 1951, pp. 21-40.

34 Feikema, D., Chen, R-H., and Driscoll, J., “Enhancement of flame blowout limits by the use of swirl”, *Combustion and Flame*, Vol. 80, 1990, pp. 183-195.

35 Khitrin, L. N. and Goldenberg, S. A., “The Influence of the Initial Temperature of a Combustible Mixture and of the Ambient Pressure on the Stabilization Limits”, *Proc. Comb. Inst.*, Vol. 6, 1955, pp. 448-451, 1955.

36 Cheng, S.I., and Kovitz, A.A., “Theory of Flame stabilization by a Bluff body”, *Proc. Comb. Inst.*, Vol. 7, 1958, pp. 681-691.

37 Hertzberg, J.R., Shepherd, I.G., and Talbot, L., “Vortex Shedding Behind Rod Stabilized Flames”, *Combustion and Flame*, Vol. 86, 1991, pp. 1-11.

38 Ateshkadi, A., McDonnell, V.G., and Samuelson, G. S., “Lean Blowout model for a Spray Fired Swirl Stabilized Combustor”, *Proc. Comb. Inst.*, Vol. 28, 2000, pp. 1281-1288.

39 Lewis, B. and von Elbe, G., “Combustion, flames and explosions of gases”, 2nd ed., Academic Press, 1961.

40 Warris, A. M., and Weinberg, F., “Ignition and flame stabilization by plasma jets in fast gas streams”, *Proc. Comb. Inst.*, Vol. 20, 1984, pp. 1825 – 1831.

41 Weinberg, F.J., “Advanced combustion methods”, Academic press, 1986.

42 Galley, P., Pilla, G., Lacostet, D., Ducruix, S., Lacas, F., Veynante, D., and Laux, C.O., “Plasma enhanced combustion of a lean premixed air propane turbulent flame using a nanosecond repetitively pulsed plasma”, paper AIAA-2005-1193, 43rd AIAA Aerospace Sciences meeting and exhibit, Reno, NV, Jan 10-13, 2005.

43 Switenbank, J., Turan, A., and Felton, P.G., “Three-dimensional two-phase modeling of gas turbine combustors”, Gas Turbine Combustor Design Problems, Lefebvre, A. H., editor, Hemisphere Publishing, NewYork, 1980, pp. 249-314.

44 Lucca-Negro O., and O’Doherty T., “Vortex breakdown: a review”, *Prog. Energy and Comb. Sci.*, Vol. 27, 2001, pp. 431-481.

45 Bradley D., Gaskell P.H., Gu X.J., Lawes M., and Scott M.J., “Premixed turbulent flame instability and NO formation in a lean burn swirl burner”, *Combustion and Flame*, Vol. 115, 1998, pp. 515-538.

46 Umemura and Tomita, “Rapid Flame Propagation in a Vortex Tube in Perspective of Vortex Breakdown Phenomena.” *Combustion and Flame*, Vol. 125, 2001, pp. 820-838.

47 Sarpkaya T., “On stationary and traveling vortex breakdown”, *Jl. Fluid Mech.*, Vol. 45, 1971, pp. 545-559.

48 Faler J.H., and Leibovich S., “Disrupted states of vortex fow and vortex breakdown”, *Phys. Fluids*, Vol. 20, 1977, pp. 1385-1400.

49 Escudier M.P., “Vortex breakdown: observations and explanations”, *Prog. Aerospace Sci.*, Vol.25, 1988, pp. 189-229.

50 Billant P., Chomaz J-M., and Hurre P., “Experimental study of vortex breakdown in swirling jets”, *Jl. Fluid Mech.*, Vol. 376, 1998, pp. 183-219.

51 Ruith M.R., Chen P., Meiburg E., and Maxworthy T., “Three-dimensional vortex breakdown in swirling jets and wakes: direct numerical simulation”, *Jl. Fluid Mech.*, Vol. 486, 2003, pp. 331-378.

52 Sotiropoulos, F., Ventikos, Y., and Lackey, T.C., “Chaotic advection in three-dimentsional stationary vortex-breakdown bubbles: Sil’nikov’s chaos and the devil’s staircase”, *Jl. Fluid Mech.*, Vol. 444, 2001, pp. 257-297.

53 Alekseenko S.V., Kuibin P.A., Okulov V.L., and Shtork S.I., “Helical vortices in swirl flow”, *Jl. Fluid Mech.*, Vol. 382, 1999, pp. 195-243.

54 Marques F., and Lopez J.M., “Precessing vortex breakdown mode in an enclosed cylinder flow”, *Phys. Fluids*, Vol. 13, No. 6, Jun 2001, pp. 1679-1682.

55 Billant P., Chomaz J-M., Delbende I., Huerre P., Loisseleux T., Olendraru C., Rossi M., and Sellier A., “Instabilities and vortex breakdown in swirling jets and wakes”, in Dynamics of slender vortices, Krause E., and Gersten K. (Eds.), IUTAM symposium on dynamics of slender vortices, Kluwer academic publishers, 1998, pp. 267-286.

56 Serre E., and Bontoux P., “Vortex breakdown in a three-dimensional swirling flow”, *Jl. Fluid Mech.*, Vol. 459, 2002, pp. 347-370.

57 Althaus W., and Weimer M., “Review of the Aachen work on vortex breakdown”, in Dynamics of slender vortices, Krause E., and Gersten K. (Eds.), IUTAM symposium on dynamics of slender vortices, Kluwer academic publishers, 1998, pp. 331-344.

58 Saprkaya T., and Novak F., “Turbulent vortex breakdown: Experiments in tubes at high Reynolds numbers”, in *Dynamics of slender vortices*, Krause E., and Gersten K. (Eds.), IUTAM symposium on dynamics of slender vortices, Kluwer academic publishers, 1998, pp. 287-296.

59 Guo. B., Langrish T.A.G., and Fletcher D.L., “Simulation of turbulent swirl flow in an axisymmetric sudden expansion”, *AIAA Jl.*, Vol. 39, No. 1, Jan 2001, pp. 96-102.

60 Spall R.E., “Transition from spiral- to bubble- type vortex breakdown”, Brief communications, *Phys. Fluids*, Vol 8, No. 5, May 1996, pp. 1330-1332.

61 Fick W., Griffiths A.J., and O'Doherty T., "Visualization of the precessing vortex core in an unconfined swirling flow", *Optical diagnostics and Engg.*, Vol. 2, No. 1, 1997, pp. 19-31.

62 Syred N., Gupta A.K., and Beer J.M., "Temperature and density gradient changes arising with the precessing vortex core and vortex breakdown in swirl burners", *Proc. Comb. Inst.*, Vol. 15, 1975, pp. 587-597.

63 Lilley, D.G., "Swirl flows in combustion: a Review", *AIAA Jl.*, Vol. 15, No. 8, 1977, pp1063-1078.

64 Baker, R.J., Hutchinson, P., Khalil, E.E., and Whitelaw, J.H., "Measurements of three velocity components in a model furnace with and without combustion", *Proc. Comb. Inst.*, Vol. 15, 1975, pp553- 559.

65 Chigier, N. A., and Dvorak, K., "Laser anemometer measurements in flames with swirl", *Proc. Comb. Inst.*, Vol 15, 1975, pp. 573-585.

66 Syred, N., Chigier, N.A., and Beer, J.M., "Flame stabilization in recirculation zones of jets with swirl", *Proc. Comb. Inst.*, Vol. 13, 1971, pp 617-624.

67 Wang, S., Hsieh, S-Y., and Yang, V., "Unsteady flow evolution in swirl injector with radial entry. I. Stationary conditions", *Physics of Fluids*, Vol. 17, 2005, pp. 1-13.

68 Rusak, Z., Kapila, A. K., and Choi, J. J., "Effect of combustion on near-critical swirling flow", *Combustion Theory and Modeling*, Vol. 6, 2002, pp. 625-645.

69 Ghoniem, A.F., Soteriou, M.C., Knio O.M., and Cetegen, B., "Effect of steady and periodic strain on unsteady flamelet combustion", *Proc. Comb. Inst.*, Vol. 24, 1992, pp 223-230.

70 Law, C.K., Zhu, D.L., and Yu, G., "Propagation and extinction of stretched premixed flames", *Proc. Comb. Inst.*, Vol. 21, 1986, pp.1419-1426.

71 Im, H.G., Bechtold, J.K., and Law, C.K., "Response of counterflow premixed flames to oscillating strain rates", *Combustion and Flame*, Vol. 105, 1996, pp 358-372.

72 Sardi, K. and Whitelaw, J. H., "Extinction timescales of periodically strained lean counterflow flames", *Experiments in fluids*, Vol. 27, 1999, pp. 199-209.

73 Amantini, G., Frank, J. H., and Gomez, A., "Experiments on standing and traveling edge flames around flame holes", *Proc. Comb. Inst.*, Vol. 30, 2005, pp. 313-321.

74 Hedman, P.O., Fletcher, T.H., Graham, S.G., Timothy, G.W., Flores, D.V., and Haslam, J.K., "Observations of Flame Behavior in a Laboratory-Scale Pre-mixed Natural Gas/Air Gas Turbine Combustor from PLIF measurements of OH", Paper No. GT-2002-30052, Proceedings of ASME TURBO EXPO 2002, Jun 3-6, Amsterdam, Netherlands, 2002.

75 Gupta, A.K., Lilley, D.G., and Syred, N., "Swirl Flows", Abacus Press, Kent, England, 1984.

76 Kahler, C.J., Sammler, B., and Kompenhans, J., "Generation and control of tracer particles for optical flow investigations in air", *Experiments in Fluids*, Vol. 33, 2002, pp. 736-742.

77 Melling, A., "Tracer particles and seeding for particle image velocimetry", *Meas. Sci. Technol.*, Vol. 8, 1997, pp. 1406-1416.

78 Muruganandam, T. M., Kim, B.-H., Morrell, M. R., Nori, V., Patel, M., Romig, B. W., and Seitzman, J. M., "Optical equivalence ratio sensors for gas turbine combustors", *Proc. Comb. Inst.*, Vol. 30, No. 1, 2005, pp. 1601-1609.

79 Hermanson, J. C., Colket, M. B., and Sangiovanni, J. J., "Stability and Emissions of Lean, Turbulent, Premixed Flames with Very Lean Coflow", *AIAA Jl.*, Vol. 35, No. 11, 1997, pp 1705-1711.

80 Hiers R. S., Jr., and Hiers R. S., III, "development of high-temperature image probes for viewing turbine engine augmntors, paper AIAA-2002-2912, 22nd AIAA Aerodynamic measurement technology and ground testing conference, St. Louis, MO, Jun 24-26, 2002.